ABSTRACT

Title of Thesis: ANALYSIS OF NONLINEAR BEHAVIOR IN NOVEL PNEUMATIC ARTIFICIAL MUSCLES

Erica Grace Hocking, Master of Science, 2012

Thesis Directed By: Professor Norman M. Wereley, Department of Aerospace Engineering

Motivated by the excellent actuator characteristics of pneumatic artificial muscles (PAMs), two novel actuators based on this technology were developed for applications where traditional PAMs are not suitable. The first of these actuators is a miniature PAM that possesses the same operating principle as a full-scale contractile PAM, but with a diameter an order of magnitude smaller. The second actuator, a push-PAM, harnesses the operational characteristics of a contractile PAM, but changes the direction of motion and force with a simple conversion package. Testing on these actuators revealed each PAM's evolution of force with displacement for a range of operating pressures. To address the analysis of the nonlinear response of these PAMs, a nonlinear stress vs. strain model, a hysteresis model, and a pressure deadband were introduced into a previously developed force balance analysis. The refined nonlinear model was shown to reconstruct PAM response with higher accuracy than previously possible.

ANALYSIS OF NONLINEAR BEHAVIOR IN NOVEL PNEUMATIC ARTIFICIAL MUSCLES

By

Erica Grace Hocking

Thesis submitted to the Faculty of the Graduate School of the
University of Maryland, College Park, in partial fulfillment
of the requirements for the degree of
Master of Science
2012

Advisory Committee:
Professor Norman M. Wereley, Chair
Professor Inderjit Chopra
Professor Sung Lee

Acknowledgements

I would like to begin by thanking my advisor and thesis committee chair, Dr. Norman Wereley. Without his guidance, support, and direction over the last two years, I would not have been able to accomplish the research presented here. I would also like to thank the other members of my committee, Dr. Inderjit Chopra and Dr. Sung Lee, for their assistance and feedback in preparing my thesis.

For their help with learning the ropes of PAM construction and general machining techniques, I owe a big thank you to Ben Woods and Robbie Vocke. Both were always quick to put aside whatever they were working on and lend me a hand whenever I needed it. Similarly, I would like to thank Ryan Robinson. Ben, Robbie, and Ryan were my predecessors in the PAM community here at the University of Maryland, and their advice on manufacturing, testing, and analysis was invaluable.

I would also like to acknowledge the love and encouragement of my family and friends. My parents, Adair and Mark, have been supportive of me in every aspect of my academic career, and I can't say how much I appreciate all that they have done to help me get to this point. In the face of research success and adversity, my boyfriend, Adam, has been there every step of the way to celebrate or commiserate with me, and his constant encouragement has kept me motivated throughout this process. I also want to thank all of my friends and coworkers who have made grad school way more fun than it should have been: Joe, Jill, Will, Jeremy, Kate, Conor, Elizabeth, Ian, Chris, Doug, Ben, Robbie, Andrew, Shane, Harinder, Ami, Steve, Nick, Ryan, and Xianxu (in no particular order).

Finally, this research was made with Government support under and awarded by the DoD, Air Force Office of Scientific Research, National Defense Science and Engineering Graduate (NDSEG) Fellowship, 32 CFR 168a.

Table of Contents

List of Tables

List of Figures

Nomenclature

A_B	=	cross-sectional of bladder
B	=	length of sleeve fiber
D	=	outer diameter of bladder
E	=	elastic modulus
F	=	force generated by PAM
F_{AVG}	=	pressure-averaged force
F_B	=	pressure-averaged blocked force
F_F	=	friction force
F_G	=	Gaylord force
F_{LFB}	=	linear elastic force balance force correction
F_{NLFB}	=	nonlinear elastic force balance force correction
k_F	=	friction factor
L_0	=	initial (active) length of PAM
L	=	instantaneous length of PAM
L'	=	corrected length of PAM
M	=	summation upper limit
N	=	number of turns of sleeve fiber
P	=	actuation pressure
P'	=	corrected actuation pressure
P_c	=	pressure offset for PAM actuation (threshold pressure)
R_0	=	initial outer radius of bladder
R	=	instantaneous outer radius of bladder

T	=	tension in sleeve fiber
t	=	instantaneous thickness of bladder
V_B	=	volume of bladder
v	=	velocity
α	=	braid angle (radial)
ε	=	strain in bladder
ΔL	=	change in length of PAM
Δl	=	tip shape length correction
ΔR	=	change in radius of bladder
σ	=	stress in bladder

1. Introduction

1.1. Background and Motivation

Fluidic artificial muscles (FAMs) are simple mechanical actuators that consist of an elastomeric bladder within a braided mesh sleeve, with two end fittings that serve to seal the ends of the FAM, provide actuator attachment points, and create a channel for the injection of the working fluid. Upon pressurization of the bladder (by air, water, oil, etc.), the actuator either contracts or extends axially, with the direction of motion dependent on the orientation of the braided sleeve fibers. Because contractile FAMs are able to produce higher forces than extensile FAMs and are less prone to buckling [1-5], contractile FAMs are more commonly utilized and the term FAM typically refers to a contractile actuator.

As Joseph McKibben is usually credited with the development of the first FAM in the 1950s, these devices are often referred to as McKibben Actuators. However, other widely used names for this class of actuators include Pneumatic Artificial Muscle, Braided Artificial Muscle, Fluidic Flexible Matrix Composite, Rubber Muscle Actuator, and Rubbertuator (as trademarked by the Bridgestone Company). As the devices discussed in the ensuing chapters are actuated using pressurized air, Pneumatic Artificial Muscle (PAM) is the preferred nomenclature that will be used throughout this work.

Contractile PAMs offer numerous advantages over more traditional actuation technologies, most notably high forces and displacements despite their relatively small size and weight. Adapted from Ref. [6], Table 1.1 shows the maximum strain (stroke divided by resting length), actuation stress (force divided by cross-sectional area), and specific work (work divided by mass) of several types of actuators, including PAMs

developed by previous University of Maryland (UMD) researchers. From this table, it is clear that PAMs combine large usable strains with large actuation stresses to yield a higher ratio of work to mass (i.e. specific work) than several other actuation technologies such as electromechanical actuators, solenoids, and piezoelectric or magnetostrictive materials. Similarly, other researchers have reported that the ratio of power to weight (i.e. specific power) of PAMs can range from 500 – 2000 W/kg [7], while that of electric motors is only on the order of 100 W/kg [8].

Table 1.1 Comparison of actuator technologies [Modified from Ref. 6]

Actuation Technology	Max Strain	Actuation Stress (MPa)	Specific Work (J/kg)
Hydraulic	1	70	35000
Electromechanical	0.5	1	300
Solenoid	0.4	0.1	5
Piezoelectric	0.002	9	1
Magnetostrictive	0.002	200	20
Shape Memory Alloy (SMA)	0.07	700	4500
Pneumatic Cylinder	1	0.9	1200
UMD PAM	0.4	16	4400

In addition to these performance advantages, PAMs boast a variety of structural advantages as well. Because of their simple design, PAMs can be manufactured relatively easily using low-cost materials. Furthermore, PAMs are very durable and possess a long fatigue life, having demonstrated only small signs of wear and tear after 120 million actuation cycles [5]. These actuators are also compliant, making them safe for human interaction and tolerant of mechanical misalignment and impulsive loading.

As a result of these advantageous properties, PAMs have attracted interest in a wide array of fields. One of the first and most common applications for PAMs is within prosthetics/orthotics. In addition to the original use of the McKibben muscle for assisting polio patients who had experienced paralysis in their hands, researchers have more recently used PAMs to actuate rehabilitation devices [9], an ankle-foot orthosis [10-11], and a knee-ankle-foot orthosis [12]. In the field of robotics, researchers have investigated using PAMs for a robotic manipulator capable of lifting heavy payloads [13], a cricket-inspired walking/jumping micro-robot [14], and a medical robot for keyhole surgery [15]. Additionally, within aerospace engineering, PAMs have received recent attention as actuators for morphing wing concepts [16-17], as well as trailing edge flap systems [5-6,18]. A more comprehensive review of some of the applications of PAMs is undertaken by Zhang and Philen in Ref. [19].

In addition to experimental characterization and application development, several researchers have also investigated the modeling and analysis of these devices so that they may be accurately controlled in any actuation scheme. Mathematical actuator models have been developed to relate force generation, contraction, and actuation pressure within PAMs using both energy balance and force balance methods of derivation [7,15,20-26]. Furthermore, refinements to these models have been suggested to account for factors such as elasticity in the braid and bladder, non-cylindrical tip shapes, and friction between the actuator components [18,21-27]. A full review of the modeling efforts developed to capture the actuation behavior of PAMs is given in Ref. [28]. Despite these efforts, however, these models lack the ability to fully account for the many nonlinearities associated with PAM actuation.

1.2. Objective of Present Research

Given the excellent actuator characteristics of contractile PAMs, the first objective of this research was to develop and characterize two novel actuators based on this technology for use in new applications where traditional PAMs may not be suitable. The first of these actuators is a miniature PAM that possesses the same operating principle as a full-scale contractile PAM, but with a diameter an order of magnitude smaller so that the device may be incorporated in small-scale mechanical systems. The second actuator, known as a push-PAM, harnesses the operational characteristics of a typical contractile PAM, but changes the direction of motion and force with a simple conversion package that demands only a small increase in friction, weight, and cost.

The second objective of this research was to develop a new modeling approach to fully capture the nonlinear actuation behavior of these and all PAMs. Building on the efforts of previous researchers, this new analysis method utilizes additional modeling terms to account for key nonlinear phenomena that were observed in PAM actuation: nonlinear PAM stiffness, hysteresis of the force vs. displacement response for a given pressure, and a pressure deadband.

1.3. Overview of Thesis

This thesis is organized into four chapters to present the different aspects of the research that was undertaken to complete the goals described above.

Chapter 1: Introduction – This chapter presents background information on traditional contractile PAMs and discusses their numerous advantages over other actuation

technologies. Furthermore, current applications of PAM actuators are briefly considered, along with the modeling efforts that have been used thus far to predict the behavior of these devices. Given the current state of PAM technology and analysis, a motivation is established to develop novel PAM actuators for new applications, as well as further refine the modeling methodologies used to characterize PAM behavior.

Chapter 2: Miniature PAM Development and Analysis – The manufacturing process, experimental characterization, and analytical modeling of PAMs with millimeter-scale diameters are presented in this chapter. A fabrication method is developed to consistently deliver low-cost, high-performance, miniature PAMs using commercially available materials. A PAM's full evolution of force with displacement is measured for operating pressures ranging from 207 – 552 kPa (30 – 80 psi in 10 psi increments), as well as the blocked force and free contraction capabilities at each pressure. To address the analysis of the nonlinear response of this miniature PAM, a nonlinear stress vs. strain model, a hysteresis model, and a pressure bias are introduced into a previously developed force balance analysis. Parameters of these nonlinear model refinements are identified from the measured force vs. displacement data. This improved nonlinear force balance model is shown to capture the full actuation behavior of the miniature PAM at each operating pressure and reconstruct the response of the small-scale actuator with much more accuracy than previously possible. Chapter 2 is a manuscript that is being submitted to a special issue of *Smart Materials and Structures* that will focus on bio-inspired smart materials and systems.

Chapter 3: Push-PAM Development and Analysis – This chapter presents the design and characterization of a push-PAM actuator and compares its performance to a traditional contractile PAM. Quasi-static testing on this new actuator reveals the push-PAM's full evolution of force with displacement for operating pressures ranging from 138 – 621 kPa (20 – 90 psi in 10 psi increments), in addition to the blocked force and free contraction capabilities at each pressure, confirming that the push-PAM is able to achieve forces and strokes comparable to a contractile PAM tested under the same conditions. Furthermore, it is shown that the performance of both types of actuators can be captured with the same modeling efforts. The refined force balance analysis from Chapter 2 is applied to these actuators and is shown to reconstruct the actuator response with minimal error for both the contractile PAM and the push-PAM. Chapter 3 is a manuscript that is being submitted to the *ASME Journal of Mechanical Design*. As the push-PAM is the subject of a patent [29], this work was done in collaboration with, and co-authored by, the authors of that patent.

Chapter 4: Conclusions – The key conclusions from the research are summarized in this chapter. Furthermore, this chapter highlights the significant contributions to PAM technology that are made within this body of work and discusses possible future work related to the PAMs developed herein.

1.4. References

[1] Trivedi, D., and Rahn, C. D., 2012, "Soft Robotic Manipulators: Design, Analysis, and Control," *Plants and Mechanical Motion: A Synthetic Approach to Nastic Materials and Structures*, Wereley, N. M., and Sater, J. M., eds., DEStech Publications, Inc., Lancaster, PA, Chap. 7, pp. 141–165.

[2] Pritts, M. B., and Rahn, C. D., 2004, "Design of an Artificial Muscle Continuum Robot," *Proc. IEEE Int. Conf. on Robotics and Automation*, **5**, pp. 4742–4746.

[3] Zhu, B., Rahn, C. D., and Bakis, C. E., 2011, "Actuation of Fluidic Flexible Matrix Composites in Structural Media," J. Intell. Mater. Syst. Struct., **23**(3), pp. 269–278. DOI: 10.1177/1045389X11428676

[4] Philen, M. K., Shan, Y., Prakash, P., Wang, K. W., Rahn, C. D., Zydney, A. L., and Bakis, C. E., 2007, "Fibrillar Network Adaptive Structure with Ion-transport Actuation," J. Intell. Mater. Syst. Struct., **18**(4), pp. 323–334. DOI: 10.1177/1045389X06066097

[5] Woods, B. K. S., Gentry, M. F., Kothera, C. S., and Wereley, N. M., 2011, "Fatigue Life Testing of Swaged Pneumatic Artificial Muscles as Actuators for Aerospace Applications," J. Intell. Mater. Syst. Struct., **23**(3), pp. 327–343. DOI: 10.1177/1045389X11433495

[6] Woods, B. K. S., 2012, "Pneumatic Artificial Muscle Driven Trailing Edge Flaps for Active Rotors," Ph.D. Thesis, University of Maryland, College Park.

[7] Caldwell, D., Tsagarakis, N., and Medrano-Cerda, G. A., 2000, "Bio-mimetic Actuators: Polymeric Pseudo Muscular Actuators and Pneumatic Muscle

Actuators for Biological Emulation," Mechatronics, **10**(4–5), pp. 499–530. DOI: 10.1016/S0957-4158(99)00071-9

[8] Daerden, F., 1999, "Conception and Realization of Pleated Pneumatic Artificial Muscles and their Use as Compliant Actuation Elements," Ph.D. Thesis, Vrije University Brussel, Brussels.

[9] Bharadwaj, K., Hollander, K. W., Mathis, C. A., and Sugar, T. G., 2004, "Spring Over Muscle (SOM) Actuator for Rehabilitation Devices," *Proc. Of the 26th Annual Int. Conf. of the IEEE EMBS*, **1**, pp. 2726–2729.

[10] Philen, M. K., 2009, "On the Applicability of Fluidic Flexible Matrix Composite Variable Impedance Materials for Prosthetic and Orthotic Devices," Smart Mater. Struct., **18,** 104023 (10pp). DOI: 10.1088/0964-1726/18/10/104023

[11] Ferris, D. P., Czerniecki, J. M., and Hannaford, B., 2005, "An Ankle-Foot Orthosis Powered by Artificial Pneumatic Muscles," J. Appl. Biomech., **21**(2), pp. 189–197.

[12] Sawicki, G. S., and Ferris, D. P., 2009, "A Pneumatically Powered Knee-Ankle-Foot Orthosis (KAFO) with Myoelectric Activation and Inhibition," J. Neuroeng. Rehabil., **6**(23), pp. 1–16.

[13] Robinson, R. M., Kothera, C. S., Woods, B. K. S., Vocke III, R. D., and Wereley, N. M., 2011, "High Specific Power Actuators for Robotic Manipulators," J. Intell. Mater. Syst. Struct., **22**(13), pp. 1501–1511. DOI: 10.1177/1045389X11417653

[14] Birch, M. C., *et al.*, 2001, "A Miniature Hybrid Robot Propelled by Legs," *Proc. of the 2001 IELE/RSJ Int. Conf. on Intelligent Robots and Systems,* **2**, pp. 845–851.

[15] De Volder, M., Moers, A. J. M., and Reynaerts, D., 2011, "Fabrication and Control of Miniature McKibben Actuators," Sensors Actuat. A, **166**(1), pp. 111–116. DOI: 10.1016/j.sna.2011.01.002

[16] Bubert, E. A., 2009, "Highly Extensible Skin for a Variable Wing-Span Morphing Aircraft Utilizing Pneumatic Artificial Muscle Actuation," M.S. Thesis, University of Maryland, College Park.

[17] Chen, Y., Yin, W., Liu, Y., and Leng, J., 2011, "Structural Design and Analysis of Morphing Skin Embedded with Pneumatic Muscle Fibers," Smart Mater. Struct., **20,** 085033 (8pp). DOI: 10.1088/0964-1726/20/8/085033

[18] Woods, B. K. S., Kothera, C. S., and Wereley, N. M., 2011, "Wind Tunnel Testing of a Helicopter Rotor Trailing Edge Flap Actuated via Pneumatic Artificial Muscles," J. Intell. Mater. Syst. Struct., **22**(13), pp. 1513–1528. DOI: 10.1177/1045389X11424216

[19] Zhang, Z., and Philen, M. K., 2011, "Review: Pressurized Artificial Muscles," J. Intell. Mater. Syst. Struct., **23**(3), pp. 255–268. DOI: 10.1177/1045389X11420592

[20] Gaylord, R., 1958, "Fluid Actuated Motor System and Stroking Device," U.S. Patent No. 2,844,126.

[21] Schulte, H. F., Adamski, D. F., and Pearson, J. R., 1961, "Characteristics of the Braided Fluid Actuator," Report at Department of Physical Medicine and Rehabilitation, the University of Michigan, Ann Arbor, MI, pp. 105–120.

[22] Chou, C., and Hannaford, B., 1994, "Static and Dynamic Characteristics of McKibben Pneumatic Artificial Muscles," *Proc. of ICRA*, **1**, pp. 281–286.

[23] Tondu, B., and Lopez, P., 2000, "Modeling and Control of McKibben Artificial Muscle Robot Actuators," IEEE Control Systems Magazine, **20**(2), pp. 15–38.

[24] Tsagarakis, N., and Caldwell, D., 2000, "Improved Modeling and Assessment of Pneumatic Muscle Actuators," *Proc. of ICRA*, **4**, pp. 3641–3646.

[25] Ferraresi, C., Franco, W., and Bertetto, A. M., 2001, "Flexible Pneumatic Actuators: A Comparison Between the McKibben and the Straight Fibres Muscles," J. Robot. Mechatron., **13**(1), pp. 56–63.

[26] Kothera, C. S., Jangid, M., Sirohi, J., and Wereley, N. M., 2009, "Experimental Characterization and Static Modeling of McKibben Actuators," ASME J. Mech. Des., **131**, 091010 (10pp). DOI: 10.1115/1.3158982

[27] Davis, S., and Caldwell, D., 2006, "Braid Effects on Contractile Range and Friction Modeling in Pneumatic Muscle Actuators," Int. J. Robot. Res., **25**(4), pp. 359–369.

[28] Tondu, B., 2012, "Modelling of the McKibben Artificial Muscle: A Review," J. Intell. Mater. Syst. Struct., **23**(3), pp. 225–253. DOI: 10.1177/1045389X11435435

[29] Woods, B. K. S., Wereley, N. M., Kothera, K. S., Boyer, S. M., "Extensile Fluidic Muscle Actuator," U.S Patent Appl. No. 12/955,242.

2. Miniature PAM Development and Analysis

2.1. Introduction

Small-scale mechanical systems are becoming ever more ubiquitous in current technological developments and applications, introducing a need for compact and lightweight actuation systems that are capable of effecting large forces and strains, but sufficiently small to be contained within these miniature systems. Previous work has established fluidic artificial muscles (FAMs) as an ideal actuation technology when a high premium is placed on maximizing the specific work (ratio of work to mass), specific power (ratio of power to mass), and power density (ratio of power to volume) of the actuator selection [1-5]. Furthermore, FAMs boast a very simple structure, high durability and fatigue life, and are compliant [6]. With these full-scale FAMs (i.e. FAMs with diameters on the order of tens of millimeters) possessing more advantageous characteristics than actuation technologies such as electromechanical actuators, solenoids, and piezoelectric or magnetostrictive materials, the motivation is clear to pursue the miniaturization of FAMs such that they have diameters on the order of millimeters and may be utilized to fill the niche for small-scale actuators in the burgeoning arena of micro-technology.

Miniature FAMs have already been considered by other researchers for several areas of small-scale robotics and other mechanical systems. The vast majority of miniature FAM development and characterization has focused on using air as the working fluid, with the resulting actuator referred to as a pneumatic artificial muscle (PAM), as is the case in this study. In the field of aerospace engineering, for example,

small-scale PAMs have been incorporated into morphing wing concepts and unmanned micro-air vehicle designs [1,7]. Researchers have also applied this technology to medical robots, using miniature PAMs to manipulate a device for keyhole surgery [8]. Furthermore, small-scale PAMs have been considered for actuating the legs on an autonomous micro-robot [9]. In addition to small-scale PAM research, recent studies using miniature hydraulic artificial muscles (HAMs) have employed a liquid, such as water, as the working fluid to increase actuator stiffness (or reduce actuator compliance) and eliminate the need for a large external air compressor, at the cost of reducing bandwidth [10-11].

In addition to experimental characterization and application development, several researchers have also investigated the modeling and analysis of these devices. Mathematical actuator models have been developed to relate force generation, contraction, and actuation pressure within FAMs using both energy balance and force balance methods of derivation [4-5,8,12-17]. Furthermore, refinements to these models have been suggested to account for factors such as elasticity in the braid and bladder, non-cylindrical tip shapes, and friction between the actuator components [2,5,13-18]. A full review of the modeling efforts developed to capture the actuation behavior of FAMs is given in Ref. [19]. Despite these efforts, however, these models lack the ability to fully account for the many nonlinearities associated with FAM actuation.

With the potential for the application of miniature FAMs so far-reaching, the first goal of this study was to develop a highly repeatable manufacturing process for fabricating miniature PAMs having diameters ranging from 3 – 4.25 mm (0.118 – 0.167 in) using low-cost commercially available materials in a manner that yields consistent

performance from one PAM to the next. Utilizing a PAM produced through this methodology, the second objective of this research was to experimentally develop the corresponding actuator load lines, as well as associated blocked force and free contraction capabilities, that describe the performance of the device. Lastly, the development of an analytical model was undertaken, so that these miniature PAMs may be better utilized and controlled in any actuation scheme.

To these ends, the remainder of this chapter is organized into four sections. First, the manufacturing process developed for fabricating PAMs at this small scale will be presented. The PAMs will then be characterized through quasi-static testing on a single actuator to describe the evolution of force with contraction at discrete internal pressures. Next, a nonlinear analysis of these miniature PAMs will be developed, based on a quasi-static linear elastic analysis of full-scale PAMs [16-17], that refines the linear elastic model so that it accurately accounts for the experimentally observed nonlinear effects of nonlinear stiffness, hysteresis, and pressure deadband. Essentially, the analysis is refined by replacing a linear elastic constitutive relationship with a nonlinear one, where the parameters of the nonlinear stress-strain relationship, which are assumed to be functions of pressure, are identified from experimental data. The chapter will conclude with a summary of the findings of this study and a brief discussion of future research.

2.2. Fabrication

Regardless of actuator size and working fluid, FAMs are comprised of the same basic components: a flexible elastomeric bladder surrounded by a braided sleeve, with two end fittings that serve to seal the ends of the FAM, provide actuator attachment points, and create a channel for the injection of the working fluid. In this study, air will be

used as the working fluid, so the discussion will be restricted to PAMs. Figure 2.1 shows a PAM used in this study in both its resting and actuated state. (Note that the bladder is hidden within the braided sleeve.) Upon pressurizing the elastomeric bladder, the radial expansion of the bladder causes a subsequent radial expansion in the surrounding braided sleeve. Because the braided sleeve fibers are much stiffer than the bladder material, the braided sleeve is unable to stretch as the bladder does and instead contracts axially by an amount ΔL to allow for the increase in diameter. This axial contraction of the braided sleeve ultimately generates a pulling force that decreases as ΔL increases until the maximum contraction is reached and the PAM no longer exerts a contractile force.

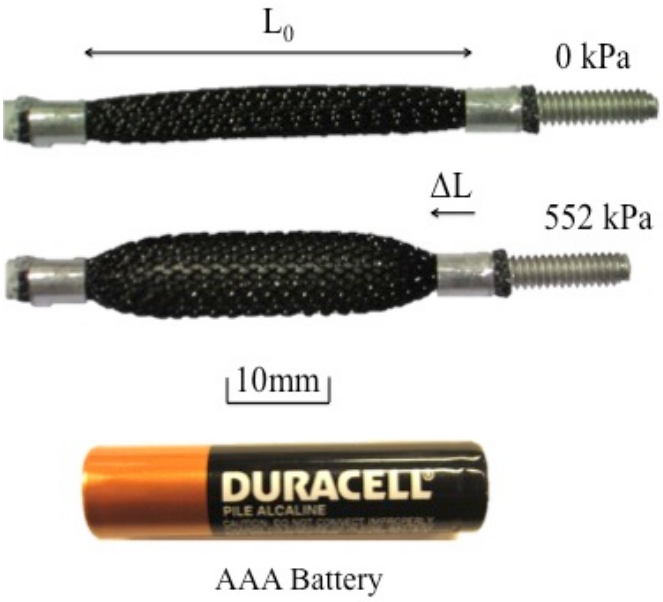

Figure 2.1 Depiction of a PAM at resting length (0 kPa) and in an actuated state (552 kPa) with a AAA battery for a sense of scale.

When developing the fabrication process for the miniaturized PAMs used in this study, it was required that the actuators could be assembled using low-cost materials and that the final product could interface easily with the experimental setup. Furthermore, consistency in the performance of the PAMs and tight seals at the end fittings (to minimize leakage of the working fluid) were outcomes of the utmost importance to the manufacturing process. After trying several different materials and procedures, the methodology that follows proved to best meet these requirements, and to reliably yield high performance actuators.

The PAMs used in this study were fabricated using commercially available aluminum threaded rods, silicone tubing, polyethylene terephthalate (PET) braided sleeve, aluminum tubing, and epoxy. Before the actuator was assembled, two end fittings were machined from the aluminum threaded rods. While one end of the rods remained unaltered in order to allow for the PAMs to screw in to the test bench for easy attachment, the other end was turned down using a lathe to ensure a snug fit with the silicone tubing, braided sleeve, and aluminum tubing. To that end, each rod was machined in a step-down fashion such that diameter of the first 2.54 mm (0.1 in) was 25% larger than the inner diameter of the silicone tubing and the second 2.54 mm (0.1 in) matched the inner diameter of the aluminum tube minus twice the sleeve thickness (see Figure 2.2(a)). Next, a hole was drilled through one of the threaded rods to create a conduit for the working fluid during pressurization. After the end fittings were machined, the rest of the components were cut to the proper lengths for the given PAM. The silicone tubing was cut to the desired active length of the PAM, plus an additional 5.08 mm (0.2 in) to account for the amount of bladder material that would overlap the end fittings.

Similarly, the aluminum tubing was cut into two 5.08 mm (0.2 in) sections to surround the bladder and braid on the turned-down portions of the end fittings. Lastly, the PET braided sleeve was cut to match the active length of the PAM plus the length of the end fittings, then the ends of the braided sleeve were cauterized to prevent fraying during manufacturing. These materials are shown prior to assembly in Figure 2.2(b).

The first step in assembling the PAMs was to apply a thin layer of quick-setting epoxy to the first 2.54 mm (0.1 in) of the end fitting with the thru hole, then slide the silicone tubing onto this portion of the end fitting as shown in Figure 2.2(c). Before allowing the epoxy to cure for half an hour, any excess epoxy that pooled at the edge of the bladder was removed using acetone and a clean cloth. Once the epoxy had fully cured, the next step was to slide the PET braided sleeve around the silicone tubing (from the side of the PAM that was not already attached to an end fitting) until the braided sleeve reached the far edge of the end fitting. In a similar fashion, the two aluminum tubes were then slid over the braided sleeve, just until they were centered over the silicone tubing (Figure 2.2(d)). Next, another thin layer of quick-setting epoxy was applied to the first 2.54 mm (0.1 in) of the remaining end fitting and this component was inserted into the open end of the silicone tubing. In order to prevent epoxy getting on the braid during this step, it was important to push the braided sleeve back, exposing only the silicone tubing and allowing for easy removal of excess epoxy prior to curing (Figure 2.2(e)). After the quick-setting epoxy on the second end fitting had cured for half an hour, a 24-hour epoxy was applied to the exterior of the braided sleeve over the turned-down 5.08 mm (0.2 in) portion of the end fittings (i.e. over the last 2.54 mm (0.1 in) at the extremities of the silicone bladder and the adjacent 2.54 mm (0.1 in) of reduced diameter

threaded rod). With the epoxy on the braided sleeve, the aluminum tubes were finally slid over the epoxy and any excess epoxy on the braids was removed with acetone before allowing the epoxy to cure, as shown in Figure 2.2(f). Lastly, after the epoxy cured for a full 24 hours, the excess braid material beyond the aluminum tubes was cut away from the PAM to fully expose the threaded portion of the end fittings.

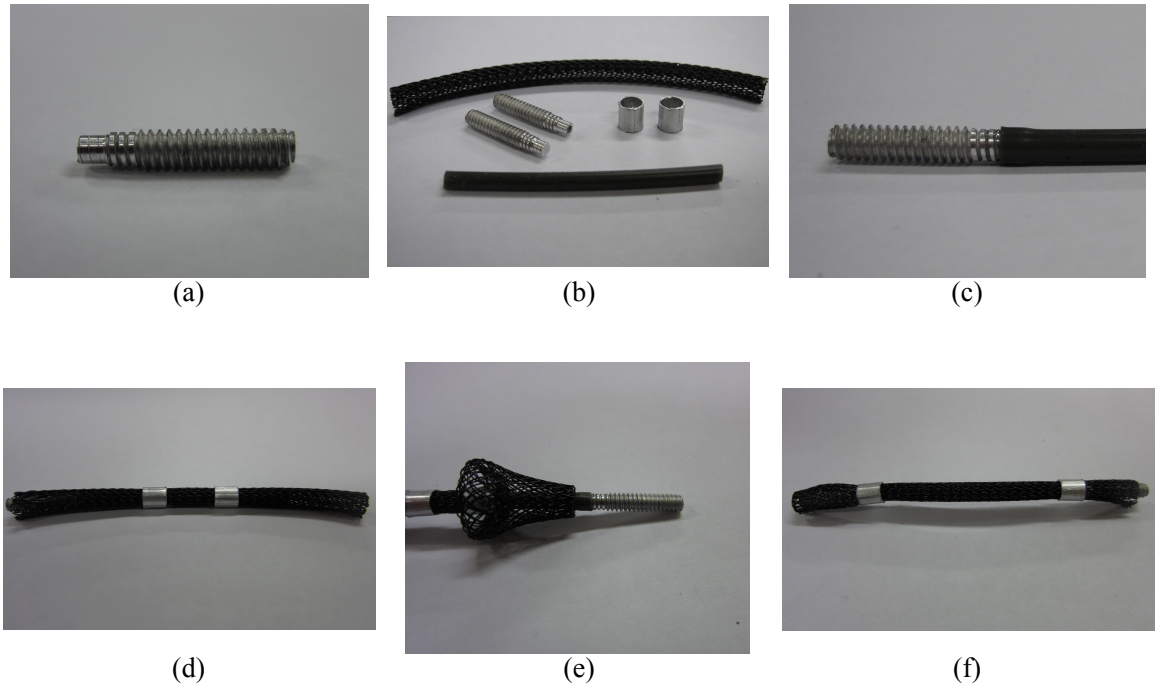

Figure 2.2 Steps in the fabrication process for small-scale PAMs. (a) Machine the end fittings with a step-down diameter scheme. (b) Prior to assembly, gather all materials and cut them to the appropriate size. (c) Attach the silicone tube to the smallest diameter portion of the end fitting. (d) Slide the braided sleeve and aluminum tubes over the silicone tubing before attaching the second end fitting. (e) Push the braided sleeve back when attaching the second end fitting to ensure epoxy does not get on the braid. (f) Slide the aluminum tubes over the end fitting/bladder/epoxy interface.

Although simply assembling the PAM with epoxy at the end fittings did produce a useable actuator, a swaging process was added to the end of the fabrication procedure to provide a reinforced connection at the end fittings and superior PAM performance, as was done by Vocke *et al.* [1]. In this process, the aluminum tube was inserted into a collet that was then tightened in a collet holder, circumferentially crushing the aluminum tube onto the braided sleeve, silicone tubing, and aluminum threaded rod. This uniform application of pressure created additional mechanical interlocking between the PAM components, greatly increasing the strength of the PAM.

While this full manufacturing process was successfully applied to PAMs having active lengths ranging from 20 mm (0.787 in) to 60 mm (2.36 in), and having outer diameters ranging from 3.02 mm (0.119 in) to 4.19 mm (0.165 in), only a single size actuator was used in this study. The actuator presented here had an active length of 39.16 mm (1.54 in) and a diameter of 4.13 mm (0.1625 in). The silicone tubing used for the bladder had an inner diameter of 2 mm (0.0787 in) with a wall thickness of 0.5 mm (0.0394 in). In particular, 6-32 threaded rod was chosen for the end fittings because this size still possessed a threaded surface over the turned-down portion of the rods (see Figure 2.2(a)), which provided increased surface area for strong mechanical and chemical interlocking between the end fitting, silicone bladder, epoxy, and outer aluminum tube. The PET braided sleeve had a nominal diameter of 13.46 mm (0.53 in) at ±45° braid angle. The aluminum tubing had an outer diameter and wall thickness of 4.76 mm (0.198 in) and 0.356 mm (0.014 in), respectively.

2.3. Experimental Characterization

2.3.1. Experimental Procedure

In order to characterize the PAM performance, the actuator underwent quasi-static testing using a 97.9 kN (22 kip) MTS servo-hydraulic test machine. This machine also provided displacement measurements during testing, while a Honeywell load cell rated for 445 N (100 lb) was used to read force measurements because it allowed for higher resolution force data than the MTS was capable of measuring. The PAM was pressurized with a Husky Pro 227 L (60 gal) air compressor. Meanwhile, a Wilkerson Dial-Air pressure regulator with an SSI Technologies, Inc. digital pressure gauge was used to precisely monitor the pressure supplied to the PAM.

The overall goal of the experimental characterization was to determine the evolution of force with displacement for a range of internal pressures. This was achieved by first inflating the PAM to a specific pressure, ranging from 207 – 552 kPa (30 – 80 psi) in 69 kPa (10 psi) increments, with both ends fixed by the MTS grips. After holding momentarily at this condition, one of the MTS heads was unlocked, allowing the PAM to fully contract to the point where it ceased to exert a force. Finally, following another momentary hold, the PAM was then stretched back to its nominal resting length. A given test of the actuator consisted of three of these cycles.

While this test procedure provided data to characterize the entire actuator load line, two main points of interest that were also gleaned from this test were the blocked force and free contraction of the PAM. The blocked force corresponds to the maximum amount of force that the PAM is able to exert at a given internal pressure, which occurs when the actuator is pressurized with both ends of the PAM held fixed at its resting

length. Conversely, free contraction denotes the maximum stroke of the PAM for a given pressure, measured as the contraction at which the PAM no longer produces any force. Figure 2.3 shows the test specimen in each condition at 552 kPa (80 psi). In Figure 2.3(a), the length of the PAM was held constant at its nominal resting length by the MTS grips, while the grips were unlocked in Figure 2.3(b), allowing the PAM to inflate and contract to its maximally contracted state.

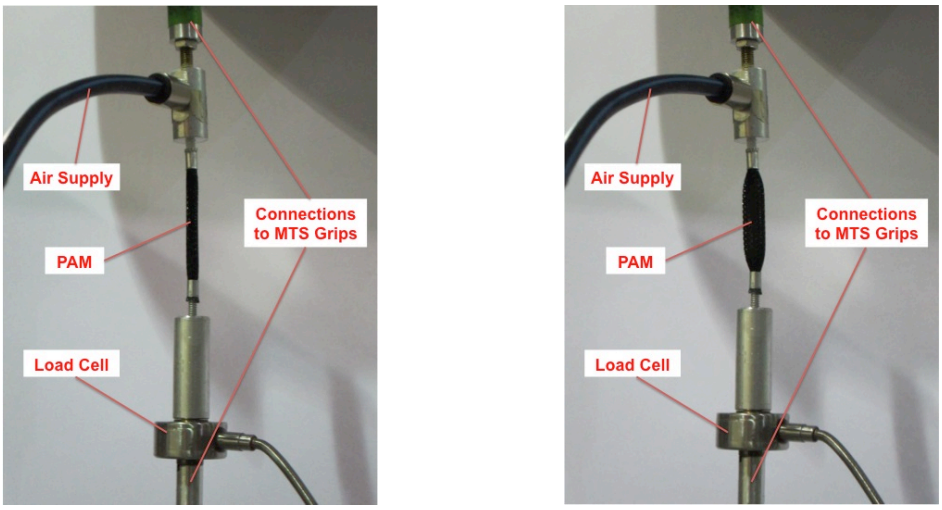

(a) (b)

Figure 2.3 PAM shown in the experimental set up in (a) the blocked force condition and (b) the free contraction condition.

An important effect that was noted in earlier tests of these PAMs was stress-softening of the silicone bladder. This softening (known as the Mullins effect) caused the blocked force and free contraction to increase substantially each time the specimen was tested at a given actuation pressure. Although the physical source of this effect is yet unclear, literature reports that the softening only increases when the rubber is stretched to a new extreme and that the Mullins effect softening stabilizes after a few cycles [20]. Therefore, in order to combat PAM performance creep due to this effect, the actuator was

cycled between 0 and 621 kPa (0 and 90 psi) 25 times with the end free to contract and the bladder free to inflate to its maximum amount. This cycling was carried out before the actuator was tested for the first time in order to stretch the PAM bladder beyond the amount to which it was expected to extend during testing, given that the maximum internal pressure for testing was 552 kPa (80 psi).

2.3.2. Discussion of Experimental Results

The results of a single characterization test are shown in Figure 2.4 for the PAM described above, demonstrating the evolution of force with displacement at a series of discrete internal pressures. The horizontal axis is a non-dimensional measure of contraction given by

$$Contraction = \Delta L / L_0 \,. \tag{1}$$

In this equation, L_0 is the resting length of the PAM (otherwise known as the active length), and ΔL is the amount by which the PAM has contracted (as described above). Because ΔL is taken to be positive when the PAM is contracting, the contraction value calculated using Equation (1) can be considered negative strain in the traditional positive extension strain notation. Also included in Figure 2.4 are dashed lines indicating the average PAM force (F_{AVG}) as a function of contraction for each operating pressure, which will be important for the modeling work discussed in later sections of this chapter.

The actuator load lines in Figure 2.4 clearly show that the force in the PAM decreases with increasing contraction at a given pressure. It is interesting to note, however, that the behavior of the curve changes depending on the amount of contraction the PAM is undergoing. Below about $\Delta L/L_0 = 0.005$, the force drops relatively quickly

with increasing contraction. For contractions in the range $0.005 < \Delta L/L_0 < 0.04$, however, the force decreases at a slower rate along a nearly linear path. Finally, when the PAM contracts above $\Delta L/L_0 = 0.04$, the rate at which the PAM loses its contractile force again increases. This increase in the negative slope of the force vs. displacement curve, or stiffening effect, has not been reported in other PAM research and is most likely attributable to the nature of the small-scale silicone bladder. At higher contractions, it is possible that the silicone rubber is being strained beyond its linear stress-strain relationship and has entered a stiffening region in which stress increases dramatically with strain. Further tests on the silicone bladder alone would need to be conducted in order to verify this phenomenon. Additionally, this effect may simply be more prominent in the characterization of miniaturized PAMs because the bladder volume (V_B) is relatively large compared to the internal volume (V_0) of the actuator. The PAMs used in this study have a volume ratio of $V_B/V_0 = 1.25$, whereas full-scale PAMs like those developed by Kothera *et al.* [17] had a volume ratio of $V_B/V_0 = 0.778$. With the bladder constituting a much larger portion of the PAM cross-sectional area, the elasticity of the bladder has a more dramatic impact on the overall performance of the PAM. As such, stiffening in the silicone could play a key role in creating actuator load lines for these millimeter-scale diameter PAMs that differ greatly from their full-scale counterparts.

It is also important to note the hysteresis in the actuator load lines, with the lower line corresponding to the path from blocked force to free contraction and the upper line corresponding to the return path. This results from friction between the braid and the bladder during inflation and deflation, as well as friction between the individual fibers of the braid as the braid angle changes. As mentioned in the experimental setup, however,

each test is actually comprised of three cycles between blocked force and free contraction (all of which are plotted in Figure 2.4), so there is excellent repeatability in the characteristics of the PAM actuation.

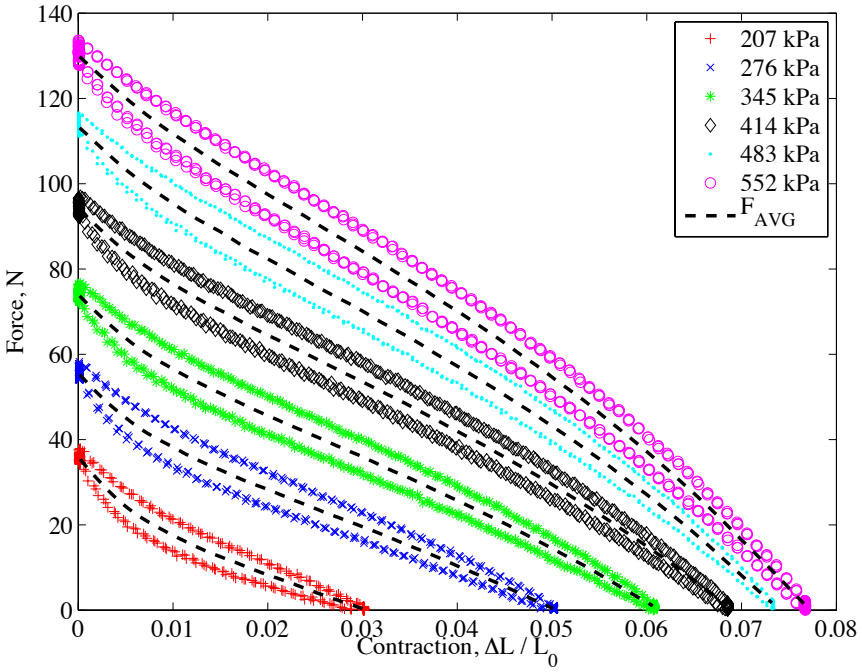

Figure 2.4 Experimentally characterized actuator load lines at a series of discrete internal pressures.

As previously mentioned, two main parameters of interest are the blocked force and free contraction of the PAM at each internal pressure. These values are represented in Figure 2.5 as the points at which the actuator load lines reach each axis (blocked force on the vertical axis and free contraction on the horizontal axis). It is evident in this figure that both blocked force and free contraction increase with pressure. For clarity, however, the strict evolution of each parameter with internal pressure is shown separately in Figure 2.5. The results of seven separate tests on the same PAM specimen are shown in these graphs.

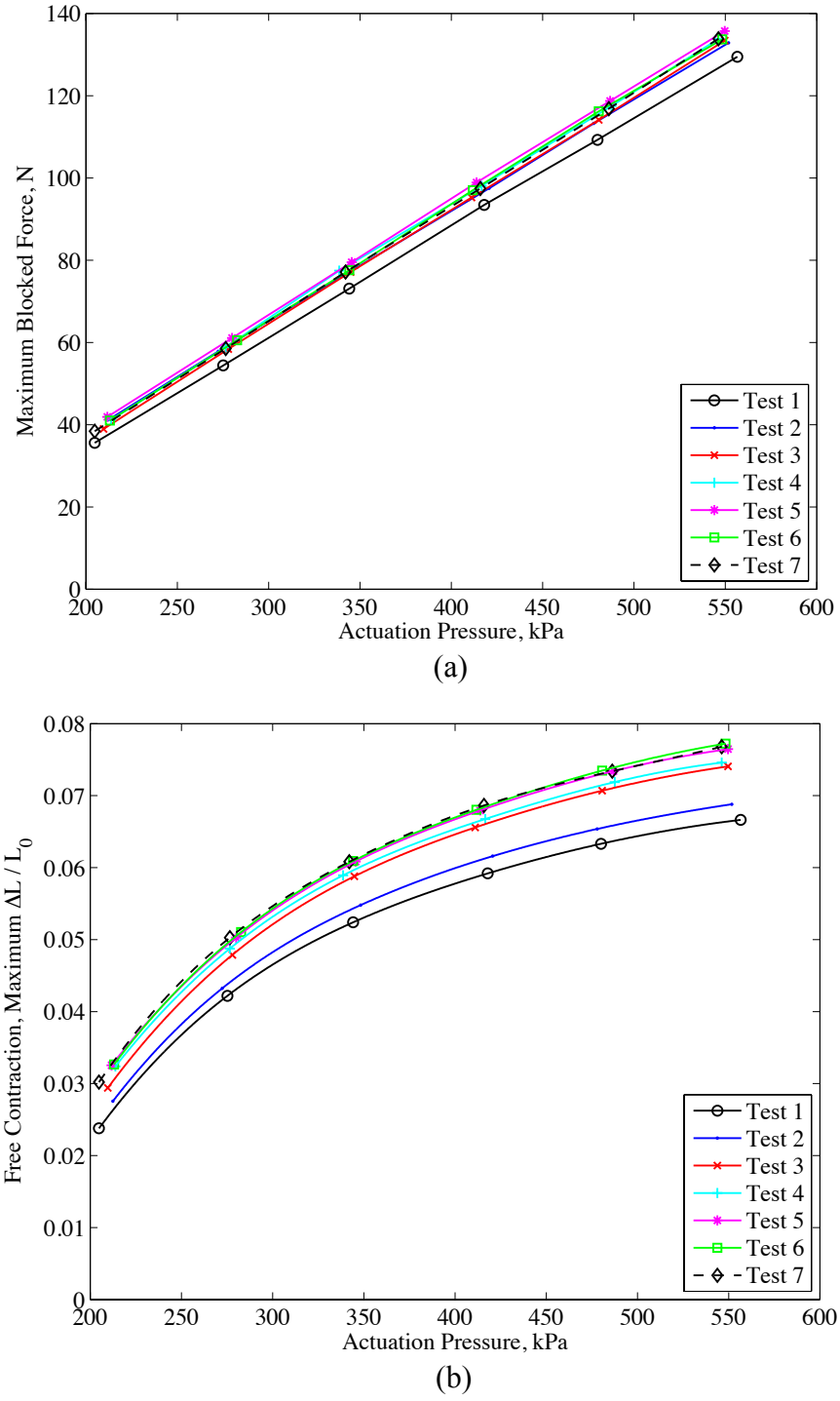

Figure 2.5 Seven sets of experimental data from the same PAM specimen for (a) blocked force and (b) free contraction as a function of pressure.

The data shown in Figure 2.5 reveal several significant qualities of the PAM actuator. First, in the blocked force diagram (Figure 2.5(a)), the maximum force exerted by the PAM increases linearly with increased actuation pressure across the full range of tested pressures, which is consistent with trends reported in literature for both full-scale and miniature PAMs [7-8,17]. On the other hand, free contraction (in Figure 2.5(b)) increases non-linearly with pressure and the maximum contraction begins to level off above about 345 kPa (50 psi) as the effect of increasing pressure diminishes. Because the physical constraints of the braided sleeve were not yet met at the radial dimensions exhibited during testing, this plateau in free contraction is most likely due to the silicone bladder nearing is largest allowable diameter. The maximum blocked force achieved during testing was 135.7 N (30.51 lb) and the maximum achieved free contraction was $\Delta L/L_0 = 0.0772$ (i.e. 7.72%), both of which occurred at an actuation pressure of 552 kPa (80 psi).

The results shown in Figure 2.5 also demonstrate the impact of the aforementioned stress-softening in the bladder. Although each set of test data follows the same trends, it is clear that the blocked force and free contraction of the PAM were initially increasing from one test to the next. While the blocked force saturated after a couple tests, larger increases in free contraction are evident because free contraction is more dependent than blocked force on bladder elasticity. Although the pre-cycling of the PAMs at 621 kPa (90 psi) greatly improved the consistency of the PAM performance with respect to previous PAM specimens that had been tested, the impact of the Mullins effect was still evident. In order to fully characterize the increase in PAM performance, and determine if this performance ever reached a plateau, the same PAM was tested

repeatedly over the course of several days. As shown in Figure 2.5, the PAM performance did indeed stabilize, with the PAM producing consistent results after Test 4. (Note: A large in increase in free contraction from Test 2 to Test 3 was observed because the PAM was cycled further between these two tests without data being recorded.)

2.4. Model Development and Validation

With the feasibility of a creating a high-performance PAM with a millimeter-scale diameter having been proven through experimental characterization, the next step in this study was to develop a model capable of accurately predicting the output of the actuator. As with all PAMs, the geometry of the braided sleeve plays a major role in determining the response of the actuator. From the braid angle α (taken from the radial plane of the actuator to the braid fibers), the current actuator length L (given by L_0 - ΔL), and the bladder outer diameter D, the following braid parameters can be calculated through geometric constraints:

$$B = \frac{L}{\sin\alpha} \tag{2}$$

and

$$N = \frac{B\cos\alpha}{\pi D} \tag{3}$$

where B is the length of one fiber and N is the number of turns the fiber makes around the bladder. For ease of measurement, the braid angle, length, and bladder outer diameter used to calculate B and N were measured while the PAM was in its resting state. For the particular PAM used in this study, the initial braid angle was 77°, the resting length was 39.16 mm (1.54 in), and the initial bladder outer diameter was 3 mm (0.1181 in).

2.4.1. Gaylord Force Model

Using these basic geometric constraints, a number of models have been developed to predict PAM actuation behavior, with most models focusing on either energy balance or force balance methods of derivation [4-5,8,12-17]. These methods all agree upon the same initial forcing term, known as the Gaylord force,

$$F_G = \frac{P}{4N^2\pi}\left(3L^2 - B^2\right) \tag{4}$$

where F_G is the force generated by the PAM upon pressurization and P is the actuation pressure. While this model provides a reasonable estimate for blocked force, it fails to capture the nonlinearity of the actuation diagram and over-predicts PAM contraction. In order to better represent actuator behavior, several correction terms have been added to the Gaylord force to account for factors such as elasticity in the braid and bladder, non-cylindrical tip shapes, and friction between the actuator components [2,5,13-18].

2.4.2. Force Balance Model

Of these various models, the force balance model first proposed by Ferraresi *et al.* [16] and later refined by Kothera *et al.* [17] provided reasonable preliminary estimates of quasi-static force vs. contraction for the small-scale PAM used in this study. As suggested by these researchers, the force produced by the actuator can be predicted based on force balance methods and derived using the free-body diagram shown in Figure 2.6. From this diagram, the equilibrium equations in the *x*- and *z*-directions are, respectively,

$$PRL = \sigma_x tL + NT\cos\alpha \tag{5}$$

and

$$F + \pi R^2 P = \sigma_z A_B + T \sin\alpha \tag{6}$$

where R is the instantaneous bladder outer radius, σ is the stress in the bladder (in the x- or z-direction as noted by the subscript), t is the instantaneous thickness of the bladder, T is the tension in the braided sleeve fiber, F is the total longitudinal force exerted by the PAM, and A_B is the bladder cross-sectional area.

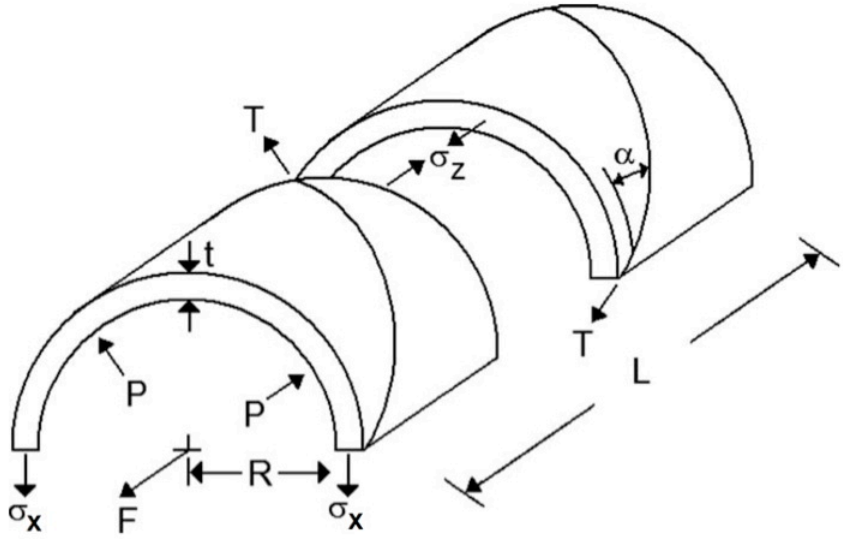

Figure 2.6. Free-body diagram used in the force balance model derivation [modified from Ref. 17].

Assuming a constant bladder volume (V_B), the bladder cross-sectional area can be written as $A_B = V_B/L$. Furthermore, the instantaneous bladder thickness can be calculated as

$$t = R - \sqrt{R^2 - \frac{V_B}{\pi L}}\,. \tag{7}$$

Solving Equation (5) for T and substituting the expression into Equation (6), the force in the PAM can then be written as

$$F = -\pi R^2 P + \sigma_z \frac{V_B}{L} + \frac{PRL - \sigma_x tL}{N\cos\alpha}\sin\alpha \,. \tag{8}$$

Using the geometric constraints provided in Equations (2) and (3), it is possible to rewrite this expression in the following manner

$$F = -\pi R^2 P + \sigma_z \frac{V_B}{L} + \frac{PRL - \sigma_x tL}{N} \frac{B}{\pi 2RN} \frac{L}{B} \tag{9}$$

where substitutions have been made for $\cos\alpha$ and $\sin\alpha$, and $2R$ has been used in place of D. Simplifying this expression, and grouping like terms, the force in the PAM can then be written as

$$F = P\left(\frac{L^2}{2\pi N^2} - \pi R^2\right) + \sigma_z \frac{V_B}{L} - \frac{\sigma_x tL^2}{2\pi N^2 R} \,. \tag{10}$$

Again using the geometric constraints expressed in Equations (2) and (3) and the trigonometric identity that $\sin^2\alpha + \cos^2\alpha = 1$, it is possible to write the instantaneous bladder outer radius as

$$R = \frac{\sqrt{B^2 - L^2}}{2\pi N} \tag{11}$$

then substitute this expression for R into the first term in Equation (10) such that the force is now given by

$$F = \frac{P}{4N^2\pi}\left(3L^2 - B^2\right) + \sigma_z \frac{V_B}{L} - \frac{\sigma_x tL^2}{2\pi N^2 R} \,. \tag{12}$$

At this point, it should be observed that the first term is now equivalent to the Gaylord force term (F_G) from Equation (4), and the remaining terms are corrections that account for elasticity in the bladder.

Moving forward, previous derivations of this model assumed that the bladder was a linear elastic material [16-17]. However, this assumption fails to capture the nonlinear response of the actuator and does nothing to predict the stiffening in the bladder at high radial strains that was demonstrated during the experimental characterization of these small-scale PAMs. In order to account for this behavior, the bladder material was assumed to be a nonlinear elastic material in both the *x*- and *z*-directions such that the stress (σ) is given by

$$\sigma = \sum_{k=1}^{M} E_k \varepsilon^k \tag{13}$$

where ε is the strain in the bladder and the modulus values (E_k) are design variables that are identified from empirical data at each operating pressure in order to minimize the error between the model and the experimental results. The summation upper limit (M) defines the order of the material model and is chosen by the researcher such that the model is robust enough to capture the full behavior of the actuator. The strains are defined as in the original force balance model developed by Ferraresi *et al.* [16] as

$$\varepsilon_x = \frac{\Delta R}{R_0} = \frac{R - R_0}{R_0} = \frac{R}{R_0} - 1 \tag{14}$$

and

$$\varepsilon_z = \frac{\Delta L}{L_0} = \frac{L - L_0}{L_0} = \frac{L}{L_0} - 1 \tag{15}$$

where ΔR is the change in bladder outer radius and R_0 is the initial bladder outer radius. Substituting this stress vs. strain constitutive material relationship into Equation (12), the force in the PAM is

$$F = \frac{P}{4N^2\pi}\left(3L^2 - B^2\right) + \frac{V_B}{L}\sum_{k=1}^{M} E_k\left(\frac{L}{L_0} - 1\right)^k - \frac{tL^2}{2\pi N^2 R}\sum_{k=1}^{M} E_k\left(\frac{R}{R_0} - 1\right)^k . \quad (16)$$

The first term in this model is the basic Gaylord force term (F_G) as before, while the second two terms are correction terms identified through the use of a nonlinear elastic model in conjunction with the force balance derivation. Labeling these additional two correction terms, collectively, as F_{NLFB}, the overall PAM force presented in Equation (16) can be written as $F = F_G + F_{NLFB}$.

It should also be noted that if a linear elastic model (M = 1) is used in Equation (16), the model proposed here simplifies to the force balance model derived by previous researchers [16-17]:

$$F = \frac{P}{4N^2\pi}\left(3L^2 - B^2\right) + E_1 V_B\left(\frac{1}{L_0} - \frac{1}{L}\right) - \frac{E_1 tL^2}{2\pi N^2}\left(\frac{1}{R_0} - \frac{1}{R}\right) \quad (17)$$

where E_1 is simply the elastic modulus of the silicone bladder, assumed constant over all operating pressures. In this case the two additional force correction terms added to the Gaylord force are referred to collectively as F_{LFB} such that the overall PAM force in Equation (17) is given by $F = F_G + F_{LFB}$. As will be demonstrated in *Section 2.4.5*, a much more accurate prediction of PAM behavior can be obtained through the use of the nonlinear elastic material model by selecting $M > 1$ in Equation (16).

2.4.3. Friction Force Model

In order to fully capture the actuation behavior of the small-scale PAMs, an additional force correction term is required to account for the friction between PAM components such that the hysteresis loop exhibited in the experimental characterization data can be accurately represented. Previous researchers have investigated several

methods to account for this behavior, including the use of a fixed friction force [5], a friction force calculated from a static friction model for interactions between the braid fibers at a micromechanical level [13-14,18], and a friction force directly proportional to the PAM force [2]. A more comprehensive review of friction and hysteresis modeling within PAM research is offered in Ref. [19].

Given the simplicity and accuracy of the friction model suggested by Woods *et al.* [2], a similar term has been proposed for use with the nonlinear elastic force balance model derived above. For this correction term, the friction force (F_F) opposes the PAM motion such that the friction reduces the overall PAM force during contraction (when the actuator is considered to be moving with positive velocity, v) and increases overall PAM force during extension (when velocity is considered negative). In this model, the magnitude of the friction force is proportional to the magnitude of the PAM force, and is thus calculated as

$$F_F = -k_F \left(F_G + F_{NLFB} \right) \mathrm{sgn}\left(v \right) \tag{18}$$

where k_F is an empirically fit friction factor. For the PAM used in this study, k_F decreased linearly with actuation pressure, ranging from 0.14 at 207 kPa down to 0.04 at 552 kPa. Combining the friction force from Equation (18) with the nonlinear elastic force balance model given in Equation (16), the full PAM actuation force proposed in this study is now given by $F = F_G + F_{NLFB} + F_F$.

2.4.4. Global Model Corrections

2.4.4.1 Pressure Deadband

Not included in the initial formulation of the aforementioned PAM force model was a global correction (i.e. one that is applied to all applicable terms) to account for the initial pressure required for the bladder to make substantial contact with the surrounding braid and initiate inflation of the PAM [5,8,10,15]. In order to model the effects of this pressure deadband, the actuation pressure P is reduced as

$$P' = P - P_c \tag{19}$$

where P' is the corrected actuation pressure to be used in place of P in the PAM force model, and P_c is an empirically obtained term corresponding to the pressure at which the PAM initiates contraction. To validate the presence of this deadband and identify the correct value for P_c, the pressure-averaged blocked force (i.e. the maximum force exerted by the PAM, neglecting hysteresis effects, at each actuation pressure) is shown plotted against actuation pressure in Figure 2.7 for the entire range of pressures tested. As is evident from the figure, there is a strong linear correlation between blocked force and actuation pressure. With the visual aid of the linear trend line that has been plotted with the data, it is also clear that the PAM is unlikely to generate a blocked force until a minimum actuation pressure threshold has been reached, demonstrating the existence of the deadband [21]. This minimum pressure is given by the x-intercept of the linear trend line and is used as the pressure offset, P_c. For the particular PAM used in this study, P_c was determined to be 76.5 kPa (11.08 psi).

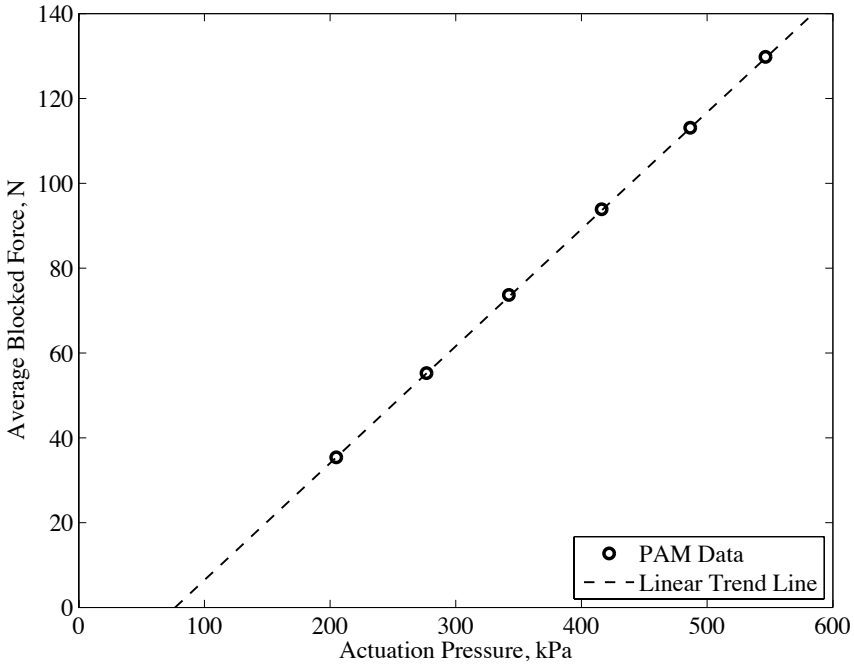

Figure 2.7 Blocked force as a function of actuation pressure with a linear trend line to demonstrate the presence of a pressure deadband.

2.4.4.2 Tip Effect Length Correction

A second global modification to the proposed model is the inclusion of a length correction term to account for the non-cylindrical shape of the actuator at the end fittings (as depicted in Figure 2.1 and Figure 2.3(b)). Instead, this and other previous models assume that the entire length of the actuator can be idealized as a right circular cylinder, while in reality the region of the PAM near the end fittings is rounded, which reduces the effective active length of the PAM. Using a corrected length term in place of the actual length significantly improved the model of the actuation diagram in previous PAM research [2,8,14-15,17,19], so this correction term has also been included in the model formulation used in this study. The tip shape, which can be modeled as a 90° circular arc following the methodology of Woods *et al.* [2], effectively reduces the length of the actuator at each end by

$$\Delta l = \left(\frac{\pi}{2} - 1\right)\left(R - R_0\right) \tag{20}$$

such that the corrected length is given by

$$L' = L - 2\Delta l \tag{21}$$

where *L'* is the corrected actuator length that is used in place of the true actuator length (*L*) in the PAM force model.

Incorporating these model improvements such that the previously described forcing terms in Equations (16) and (18) are a function of the corrected pressure and length where applicable, the model developed in this study is thus

$$F = F_G\left(P = P', L = L'\right) + F_{NLFB}\left(L = L'\right) + F_F\left(P = P', L = L'\right). \tag{22}$$

Unless explicitly stated otherwise, the model results presented in the following section are a function of the corrected pressure and length (*P'* and *L'*) in place of the measured values (*P* and *L*) where they appear in the original model expressions previously described in Equations (16) and (18).

2.4.5. Discussion of Modeling Results

As mentioned in *Section 2.4.2*, the proposed force balance model uses the nonlinear material elastic model given in Equation (13) with empirically identified modulus values (E_k). In order to achieve accurate results, the built-in MATLAB function *fmincon* (see Appendix A) was used to determine the optimum values of E_k at each operating pressure such that the error between the model output without friction force ($F_G + F_{NLFB}$) and the average force within the hysteresis loop (F_{AVG} as depicted in Figure 2.4) was a minimum. This process was carried out for increasingly higher order material models (i.e. increasing *M*) until the model was able to accurately capture the PAM

behavior at each operating pressure, neglecting hysteresis effects. In this optimization, the objective function that was minimized by the MATLAB solver is a normalized least squares regression error given by

$$Error = \sum_i \left(\frac{\left(F_G + F_{NLFB}\right)_i - \left(F_{AVG}\right)_i}{\left(F_{AVG}\right)_i} \right)^2 \tag{23}$$

where $(F_G + F_{NLFB})_i$ is the ith data point predicted by the model described in Equation (16), and $(F_{AVG})_i$ is the ith data point given by the average between the upper and lower hysteresis curves within the actual experimental data set (see Figure 2.4).

The results of the proposed nonlinear elastic force balance model are shown with respect to F_{AVG} in Figure 2.8, demonstrating the impact of increasing the summation upper limit (M) on the accuracy of the model. For clarity, only the results from the 414 kPa data set are shown plotted, but the results at each operating pressure demonstrated similar trends. Figure 2.8(a) also shows the results of the non-optimized linear force balance model (proposed by previous researchers and presented again in Equation (17))[16-17]. From Figure 2.8(a), it is apparent that a linear elastic material model (M = 1) is unable to capture the response of these miniature PAMs. Both the non-optimized linear force balance model (in which E_1 is constant across all pressures) and the optimized linear elastic model (in which E_1 is pressure-dependent and has been optimized over the linear elastic portion of PAM contraction from $0 < \Delta L/L_0 < 0.04$) vastly over-predict the PAM force capabilities at contractions above 4%. Within the linear elastic portion of PAM contraction (below $\Delta L/L_0 = 0.04$), however, the optimized linear elastic model clearly yields a more accurate prediction. Given the large errors associated with the linear elastic model, the accuracy of using a quadratic elastic model (M = 2) was next

evaluated, with the output of the model shown with respect to F_{AVG} in Figure 2.8(b). In this figure, the results of E_k optimized over both the linear elastic portion of PAM contraction ($0 < \Delta L/L_0 < 0.04$) and over the entire contractile range are shown. For both optimization ranges, it is evident that although the quadratic elastic model produces more accurate results than the linear elastic model shown in Figure 2.8(a), this model still lacks the robustness required to capture the miniature PAM behavior throughout actuation. Continuing in this manner, the order of the material model from Equation (13) was increased to $M = 3$ (results not shown) and ultimately to $M = 4$, with the output from the quartic elastic model ($M = 4$) finally producing satisfactorily accurate correlation between the model and the pressure-averaged experimental data for the small-scale PAM's full contractile range, as shown in Figure 2.8(c).

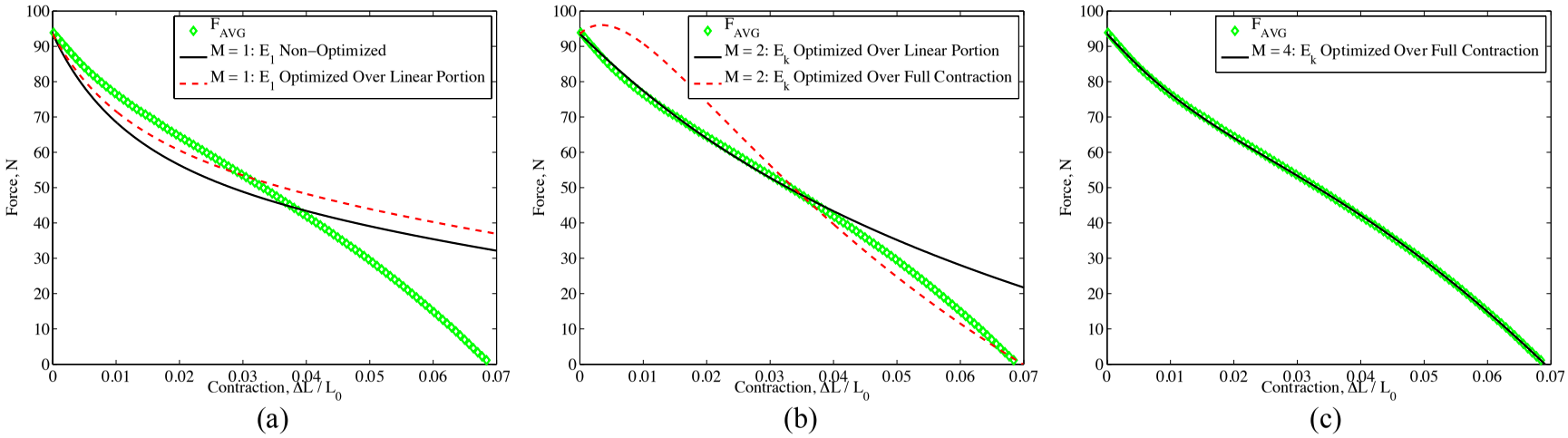

Figure 2.8 Force balance model results compared with experimental data (F_{AVG}) at an operating pressure of 414 kPa. (a) Linear elastic model results (M = 1) for E_1 non-optimized and E_1 optimized over the linear elastic portion of PAM contraction. (b) Quadratic elastic model results (M = 2) for E_k optimized over the linear elastic portion of PAM contraction and E_k optimized over the full PAM contractile range. (c) Quartic elastic model results (M = 4) for E_k optimized over the full PAM contractile range.

As a complement to the results shown in Figure 2.8, it is also interesting to consider the physical nature of the constitutive material relationship implied by the non-optimized linear elastic model and the optimized elastic models. To that end, Figure 2.9 shows the bladder stress-strain curves associated with the linear elastic material models (M = 1, both non-optimized and optimized) and the quartic material model (M = 4) that was ultimately shown to deliver accurate force predictions. Here, the stress-strain relationship has been calculated as in Equation (13) using the corresponding values of E_k for each model based on the 414 kPa test case. This relationship has been calculated up to a maximum strain of 1.1915, which corresponds to the highest radial strain experienced during testing at this pressure as defined in Equation (14) and calculated using instantaneous bladder radius values given in Equation (11). As implied by a linear elastic model, the results for M = 1 with both non-optimized E_1 and optimized E_1 suggest that stress in the bladder varies linearly with strain over the full range of motion of the PAM, which, based on actual miniature PAM behavior, is physically unlikely. Using the results of the optimization with the quartic elastic model (E_k with M = 4), however, the stress-strain curve indicates that the PAM bladder stiffens with increased strain, which is physically justifiable and yields excellent correlation with experimental results.

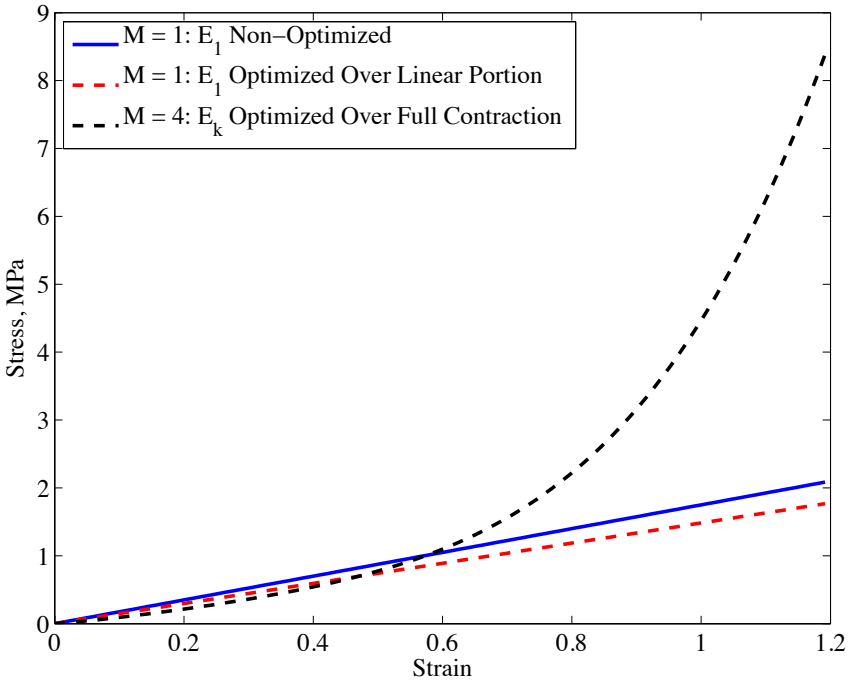

Figure 2.9 Stress-strain curves associated with a non-optimized linear elastic model and optimized elastic models for $M = 1$ and $M = 4$.

To further demonstrate the accuracy of the nonlinear elastic force balance model with $M = 4$, the results of this model ($F_G + F_{NLFB}$) with E_k empirically optimized for each actuation pressure are shown with respect to the pressure-averaged experimental data (F_{AVG}) in Figure 2.10(a) and with respect to the full experimental results in Figure 2.10(b). The PAM behavior predicted by the nonlinear elastic force balance model yields excellent agreement with the experimental data. As displayed in Figure 2.10, the model output at each actuation pressure very accurately predicts both the blocked force and free contraction capabilities of the miniaturized PAMs. Furthermore, the predicted actuator load lines nearly perfectly overlay the pressure-averaged data (Figure 2.10(a)) and thus bisect the hysteresis loops generated during the actual experimentation (Figure 2.10(b)), fully accounting for the inflection point in the experimental results at $\Delta L/L_0 = 0.04$. A

controlled actuation scheme could be formulated using this reconstructed quasi-static actuator diagram, which was a key objective of this study.

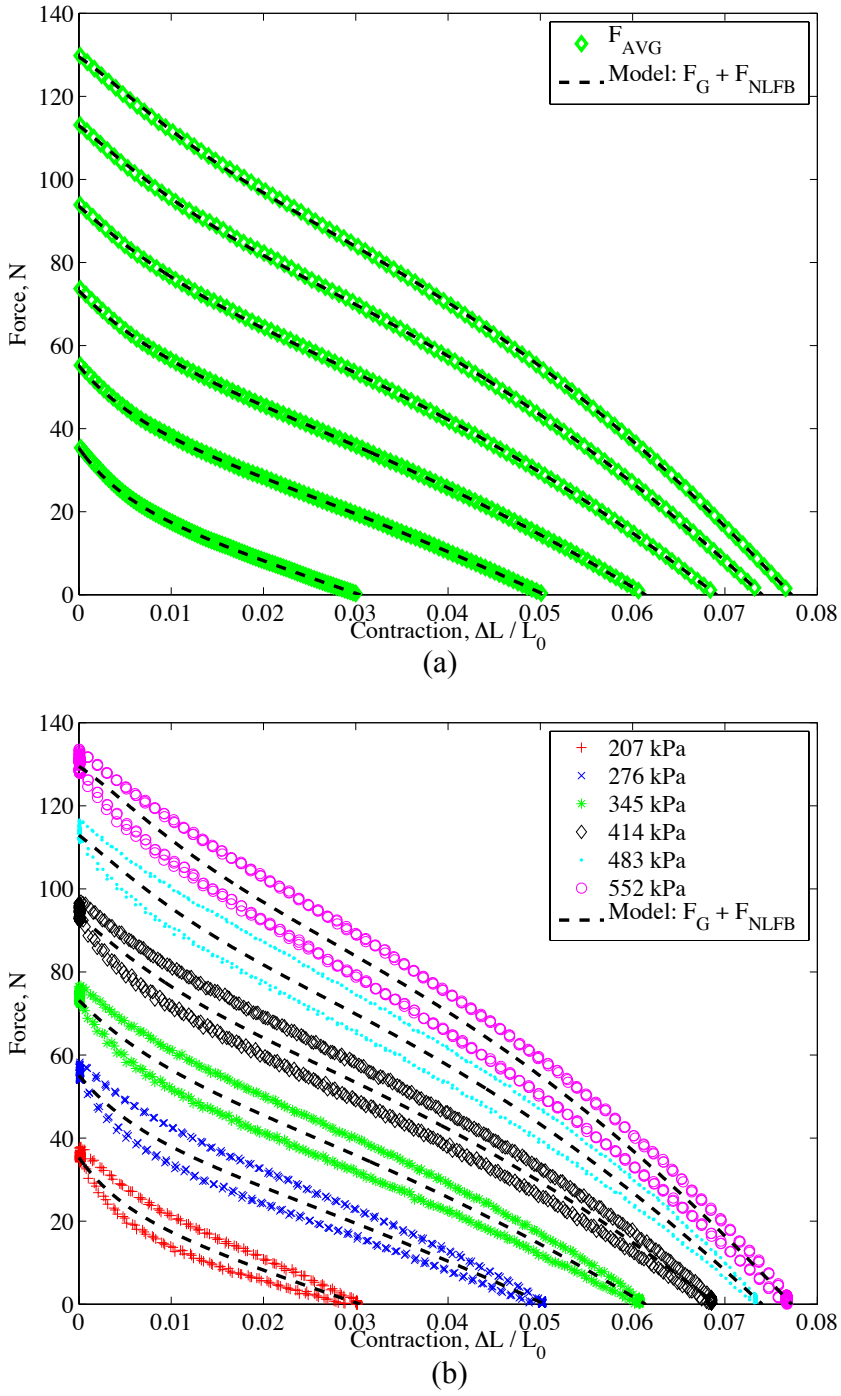

Figure 2.10 Results of nonlinear elastic force balance model (using $M = 4$) compared to (a) pressure-averaged experimental data and (b) full experimental results.

Looking specifically at the optimized values of E_k that are associated with the nonlinear elastic force balance model when $M = 4$, it is interesting to note that there are distinct trends in these elastic parameters as a function of PAM actuation pressure, $E_k(P)$, as shown in Figure 2.11. This is especially useful because these curves can be used to predict the optimum E_k values at operating pressures in between those at which the PAM was explicitly characterized through the aforementioned quasi-static testing. Using this approach, a lookup table for E_k can be developed (i.e. a spline fit of $E_k(P)$ over the full measured range of operating pressures), enabling more precise control of the PAM in any actuation scheme.

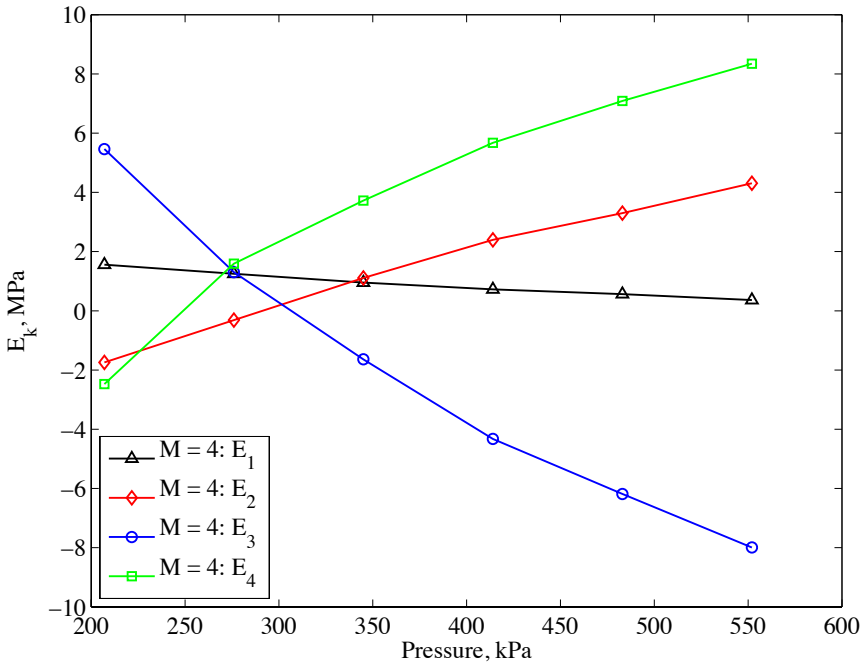

Figure 2.11 Optimum E_k as a function of pressure ($M = 4$).

To demonstrate the impact of the proposed model on the accuracy of miniature PAM force predictions, Figure 2.12 shows the progression in model capabilities from the basic Gaylord force model to the nonlinear elastic force balance model with global model

corrections (again using only the 414 kPa case for the sake of clarity). While Figure 2.12(a) shows the actual model output compared to the experimental results, Figure 2.12(b) shows the associated error between the model prediction (F_{MODEL}) and the experimental data. As these models neglected hysteresis, the experimental data used to calculate the error is the average force (F_{AVG}) as used above. The error at each contraction value has been calculated as

$$Error_i = \left| \frac{\left(F_{MODEL}\right)_i - \left(F_{AVG}\right)_i}{F_B} \right| \tag{24}$$

where F_B is the pressure-averaged blocked force.

As is evident in Figure 2.12, the Gaylord force by itself (F_G) only provides a poor estimate of the blocked force and greatly over-predicts PAM contraction. Upon including the global corrections for pressure deadband and length ($F_G(P', L')$), the model yields a much more accurate prediction of blocked force, but still fails to capture the appropriate loss in PAM force with increasing contraction. Using the basic linear elastic force balance model used by Ferraresi *et al.* [16] and again by Kothera *et al.* [17], that is $F_G(P', L') + F_{LFB}(L')$, the model is able to more closely forecast the PAM force, although it tends to under-predict the PAM output at low contractions and severely over-predict the force at higher contractions. Finally, the nonlinear elastic force balance model proposed in this study, $F_G(P', L') + F_{NLFB}(L')$, shown here using $M = 4$, is able to fully capture the PAM actuation behavior and predict the PAM force (neglecting hysteresis) with an average error of only 0.17% and a maximum error of 0.50% with respect to F_B. Across all of the actuation pressures tested (not shown graphically), the average error associated

with the nonlinear elastic force balance model was 0.18%, with a maximum error of 1.19% experienced during the 207 kPa test case.

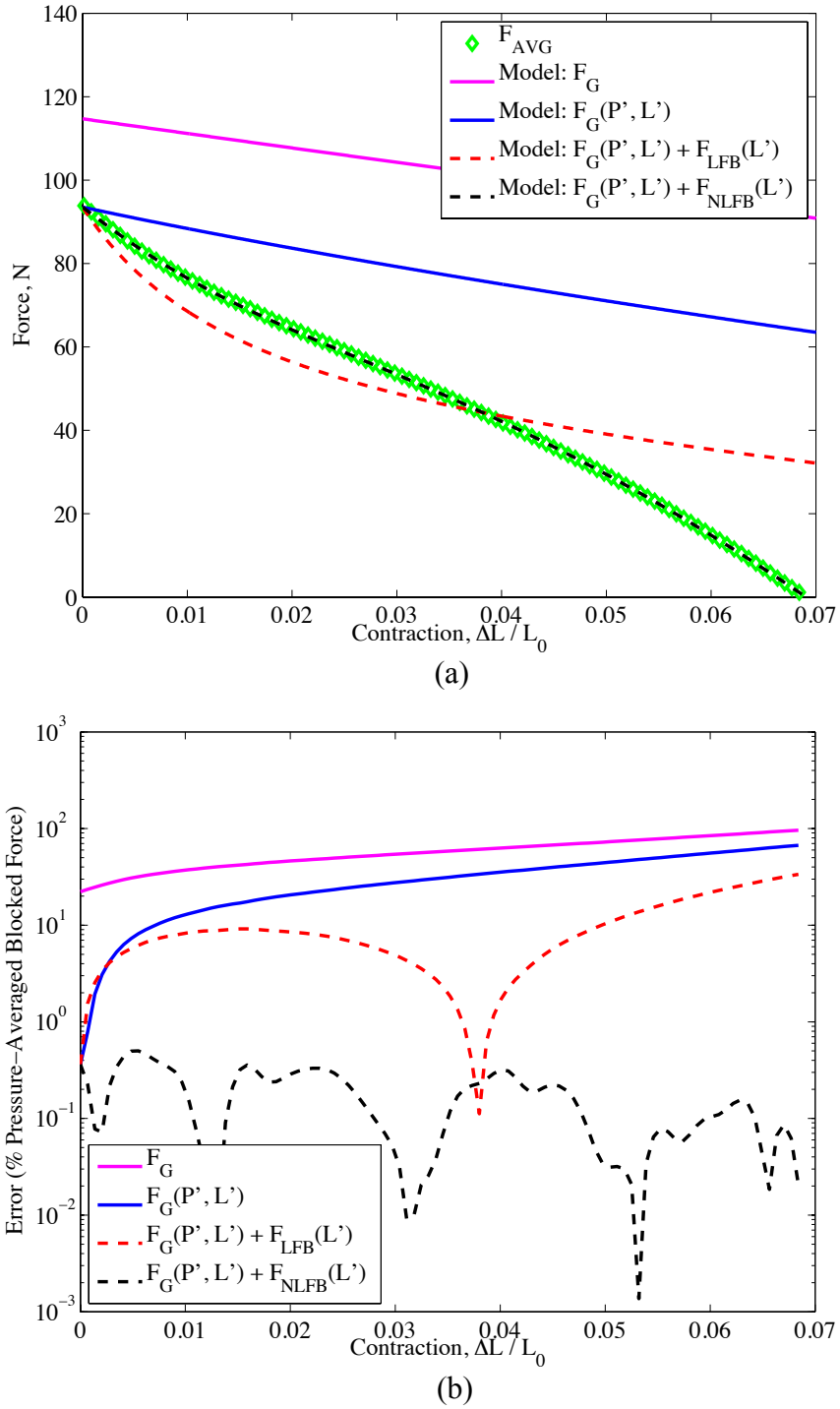

Figure 2.12 Progressive accuracy of modeling techniques for the 414 kPa case. (a) Model output compared to experimental data. (b) Associated model error (%).

Having verified the accuracy of the nonlinear elastic force balance model in predicting the average PAM force at each pressure, the next phase of the model validation process was to incorporate the friction force term as proposed in Equation (18) in order to fully capture the hysteretic nature of the PAM actuation. The output of the full PAM force model ($F_G + F_{NLFB} + F_F$) is shown with respect to the experimental data in Figure 2.13. Here it is evident that the proposed model accurately predicts the PAM force as a function of actuation pressure, PAM contraction, and PAM direction of motion, fully encompassing all aspects of the nonlinear actuation behavior of the miniature PAM.

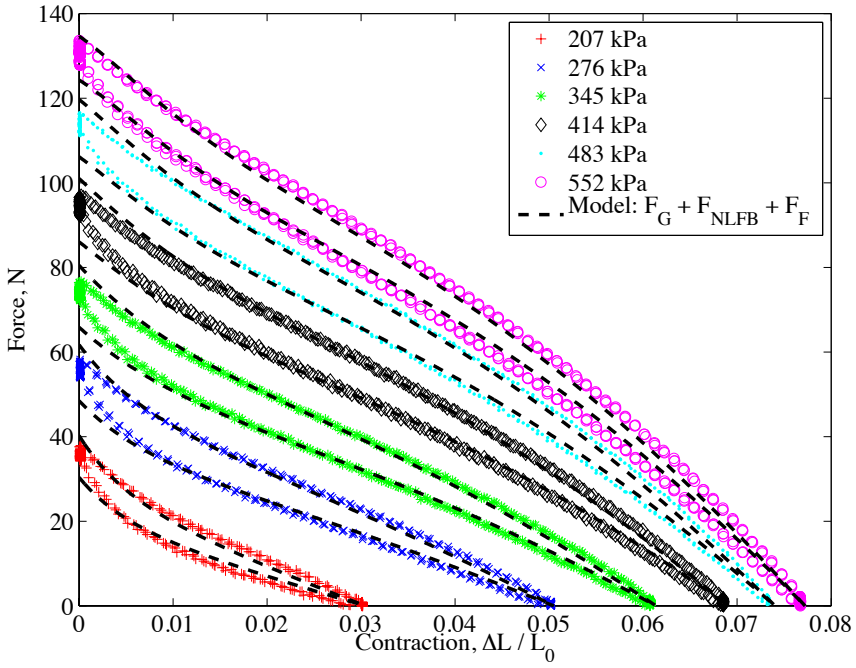

Figure 2.13 Full force model ($F_G + F_{NLFB} + F_F$) compared to experimental data.

2.4.6. Impact of Length Correction Term on Modeling Efforts

Although the nonlinear elastic force balance model was presented above with the inclusion of the corrected length term (L') in place of the actual length (L), the necessity of including the corrected length in conjunction with the optimized model was re-evaluated in this study. Given that the error minimization routine used to generate the appropriate values of $E_k(P)$ at each actuation pressure tailors these design variables to allow a precise fit to the pressure-averaged experimental data, it was hypothesized that the length correction would not substantially affect the accuracy of the model, if at all. In order to validate this hypothesis, the results of the nonlinear elastic force balance model ($F_G + F_{NLFB}$) are shown with respect to the pressure-averaged experimental data (F_{AVG}) both with and without the corrected length term in Figure 2.14(a), along with the associated error as calculated using Equation (24) in Figure 2.14(b). For clarity, only the error results of the 414 kPa operating pressure case have been included in Figure 2.14(b). From these figures, it is clear that the inclusion of the corrected length term has very little impact on the fit of the model for PAMs at this scale. In fact, across all of the operating pressures tested, the average error associated with the model including the corrected length was 0.18%, while that corresponding to the model without the corrected length was only 0.16%. As such, the inclusion of the length correction term is left to the discretion of the researcher, and it may be neglected in order to simplify the model. Further research must be conducted to verify whether this holds true for full-scale PAMs as well.

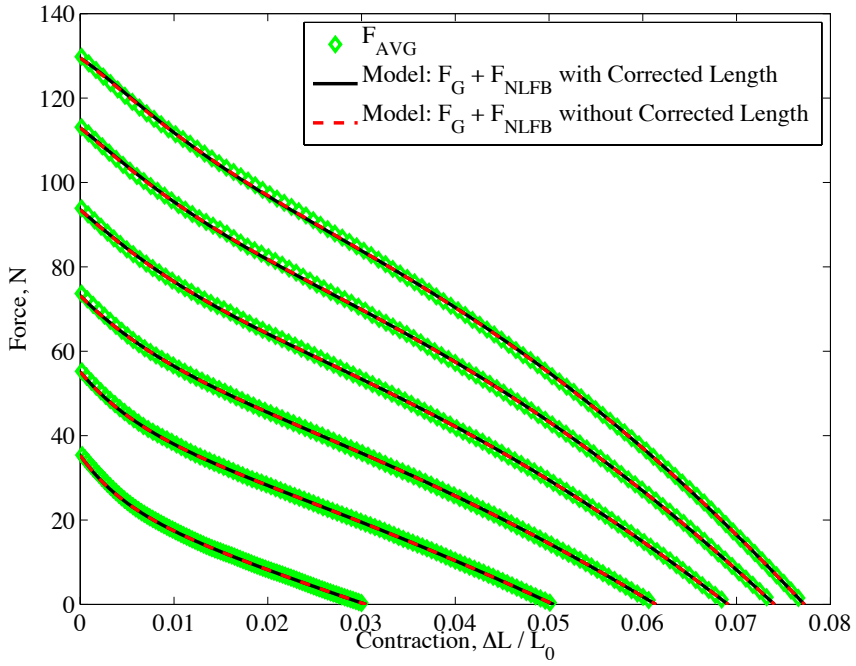

(a)

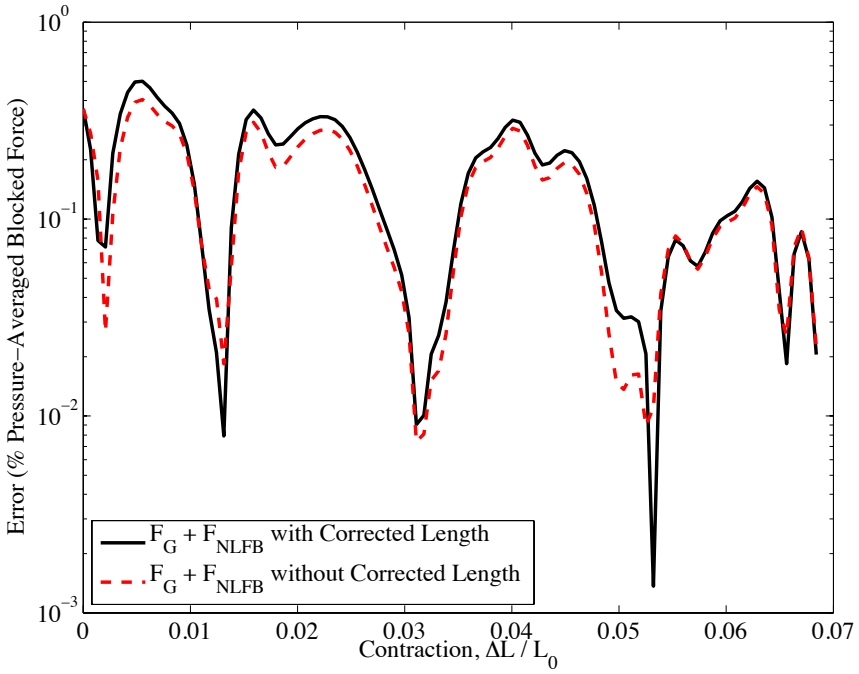

(b)

Figure 2.14 Nonlinear elastic force balance model with and without corrected length. (a) Model output compared to pressure-averaged experimental data. (b) Associated model error (%) for 414 kPa case only.

2.5. Conclusions

In this study, a miniature pneumatic artificial muscle (PAM) was fabricated, experimentally characterized, and analyzed so that it may be used as an actuator in a small-scale mechanical system. The key developments of this study are the following:

1. Miniature PAMs were constructed with commercially available materials using a highly repeatable manufacturing process that could be applied to PAMs having diameters ranging from 3 – 4.25 mm (0.118 to 0.167 in), allowing for the production of a low-cost miniature actuator that performed consistently well.
2. The experimental characterization on a single miniature PAM demonstrated the quasi-static behavior of the PAM when actuated using compressed air, highlighting the nonlinear nature of the actuator. In particular, three key nonlinear phenomena were observed: nonlinear PAM stiffness, hysteresis of the force vs. displacement response, and a pressure deadband. Nonlinear PAM stiffness is attributed to stiffening in the silicone bladder that occurred at high strains, ultimately limiting the radial expansion, and thus axial contraction, of the PAM. Hysteresis is caused by friction between the actuator components. Both nonlinear stiffening and hysteresis are a function of actuation pressure. The pressure deadband, however, is a fixed amount across all operating pressures that refers to the threshold pressure at which the PAM actuation is initiated.

3. A series of nonlinear model refinements were proposed for use with a previously derived force balance analysis to address each nonlinearity in turn. To account for PAM stiffening, a nonlinear elastic model was used wherein stress was expressed as a quartic polynomial of strain. The optimized modulus coefficients trend well with pressure and can be expressed as spline fits for a lookup table of coefficient values, $E_k(P)$. Hysteresis in the force vs. displacement curves was modeled using an empirical friction factor that was linearly dependent on pressure, and thus also suitable for a lookup table. To address the pressure deadband, a uniform pressure offset term was incorporated into the model. With the inclusion of these three refinements, the proposed PAM force model demonstrated excellent agreement with experimental results.
4. Additional model analysis revealed that the inclusion of the length correction term to account for the non-cylindrical tip shape of the PAM did not significantly impact the accuracy of the nonlinear elastic force balance model.

In conclusion, the nonlinear elastic force balance model proposed in this study offers a revolutionary analysis method for use with miniature PAMs. As this model is able to fully account for several key nonlinearities in the actuator behavior, it will be instrumental for developing accurate quasi-static actuation strategies for small-scale PAMs. Furthermore, this new model has the potential to be useful in full-scale PAM research as well, although additional testing and analysis will need to be conducted in order to verify the applicability of the model at a larger scale.

2.6. References

[1] Vocke III, R. D., Kothera, C. S., Chaudhuri, A., Woods, B. K. S., and Wereley, N. M., 2012, "Design and Testing of a High-specific Work Actuator Using Miniature Pneumatic Artificial Muscles," J. Intell. Mater. Syst. Struct., **23**(3), pp. 365–378. DOI: 10.1177/1045389X11431743

[2] Woods, B. K. S., Kothera, C. S., and Wereley, N. M., 2011, "Wind Tunnel Testing of a Helicopter Rotor Trailing Edge Flap Actuated via Pneumatic Artificial Muscles," J. Intell. Mater. Syst. Struct., **22**(13), pp. 1513–1528. DOI: 10.1177/1045389X11424216

[3] Woods, B. K. S., 2012, "Pneumatic Artificial Muscle Driven Trailing Edge Flaps for Active Rotors," Ph.D. Thesis, University of Maryland, College Park.

[4] Caldwell, D., Tsagarakis, N., and Medrano-Cerda, G. A., 2000, "Bio-mimetic Actuators: Polymeric Pseudo Muscular Actuators and Pneumatic Muscle Actuators for Biological Emulation," Mechatronics, **10**(4–5), pp. 499–530. DOI: 10.1016/S0957-4158(99)00071-9

[5] Chou, C., and Hannaford, B., 1994, "Static and Dynamic Characteristics of McKibben Pneumatic Artificial Muscles," *Proc. of ICRA*, **1**, pp. 281–286.

[6] Woods, B. K. S., Gentry, M. F., Kothera, C. S., and Wereley, N. M., 2011, "Fatigue Life Testing of Swaged Pneumatic Artificial Muscles as Actuators for Aerospace Applications," J. Intell. Mater. Syst. Struct., **23**(3), pp. 327–343. DOI: 10.1177/1045389X11433495

[7] Chen, Y., Yin, W., Liu, Y., and Leng, J., 2011, "Structural Design and Analysis of Morphing Skin Embedded with Pneumatic Muscle Fibers," Smart Mater. Struct., **20,** 085033 (8pp). DOI: 10.1088/0964-1726/20/8/085033

[8] De Volder, M., Moers, A. J. M., and Reynaerts, D., 2011, "Fabrication and Control of Miniature McKibben Actuators," Sensors Actuat. A, **166**(1), pp. 111–116. DOI: 10.1016/j.sna.2011.01.002

[9] Birch, M. C., *et al.*, 2001, "A Miniature Hybrid Robot Propelled by Legs," *Proc. of the 2001 IELE/RSJ Int. Conf. on Intelligent Robots and Systems,* **2**, pp. 845–851.

[10] Solano, B., and Rotinat-Libersa, C., 2011, "Compact and Lightweight Hydraulic Actuation System for High Performance Millimeter Scale Robotic Applications: Modeling and Experiments," J. Intell. Mater. Syst. Struct., **22**(13), pp. 1479–1487. DOI: 10.1177/1045389X11418860

[11] Tiwari, R., Meller, M. A., Wajcs, K. B., Moses, C., Reveles, I., and Garcia, E., 2012, "Hydraulic Artificial Muscles," J. Intell. Mater. Syst. Struct., **23**(3), pp. 301–312. DOI: 10.1177/1045389X12438627

[12] Gaylord, R., 1958, "Fluid Actuated Motor System and Stroking Device," U.S. Patent No. 2,844,126.

[13] Schulte, H. F., Adamski, D. F., and Pearson, J. R., 1961, "Characteristics of the Braided Fluid Actuator," Report at Department of Physical Medicine and Rehabilitation, the University of Michigan, Ann Arbor, MI, pp. 105–120.

[14] Tondu, B., and Lopez, P., 2000, "Modeling and Control of McKibben Artificial Muscle Robot Actuators," IEEE Control Systems Magazine, **20**(2), pp. 15–38. DOI: 10.1109/37.833638

[15] Tsagarakis, N., and Caldwell, D., 2000, "Improved Modeling and Assessment of Pneumatic Muscle Actuators," *Proc. of ICRA*, **4**, pp. 3641–3646.

[16] Ferraresi, C., Franco, W., and Bertetto, A. M., 2001, "Flexible Pneumatic Actuators: A Comparison Between the McKibben and the Straight Fibres Muscles," J. Robot. Mechatron., **13**(1), pp. 56–63.

[17] Kothera, C. S., Jangid, M., Sirohi, J., and Wereley, N. M., 2009, "Experimental Characterization and Static Modeling of McKibben Actuators," ASME J. Mech. Des., **131**, 091010 (10pp). DOI: 10.1115/1.3158982

[18] Davis, S., and Caldwell, D., 2006, "Braid Effects on Contractile Range and Friction Modeling in Pneumatic Muscle Actuators," Int. J. Robot. Res., **25**(4), pp. 359–369.

[19] Tondu, B., 2012, "Modelling of the McKibben Artificial Muscle: A Review," J. Intell. Mater. Syst. Struct., **23**(3), pp. 225–253. DOI: 10.1177/1045389X11435435

[20] Diani, J., Fayolle, B., and Gilormini, P., 2009, "A Review on the Mullins Effect," Eur. Polym. J., **45**(3)**,** pp. 601–612. DOI: 10.1016/j.eurpolymj.2008.11.017

[21] Gelb, A., and Vander Velde, W. E., 1968, *Multiple-input Describing Functions and Nonlinear System Design*, McGraw-Hill, New York, pp. 4–5, Chap. 1.

3. Push-PAM Development and Analysis

3.1. Introduction

Pneumatic artificial muscles (PAMs) are simple mechanical actuators that harness pressurized air to generate significant forces and deflections, while offering several advantages over other actuation technologies. They are known for their high power-to-mass, power-to-volume, and work-to-mass ratios, making them more attractive than electromechanical actuators, solenoids, piezoelectric and magnetostrictive materials, and several other types of actuators in a variety of applications [1-5]. Furthermore, they boast a very simple structure, high durability and fatigue life, and are compliant and thus safe for human interaction and tolerant of mechanical misalignment and impulsive loading [6]. As a result of these characteristics, they have attracted interest in a wide array of fields, including prosthetics/orthotics [7-8], robotics [9-10], and recently aerospace engineering [4-6,11-12]. A more comprehensive review of some of the applications of PAMs is undertaken by Zhang and Philen in Ref. [13].

These simple, yet effective, devices are comprised of a flexible elastomeric bladder surrounded by a braided sleeve, with two end fittings that serve to seal the ends of the PAMs and create a channel for the injection of the working fluid. The operating principle of PAMs is as follows. The inner elastic bladder is pressurized with air, causing an inflation and expansion of the bladder, which causes a subsequent expansion in the surrounding braided sleeve. Because the braided sleeve fibers are much stiffer than the bladder material, the braided sleeve is unable to stretch as the bladder does and instead contracts or extends axially by an amount ΔL to allow for the expansion in the bladder. In

addition to the relative motion between the two end fittings, the stiff sleeve fibers generate either a tensile or compressive force along the main axis of the actuator, corresponding to either an axial contraction or extension, respectively. For a contraction/tension actuator, the bladder expansion is primarily radial. Conversely, for an extension/compression PAM, the bladder expansion is primarily axial [14].

The direction of force and motion are dependent on the initial angle between the filaments of the braided sleeve, which is inherent to the construction of a given actuator and cannot be changed once the actuator is made. Actuators with the filaments aligned primarily with the longitudinal axis of the actuator will be contractile and generate a tensile force. If the filaments of the sleeve are aligned primarily with the radial axis of the actuator, then the resulting motion is extensile and the force generated will be compressive. There is a neutral braid angle between these two extremes that is the crossover point between these regimes. This angle has been found to be 35.26° as measured from the radial axis to the braid filaments, or more commonly reported as 54.74° as measured from the longitudinal axis [14-16]. The vast majority of PAMs studied by previous researchers have the braid configured to generate tensile forces and contractile motions [1-12,16-24]. Although extensile PAMs are capable of producing large axial deformations, they generate low compression forces and are prone to buckling when subjected to axial compressive loading [6,14-15,25-26], and are thus seldom used as actuators.

Despite the apparent advantages of contractile PAMs, however, current and future uses of PAM actuators would benefit from a configuration that allows for comparable forces and stability in an extensile scheme. For example, an industrial stamping process

where an extensile actuator is needed to push two plates together, thereby creating a compressive force between them. As such, the goal of this study was to develop and characterize a novel PAM design, known as the push-PAM, which takes advantage of the higher forces of the contractile PAM and converts contraction to extension without sacrificing actuator performance or simplicity.

To this end, the remainder of the chapter is organized into four sections. First, the design and fabrication of the push-PAM will be discussed, highlighting its simplicity and similarity to the contractile PAM. The push-PAM will then be characterized through quasi-static testing to reveal the evolution of force with displacement associated with this device at a range of discrete internal pressures, and the results will be compared to those of a contractile PAM to demonstrate the push-PAM's analogous performance. Next, existing models for contractile PAMs will be validated against the experimental data from the push-PAM, showing that the output from both types of actuators may be captured through the same modeling scheme. Furthermore, these results will showcase the precision of a refined force balance model, which includes corrections to accurately capture the nonlinear actuation behavior of the PAMs, including a nonlinear stress vs. strain relationship, friction effects that contribute to hysteresis, and an actuation deadband at low operating pressures. The chapter will conclude with a summary of the findings of this study and a brief discussion of the significance of the work.

3.2. Design and Fabrication

As was alluded to in the previous section, the design goal of the proposed push-PAM was to harness the operational characteristics of a typical contraction/tension PAM, but change the direction of motion and force with a simple conversion package that

demands only a small increase in friction, weight, and cost. To accomplish this, a pushrod was anchored inside of the bladder of a contractile PAM to one of the end fittings. The pushrod extends through the inside of the actuator and passes through a rod seal and out of the other end fitting of the PAM, which is known as the fixed end fitting. This design mimics that which was proposed in Ref. [27].

Upon pressurization of the actuator, the PAM portion of the apparatus inflates and expands radially, causing relative contractile motion between the two PAM end fittings. Because the pushrod is of fixed length, this contraction within the PAM causes an extensile motion of the pushrod outside of the actuator through the fixed end fitting. As such, when the actuator is supported by the fixed end fitting and the external end of the pushrod, pressurization of the PAM results in an increase in the distance between the mounting points, and a compressive force is generated between them. So although the PAM itself still contracts by an amount ΔL, the pushrod and the specific mounting arrangement change this relative contraction into an overall ΔL extension. This is demonstrated in Figure 3.1, which shows a schematic of the push-PAM in its resting and actuated states (top and bottom, respectively), with the mounting points marked with a red dashed line. Through this configuration, the push-PAM device allows for the superior force generation capabilities of a contractile PAM to be utilized in an extension/compression scheme.

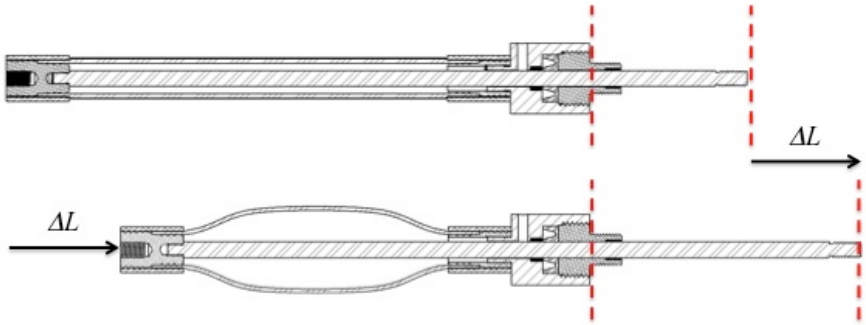

Figure 3.1 Schematic of a push-PAM is its resting (top) and actuated (bottom) configurations.

Given that the push-PAM design makes explicit use of a traditional contractile PAM, the manufacturing techniques used for these two types of actuators are nearly identical. For this study, both the contractile PAM and the push-PAM utilized a latex bladder, a Kevlar braided sleeve, and swaged aluminum end fittings [6]. For the contractile PAM, a thru hole in one of the end fittings served as a conduit for the air during pressurization. For the push-PAM, the air inlet was incorporated into the free end of the PAM utilizing a series of holes around the attachment point of the pushrod. This configuration allowed for a high mass flow rate of air into the PAM, while also simplifying the design of the fixed end fitting, which attached to the rod housing. In order to provide a good baseline for comparison during experimental characterization, both the contractile PAM and the push-PAM were designed and manufactured to have matching resting configurations (i.e. braid angle, length, and diameter). The physical actuators used in this study are pictured in Figure 3.2 to show the similarities between the PAMs used for each type of device (contractile PAM on top, push-PAM on bottom).

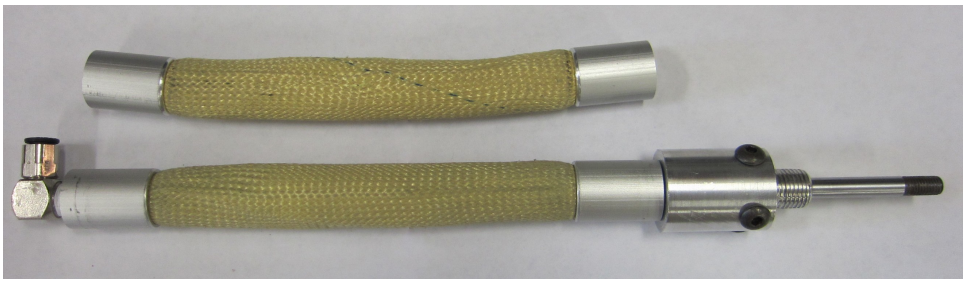

Figure 3.2 Both types of actuators characterized in this study (traditional contractile PAM on top, novel push-PAM for extensile motion on bottom).

3.3. Experimental Characterization

3.3.1. Experimental Procedure

In order to characterize and compare the performance of the contractile PAM and the push-PAM, the actuators underwent quasi-static testing using a 97.9 kN (22 kip) MTS servo-hydraulic test machine, which provided both displacement and force measurements during testing. The PAMs were pressurized with a Husky Pro 227 L (60 gal) air compressor. Meanwhile, a Wilkerson Dial-Air pressure regulator with an SSI Technologies, Inc. digital pressure gauge was used to precisely monitor the pressure supplied to the PAMs.

The overall goal of the experimental characterization was to determine the evolution of force with displacement for a range of internal pressures for both types of PAMs. This was achieved by first inflating each PAM to a specific pressure, ranging from 138 – 621 kPa (20 – 90 psi) in 69 kPa (10 psi) increments, with both attachment points fixed by the MTS grips. After holding momentarily at this condition, one of the MTS heads was unlocked, allowing the actuator to fully contract (or extend) to the point

where it ceased to exert a force. Finally, following another momentary hold, the actuator was then stretched (or compressed) back to its nominal resting length.

While this test procedure provided data to characterize each PAM's entire actuator load line, two additional points of interest that were also gleaned from this test were the blocked force and free contraction of the PAMs. The blocked force corresponds to the maximum amount of force that the PAM is able to exert at a given internal pressure, which occurs when the actuator is pressurized with both attachment points held fixed. Conversely, free contraction denotes the maximum stroke of the PAM for a given pressure, measured as the amount of contraction at which the PAM no longer produces any force. Although this terminology may seem misleading for the push-PAM because the full apparatus extends, rather than contracts, the conventional PAM nomenclature ("free contraction") has been also adopted to define the maximum stroke of the push-PAM because the device is still driven by the contractile performance of the PAM.

3.3.2. Discussion of Experimental Results

The results of the experimental characterization tests are shown in Figure 3.3 for the contractile PAM and the push-PAM described above, demonstrating each PAM's evolution of force with displacement at a series of discrete internal pressures. For clarity, only the results of the tests at 207, 414, and 621 kPa (30, 60, and 90 psi) are shown, with the contractile PAM results displayed with a red solid line, and the push-PAM results shown with a black dashed line. While the full experimental results are shown in Figure 3.3(a), the average actuator force at each pressure (F_{AVG}) is shown in Figure 3.3(b) to demonstrate the nature of the actuation without hysteresis effects, which will be

important for the modeling work discussed in later sections of this chapter. In both plots, the horizontal axis is a non-dimensional measure of PAM contraction given by

$$Contraction = \Delta L / L_0 \,. \tag{1}$$

In this equation, L_0 is the resting length of the PAM (otherwise known as the active length), and ΔL is the amount by which the device has contracted (or extended) as described above. For both the contractile PAM and the push-PAM, ΔL is taken to be positive for the desired motion of the actuator. In other words, for the contractile PAM, ΔL is positive when the actuator contracts. For the push-PAM, ΔL is positive when the pushrod extends as a result of the PAM contraction (see Figure 3.1).

The plots in Figure 3.3 clearly show that the contractile PAM and push-PAM demonstrate very similar actuation profiles, which is significant in asserting the practicality and usefulness of a push-PAM actuator. As can be seen in these figures, the forces generated by the PAMs are comparable at each actuation pressure, however the push-PAM is not quite able to achieve as much free contraction as the contractile PAM. The slight performance discrepancies between the two types of PAMs are most likely due to increased friction within the push-PAM as a whole as a result of the motion of the pushrod within the rod seal. Also, small differences in the fabrication of the two PAMs themselves may contribute to the slight disparity between the actuator load lines.

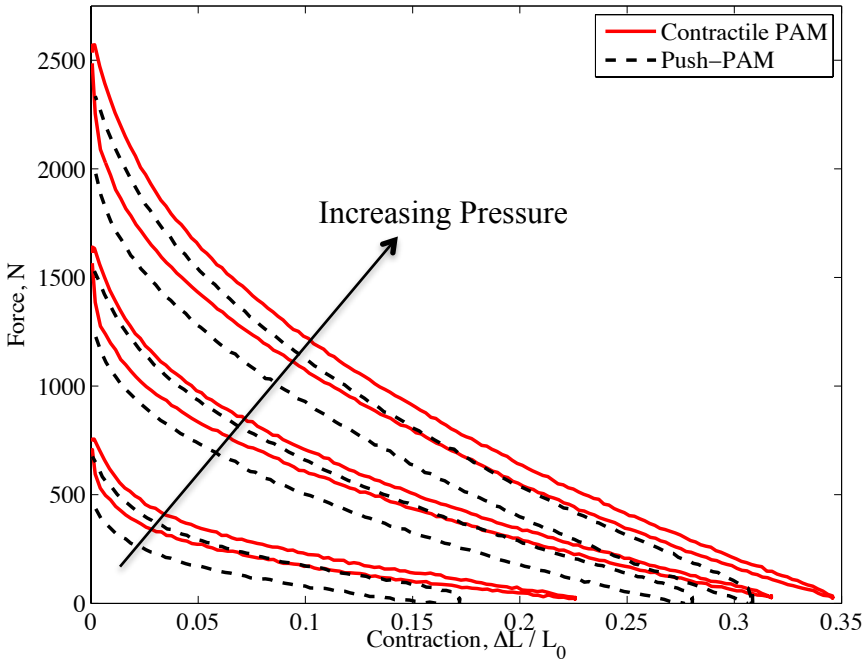

(a)

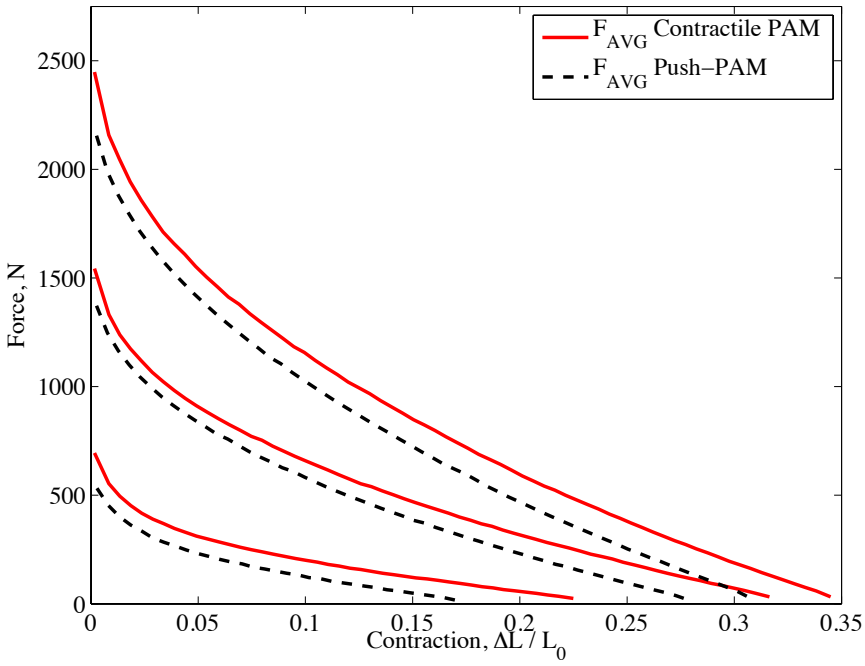

(b)

Figure 3.3 Experimentally characterized actuator load lines at operating pressures of 207, 414, and 621 kPa. (a) Full experimental results. (b) Average force within hysteresis loop.

Examining both sets of actuation profiles in Figure 3.3, the forces generated by the PAMs decrease with increasing displacement at each given pressure. However, the local slopes of the curves vary depending on the contraction of the actuator. Below about $\Delta L/L_0$ = 0.05, the force drops relatively quickly with increasing contraction, indicating that the PAMs are relatively stiff in this region. This is especially the case for the contractile PAM, whereas the push-PAM yields a slightly more gradual decrease in force at low displacements. Again, this discrepancy may be due to additional friction within the push-PAM that mitigates the initial jump in PAM force as the bladder inflates. Above $\Delta L/L_0$ = 0.05, the stiffness of the PAMs decrease and the forces diminish at a slower rate along a nearly linear path. For the contractile PAM, the nature of the actuation diagram appears to change again at contractions above $\Delta L/L_0$ = 0.15, with the stiffness of the PAM continuing to attenuate as the slope decreases further in this region. At these higher contractions (above $\Delta L/L_0$ = 0.05), it is possible that the latex bladder is being strained beyond the linear portion of a standard stress-strain curve and has entered a softening region in which additional strain causes a nearly negligible increase (or even decrease) in stress. Regardless of the exact characteristics of the PAM stiffness, however, it is clear that the PAM bladders are demonstrating nonlinear elastic behavior.

It is also important to note the aforementioned hysteresis in the actuator load lines (see Figure 3.3(a)), with the lower line corresponding to the path from blocked force to free contraction and the upper line corresponding to the return path. This hysteresis results primarily from friction between the components of the PAM. Typically, this refers to friction between the braid and the bladder during inflation and deflation, as well as friction between the individual fibers of the braid as the braid angle changes. For the

push-PAM, however, it is likely that friction between the pushrod and the rod seal also adds to the hysteretic nature of the diagram. As can be seen in Figure 3.3(a), the push-PAM demonstrates more hysteresis (i.e. the distance between the top and bottom curves is larger for the push-PAM than for the contractile PAM at a given pressure), bolstering the argument that there may be more friction in the push-PAM.

3.4. Modeling

Having proven the feasibility of creating a PAM that can extend an integrated pushrod, and having verified that such a push-PAM is capable of replicating large forces and displacements comparable to a contractile PAM, the next phase of this study was to demonstrate that a model is able to accurately predict the output of this new actuator. Because the push-PAM utilizes the same basic construction as the contractile PAM, my goal was to validate that both types of actuators may be modeled with the same sets of equations, further confirming the ease with which the push-PAM may be used as an alternative to the standard contractile PAM. As with all PAMs, the geometry of the braided sleeve plays a major role in determining the response of the actuator. From the braid angle α (taken from the radial plane of the actuator to the braid fibers), the current PAM length L (given by L_0 - ΔL), and the bladder outer diameter D, the following braid parameters can be calculated through geometric constraints:

$$B = \frac{L}{\sin\alpha} \tag{2}$$

and

$$N = \frac{B\cos\alpha}{\pi D} \tag{3}$$

where B is the length of one fiber and N is the number of turns the fiber makes around the bladder. For ease of measurement, the braid angle, length, and bladder outer diameter used to calculate B and N were measured while the PAM was in its resting state. Although the two PAMs used in this study were intended to be identical, there were slight differences between them as a result of manufacturing. For the contractile PAM, the initial braid angle was 74°, the resting length was 12.8 cm (5.05 in), and the initial bladder outer diameter was 1.59 cm (0.625 in). For the push-PAM, the initial braid angle was 73°, the resting length was 13.1 cm (5.16 in), and the initial bladder outer diameter was 1.59 cm (0.625 in).

3.4.1. Gaylord Force Model

Using these basic geometric constraints, a number of models have been developed to predict PAM actuation behavior, with most models focusing on either energy balance or force balance methods of derivation [1-2,10,17-22]. These methods all agree upon the same initial forcing term, known as the Gaylord force,

$$F_G = \frac{P}{4N^2\pi}\left(3L^2 - B^2\right) \tag{4}$$

where F_G is the force generated by the PAM upon pressurization and P is the actuation pressure. While this model provides a reasonable estimate for blocked force, it fails to capture the nonlinearity of the actuation diagram and over-predicts the PAM performance. In order to better represent the behavior of the actuator, several correction terms have been added to the Gaylord force to account for factors such as elasticity in the braid and bladder, non-cylindrical tip shapes, and friction between the actuator components [2,4,18-23].

3.4.2. Force Balance Model

Of these various models, the force balance models proposed by previous researchers [21-22], then refined in Chapter 2, provided an excellent estimation of the output of the PAMs used in this study. In this prior work, the force produced by the actuator was predicted based on force balance methods and derived using the free-body diagram shown in Figure 3.4. From this diagram, the equilibrium equations in the *x*- and *z*-directions are, respectively,

$$PRL = \sigma_x tL + NT\cos\alpha \tag{5}$$

and

$$F + \pi R^2 P = \sigma_z A_B + T\sin\alpha \tag{6}$$

where R is the instantaneous bladder outer radius, σ is the stress in the bladder (in the *x*- or *z*-direction as noted by the subscript), t is the instantaneous thickness of the bladder, T is the tension in the braided sleeve fiber, F is the total longitudinal force exerted by the PAM, and A_B is the bladder cross-sectional area.

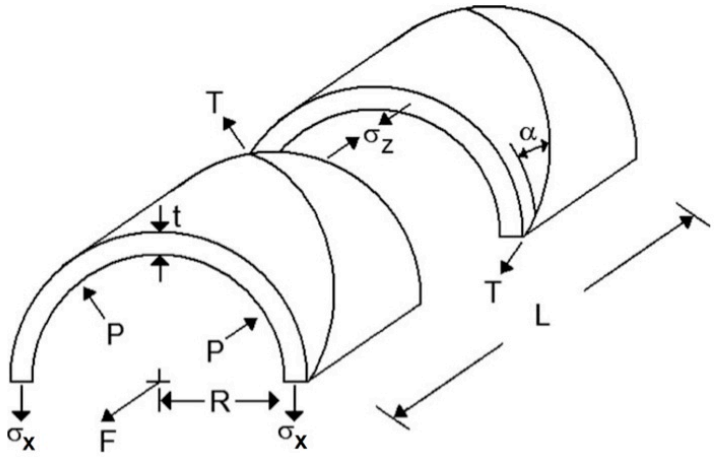

Figure 3.4 Free-body diagram used in the force balance model derivation [modified from Ref. 22].

Assuming a constant bladder volume (V_B), the bladder cross-sectional area can be written as $A_B = V_B/L$. Also, the instantaneous bladder thickness can be calculated as

$$t = R - \sqrt{R^2 - \frac{V_B}{\pi L}}. \tag{7}$$

Making use of trigonometric identities and the geometric constraints provided in Equations (2) and (3), the instantaneous bladder outer radius may be written as

$$R = \frac{\sqrt{B^2 - L^2}}{2\pi N}. \tag{8}$$

With this expression for R, as well as the geometric constraints, it is possible to solve Equations (5) and (6) for T, set them equal to each other, then group like terms such that the force generated by the PAM is given by

$$F = \frac{P}{4N^2\pi}\left(3L^2 - B^2\right) + \sigma_z \frac{V_B}{L} - \frac{\sigma_x t L^2}{2\pi N^2 R}. \tag{9}$$

Observe that the first term is now equivalent to the Gaylord force term (F_G) from Equation (4), and the remaining terms are corrections that account for elasticity in the bladder.

Moving forward, former derivations of this model used a linear elastic model for the bladder [21-22]. However, this material model fails to capture the nonlinear response of the actuator and does nothing to predict the softening in the bladder at high radial strains that was demonstrated during the experimental characterization of both the contractile PAM and the push-PAM. In order to account for this behavior, the nonlinear elastic model proposed in Chapter 2 was selected for use with the force balance derivation method. In this nonlinear material model, the stress in both the *x*- and *z*-directions is given by

$$\sigma = \sum_{k=1}^{M} E_k \varepsilon^k \tag{10}$$

where ε is the strain in the bladder and the modulus values (E_k) are design variables that are identified from empirical data at each operating pressure in order to minimize the error between the model and the experimental results. The summation upper limit (M) defines the order of the material model and is chosen by the researcher such that the model is robust enough to capture the full behavior of the actuator. The strains are defined as in the original force balance model developed by Ferraresi *et al.* [21] as

$$\varepsilon_x = \frac{\Delta R}{R_0} = \frac{R - R_0}{R_0} = \frac{R}{R_0} - 1 \tag{11}$$

and

$$\varepsilon_z = \frac{\Delta L}{L_0} = \frac{L - L_0}{L_0} = \frac{L}{L_0} - 1 \tag{12}$$

where ΔR is the change in bladder outer radius and R_0 is the initial bladder outer radius. Substituting this stress vs. strain constitutive material relationship into Equation (9), the force in the PAM is

$$F = \frac{P}{4N^2\pi}\left(3L^2 - B^2\right) + \frac{V_B}{L}\sum_{k=1}^{M} E_k \left(\frac{L}{L_0} - 1\right)^k - \frac{tL^2}{2\pi N^2 R}\sum_{k=1}^{M} E_k \left(\frac{R}{R_0} - 1\right)^k . \tag{13}$$

As previously mentioned, the first term in this model is the basic Gaylord force term (F_G), while the second two terms are correction terms identified through the use of the nonlinear elastic model in conjunction with the force balance derivation. Labeling these additional two correction terms, collectively, as F_{NLFB}, the overall PAM force presented in Equation (13) can be written as $F = F_G + F_{NLFB}$.

As shown in Chapter 2, note that by setting $M = 1$ (i.e. using a linear elastic constitutive model) in Equation (13), this model simplifies to the force balance model derived in Refs. [21-22]:

$$F = \frac{P}{4N^2\pi}\left(3L^2 - B^2\right) + E_1 V_B\left(\frac{1}{L_0} - \frac{1}{L}\right) - \frac{E_1 t L^2}{2\pi N^2}\left(\frac{1}{R_0} - \frac{1}{R}\right) \tag{14}$$

where E_1 is simply the elastic modulus of the latex bladder, assumed constant over all operating pressures. In this case, the two additional force correction terms added to the Gaylord force are collectively referred to as F_{LFB} such that the overall PAM force in Equation (14) is given by $F = F_G + F_{LFB}$. As demonstrated in Chapter 2, and further validated by the current study in *Section 3.4.5*, however, prudent selection of $M > 1$ in Equation (13) allows for a much more accurate prediction of PAM behavior through the use of the nonlinear elastic material model.

3.4.3. Friction Force Model

In order to fully capture the nonlinear actuation behavior of both types of PAMs, an additional force correction term is required to account for the friction between PAM components such that the hysteresis loop demonstrated in the experimental characterization can be accurately modeled. Previous researchers have investigated several methods to account for this behavior, including the use of a fixed friction force [2], a friction force calculated from a static friction model for interactions between the braid fibers at a micromechanical level [18-19,23], and a friction force directly proportional to the PAM force [4]. A more comprehensive review of friction and hysteresis modeling within PAM research is offered in Ref. [28].

Given the simplicity and accuracy of the friction model suggested by Woods *et al.* [4], a similar term has been proposed for use with the nonlinear elastic force balance model, as was used in Chapter 2 for the miniature PAMs. For this correction term, the friction force (F_F) opposes the PAM motion such that the friction reduces the overall PAM force during contraction (when the actuator is considered to be moving with positive velocity, v) and increases overall PAM force during extension (when velocity is considered negative). In this model, the magnitude of the friction force is proportional to the magnitude of the PAM force, and is thus calculated as

$$F_F = -k_F \left(F_G + F_{NLFB} \right) \mathrm{sgn}\left(v \right) \tag{15}$$

where k_F is an empirically fit friction factor. For the PAMs used in this study, k_F decreased linearly with actuation pressure. For the contractile PAM, k_F ranged from 0.14 at 207 kPa down to 0.06 at 621 kPa. For the push-PAM, however, more hysteresis was demonstrated in the actuation diagram (most likely due to additional friction in the rod seal), so the friction factor was slightly higher, ranging from 0.16 at 207 kPa to 0.08 at 621 kPa. Combining the friction force from Equation (15) with the nonlinear elastic force balance model given in Equation (13), the full PAM actuation force is now given by $F = F_G + F_{NLFB} + F_F$.

3.4.4. Pressure Deadband

Similar to PAM characteristics reported by previous researchers [2,10,20,24] and in Chapter 2, the actuators used in this study required a small amount of initial pressurization for the bladder to make substantial contact with the surrounding braid and initiate inflation of the PAM, resulting in an actuation deadband at low operating pressures. To capture this physical phenomenon and its effects on the PAM force

generated at a given actuation pressure, a pressure offset term was included in the analysis to account for the initial pressure required for the PAM to begin to actuate. In order to model the pressure deadband, the actuation pressure P is reduced as

$$P' = P - P_c \tag{16}$$

where P' is the corrected actuation pressure to be used in place of P in the PAM force model, and P_c is an empirically obtained term corresponding to the pressure at which the PAM initiates contraction. To validate the presence of this deadband and identify the correct value for P_c, the pressure-averaged blocked force (i.e. the maximum force exerted by the PAM, neglecting hysteresis effects, at each actuation pressure) is shown plotted against actuation pressure in Figure 3.5 for both types of actuators for the entire range of pressures tested. As is evident from the figure, there is a strong linear correlation between blocked force and actuation pressure. With the visual aid of the linear trend lines that have been plotted with the data, it is also clear that neither PAM is likely to generate a blocked force until a minimum actuation pressure threshold has been reached, demonstrating the existence of the deadband [29]. This minimum pressure is given by the x-intercept of the linear trend line for each data set and is used as the pressure offset, P_c. For the contractile PAM and push-PAM used in this study, P_c was determined from the linear trend lines to be 46.4 kPa (6.7 psi) and 58.1 kPa (8.4 psi), respectively.

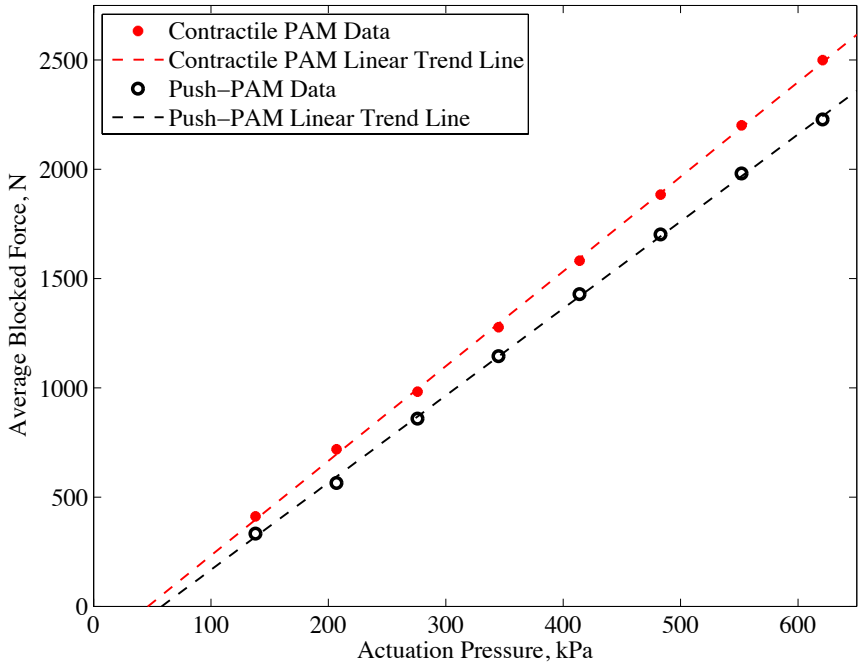

Figure 3.5 Blocked force as a function of actuation pressure with linear trend lines to demonstrate the presence of a pressure deadband.

Incorporating this model improvement such that the previously described forcing terms in Equations (13) and (15) are a function of the corrected pressure where applicable, the full PAM force model is given by

$$F = F_G\left(P = P'\right) + F_{NLFB} + F_F\left(P = P'\right). \tag{17}$$

Unless explicitly stated otherwise, the model results presented in the following section are a function of the corrected pressure (P') in place of the measured value (P) where it appears in the original model expressions previously described in Equations (13) and (15).

3.4.5. Discussion of Modeling Results

As mentioned in *Section 3.4.2*, the proposed force balance model uses the nonlinear material elastic model given in Equation (10) with empirically identified

modulus values (E_k). In order to achieve accurate results, the built-in MATLAB function *fmincon* (see Appendix A) was used to determine the optimum values of E_k at each operating pressure such that the error between the model output without friction force ($F_G + F_{NLFB}$) and the average force within the hysteresis loop (F_{AVG} as depicted in Figure 3.3(b)) was a minimum. This process was carried out for increasing summation upper limits (M) until the model was able to accurately capture the PAM behavior for all operating pressures, neglecting hysteresis effects. In this optimization, the objective function that was minimized by the MATLAB solver is a normalized least squares regression error given by

$$Error = \sum_i \left(\frac{\left(F_G + F_{NLFB}\right)_i - \left(F_{AVG}\right)_i}{\left(F_{AVG}\right)_i} \right)^2 \tag{18}$$

where $(F_G + F_{NLFB})_i$ is the ith data point predicted by the model described in Equation (13), and $(F_{AVG})_i$ is the ith data point given by the average between the upper and lower hysteresis curves within the actual experimental data set (see Figure 3.3(b)).

The results of the proposed nonlinear elastic force balance model are shown with respect to F_{AVG} in Figure 3.6 for the 207, 414, and 621 kPa tests, demonstrating the impact of increasing the summation upper limit (M) on the accuracy of the model for both the contractile PAM (top row) and the push-PAM (bottom row). Figure 3.6(a) and Figure 3.6(d) also show the results of the non-optimized linear force balance model (proposed by previous researchers and presented again in Equation (14))[21-22]. From Figure 3.6(a) and Figure 3.6(d), it is apparent that a linear elastic material model ($M = 1$) is unable to capture the response of either type of PAM. Using the non-optimized linear force balance model (in which E_1 is constant across all pressures), the model accurately

predicts blocked force, but greatly over-predicts the PAM force capabilities throughout actuation, with increased error at higher actuation pressures. While the optimized linear elastic model (in which E_1 is pressure-dependent and has been optimized over the linear elastic portion of PAM contraction from $0 < \Delta L/L_0 < 0.05$) yields much more accurate results, the model tends to under-predict PAM performance at high contractions and high pressures, especially for the contractile PAM, which has slightly better free contraction characteristics. Given the errors associated with the linear elastic model, the accuracy of using a quadratic elastic model ($M = 2$) was next evaluated, with the output of the model shown with respect to F_{AVG} in Figure 3.6(b) and Figure 3.6(e). In these figures, the results of E_k optimized over both the linear elastic portion of PAM contraction ($0 < \Delta L/L_0 < 0.05$) and over the entire contractile range are shown. For both optimization ranges, it is evident that the quadratic elastic model still lacks the robustness required to capture the PAM behavior throughout actuation. For both PAMs, the quadratic elastic model causes the force balance model to slightly under-predict the force at low contractions and over-predict the force at high contractions. Continuing in this manner, the order of the material model from Equation (10) was increased to $M = 3$ (results not shown) and ultimately to $M = 4$, with the output from the quartic elastic model ($M = 4$) finally producing satisfactorily accurate correlation between the model and the pressure-averaged experimental data for the full actuation range of both the contractile PAM and push-PAM, as shown in Figure 3.6(c) and Figure 3.6(f). Not only does this result demonstrate the excellent modeling capabilities of the nonlinear elastic force balance analysis, but it also confirms that the modeling approaches used to predict traditional PAM behavior may be applied to the push-PAM apparatus with comparable accuracy.

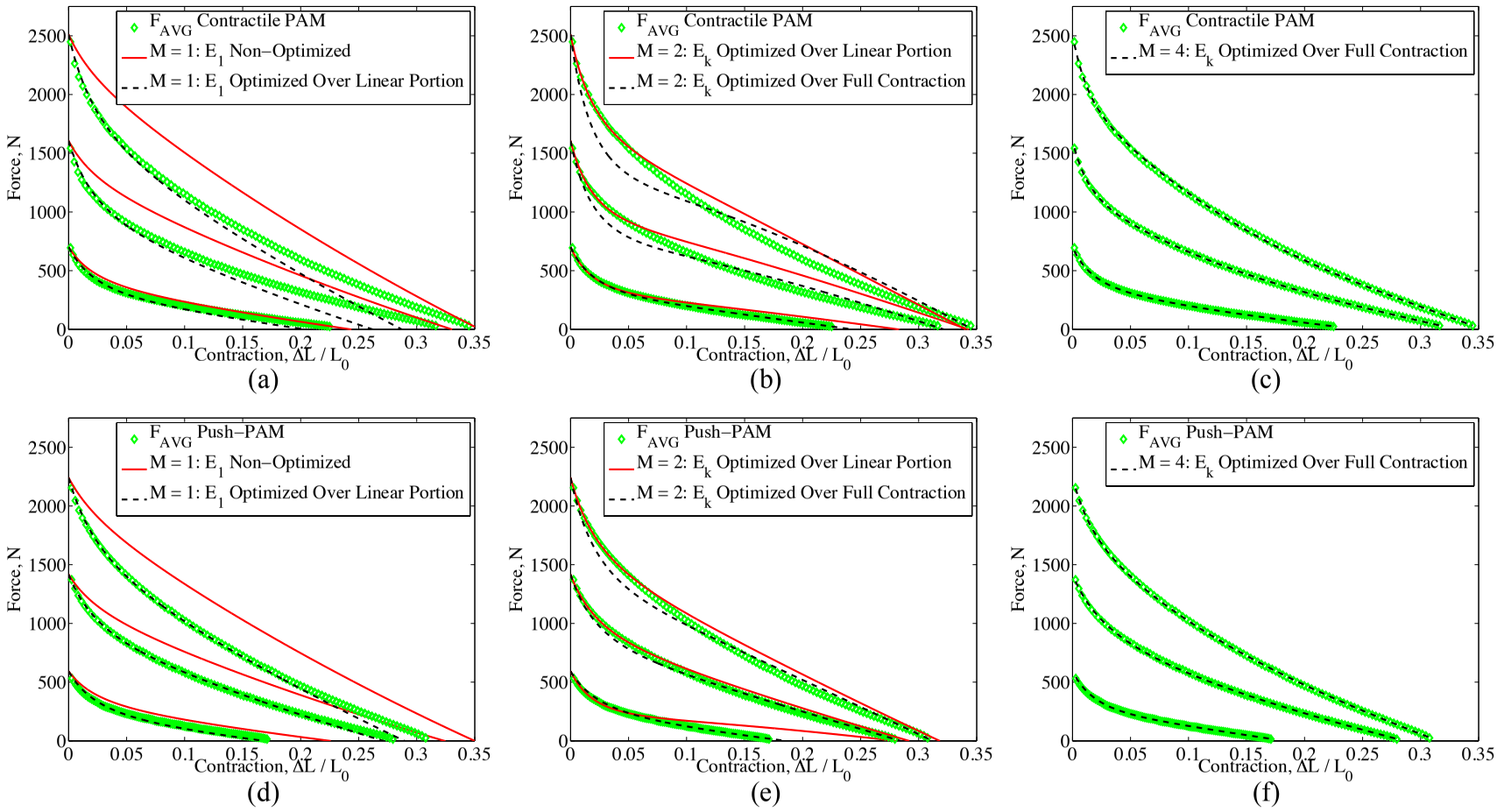

Figure 3.6 Force balance model results compared with averaged experimental data for the contractile PAM (a – c) and the push-PAM (d – f). (a/d) Linear elastic model results (M = 1) for E_1 non-optimized and E_1 optimized over the linear elastic portion of PAM contraction. (b/e) Quadratic elastic model results (M = 2) for E_k optimized over the linear elastic portion of PAM contraction and E_k optimized over the full PAM contractile range. (c/f) Quartic elastic model results (M = 4) for E_k optimized over the full PAM contractile range.

As a complement to the results shown in Figure 3.6, it is also interesting to consider the physical nature of the material models proposed through both the non-optimized linear elastic model and the optimized elastic models for the contractile PAM and the push-PAM. To that end, Figure 3.7 shows the bladder stress-strain curves associated with the linear elastic material models (M = 1, both non-optimized and optimized) and the quartic material model (M = 4) that was ultimately shown to deliver accurate force predictions. For clarity, only the models for the tests at an actuation pressure of 414 kPa are shown in the figure. Here, the stress-strain relationship has been calculated as in Equation (10) using the corresponding values of E_k for each model. This relationship has been calculated up to a maximum strain of 1.6739, which corresponds to the highest radial strain experienced during testing at this pressure as defined in Equation (11) and calculated using instantaneous bladder radius values given in Equation (8). As implied by a linear elastic model, the results for M = 1 with both non-optimized E_1 and optimized E_1 suggest that stress in the bladder varies linearly with strain over the full range of motion of the PAM, which, based on actual PAM behavior and the nature of elastomeric materials, is physically unlikely. Using the results of the optimization with the quartic elastic model (E_k with M = 4), however, the stress-strain curve indicates that the PAM bladders soften with increased strain, which is physically justifiable and yields excellent correlation with PAM actuation behavior. Furthermore, these results indicate that the contractile PAM bladder undergoes more softening than that of the push-PAM, which was suspected based on the nature of the actuator load lines. Regarding the model associated with the contractile PAM, however, it is clear that such a stress-strain curve yields impractical results at high strains, so additional research into hyper-elastic material

models may be required to fully characterize the nonlinear elastic nature of these PAM bladders.

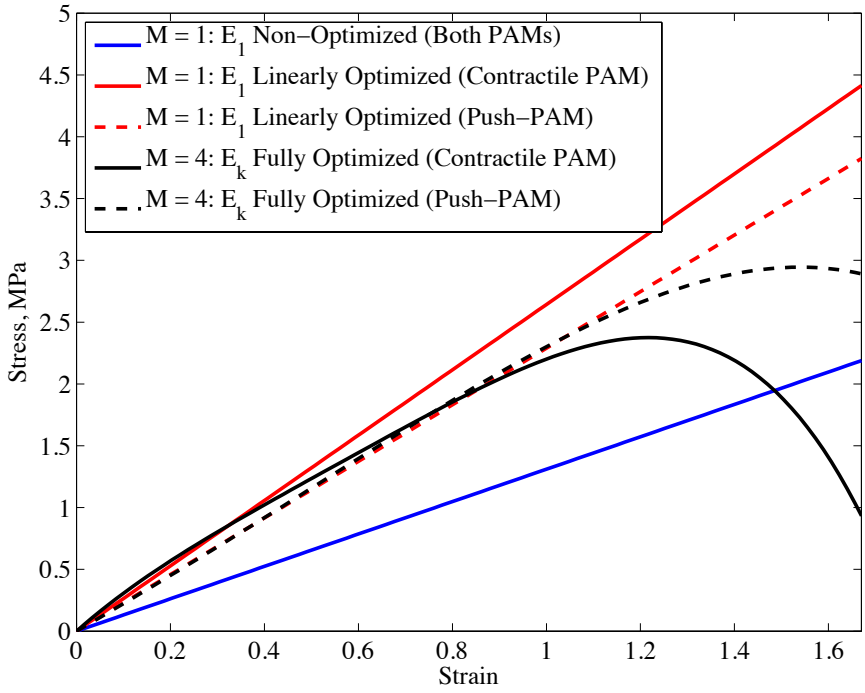

Figure 3.7 Stress-strain curves associated with a non-optimized linear elastic model and optimized elastic models for $M = 1$ and $M = 4$ for both the contractile PAM and the push-PAM.

As previously mentioned, two main parameters of interest are the blocked force and free contraction of the PAMs at each internal pressure. These values are represented in Figure 3.3 and Figure 3.6 as the points at which the actuator load lines reach each axis (blocked force on the vertical axis and free contraction on the horizontal axis). It is evident in these figures that both blocked force and free contraction increase with pressure. For clarity, however, the strict evolution of each parameter with internal pressure is shown separately in Figure 3.8 for the entire range of actuation pressures tested. Also included in Figure 3.8 are the model predictions for these parameters using

the nonlinear elastic force balance model with $M = 4$. Regarding the experimental data alone, it is clear that the contractile PAM is able to achieve a slightly higher blocked force and free contraction than the push-PAM at each actuation pressure. However, it important to acknowledge that the push-PAM yields comparable results, and some of this disparity is due to manufacturing differences between the contractile PAM and the push-PAM (e.g. active length, braid angle, pressure offset). Studying the model predictions for blocked force and free contraction, the overwhelming accuracy of the nonlinear elastic force balance model (with a pressure deadband correction term) is once again confirmed. Additionally, the hypothesis that the contractile PAM and the push-PAM can be effectively modeled with the same set of equations is further validated.

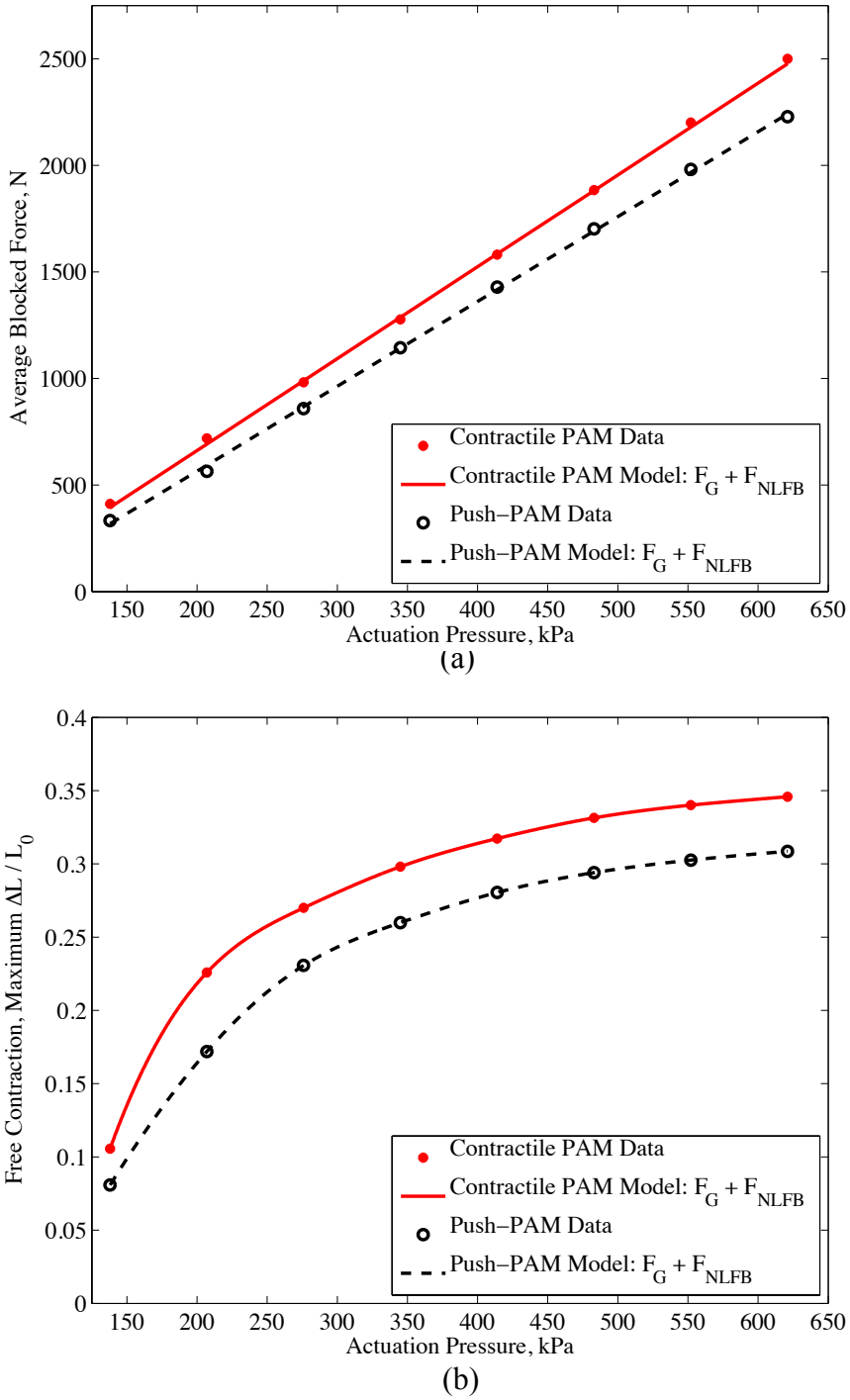

Figure 3.8 Experimental results and nonlinear elastic force balance model predictions for (a) blocked force and (b) free contraction as a function of pressure.

To further demonstrate the accuracy of the nonlinear elastic force balance model with $M = 4$, the results of this model ($F_G + F_{NLFB}$) with E_k empirically optimized for each actuation pressure are shown with respect to the to the full experimental results for the 207, 414, and 621 kPa tests in Figure 3.9. For clarity, the results from the contractile PAM and the push-PAM have been plotted in two separate figures (Figure 3.9(a) and Figure 3.9(b), respectively). It is evident from these figures that the PAM behavior predicted by the nonlinear elastic force balance model given by Equation (13) yields excellent agreement with the experimental data (neglecting hysteresis), including the rapidly changing stiffness of the PAMs below $\Delta L/L_0 = 0.05$. As such, these results help to pave the way forward for both the traditional contractile PAM and the novel push-PAM to be better utilized in controlled actuation schemes.

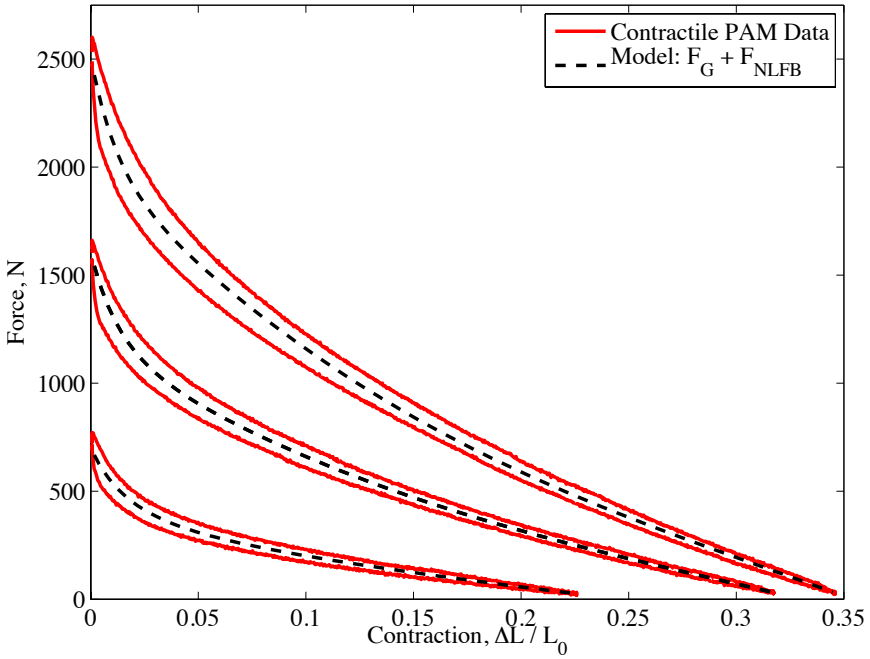

(a)

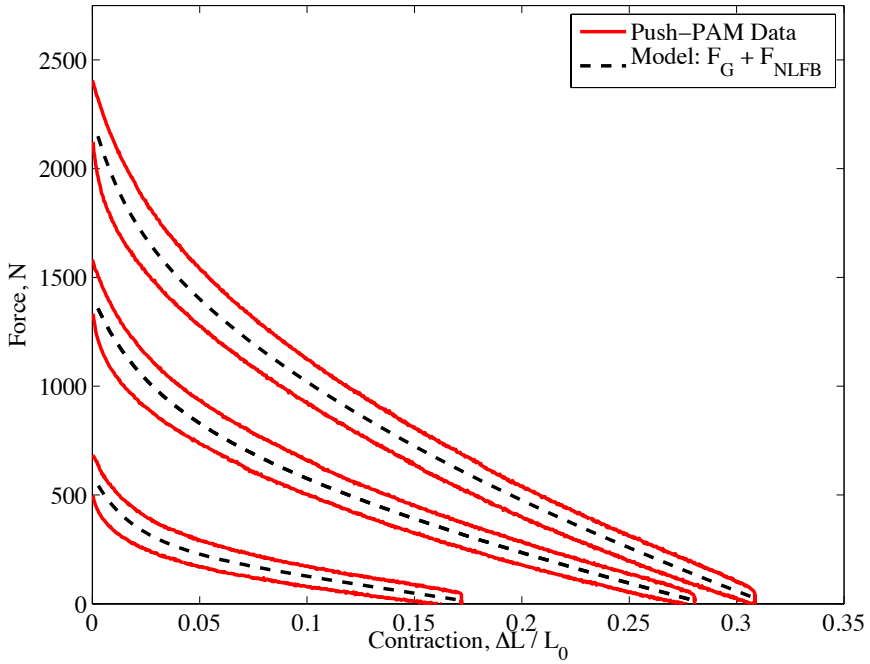

(b)

Figure 3.9 Results of the nonlinear elastic force balance model (using M = 4) compared to full experimental results for (a) the contractile PAM and (b) the push-PAM.

Although the nonlinear elastic force balance model was originally developed in Chapter 2 to accurately capture the actuation characteristics of small-scale PAMs (with diameters on the order of millimeters), these results show that this model is appropriate and useful for larger full-scale PAMs as well. To validate the impact of the nonlinear elastic force balance model on the accuracy of full-scale PAM force predictions, Figure 3.10 shows the progression in model capabilities from the basic Gaylord force model to the nonlinear elastic force balance model with a pressure offset term (using only the 414 kPa case for the sake of clarity). While Figure 3.10(a) and Figure 3.10(c) show the actual model output compared to the experimental results for the contractile PAM and the push-PAM (respectively), Figure 3.10(b) and Figure 3.10(d) show the associated error between the model prediction (F_{MODEL}) and the experimental data for each type of PAM (contractile PAM results in the top row, push-PAM results in the bottom row). As the models shown here neglected hysteresis, the experimental data used to calculate the error is the average force (F_{AVG}) as used above. The error at each contraction value has been calculated as

$$Error_i = \left| \frac{\left(F_{MODEL}\right)_i - \left(F_{AVG}\right)_i}{F_B} \right| \tag{19}$$

where F_B is the pressure-averaged blocked force for each type of actuator.

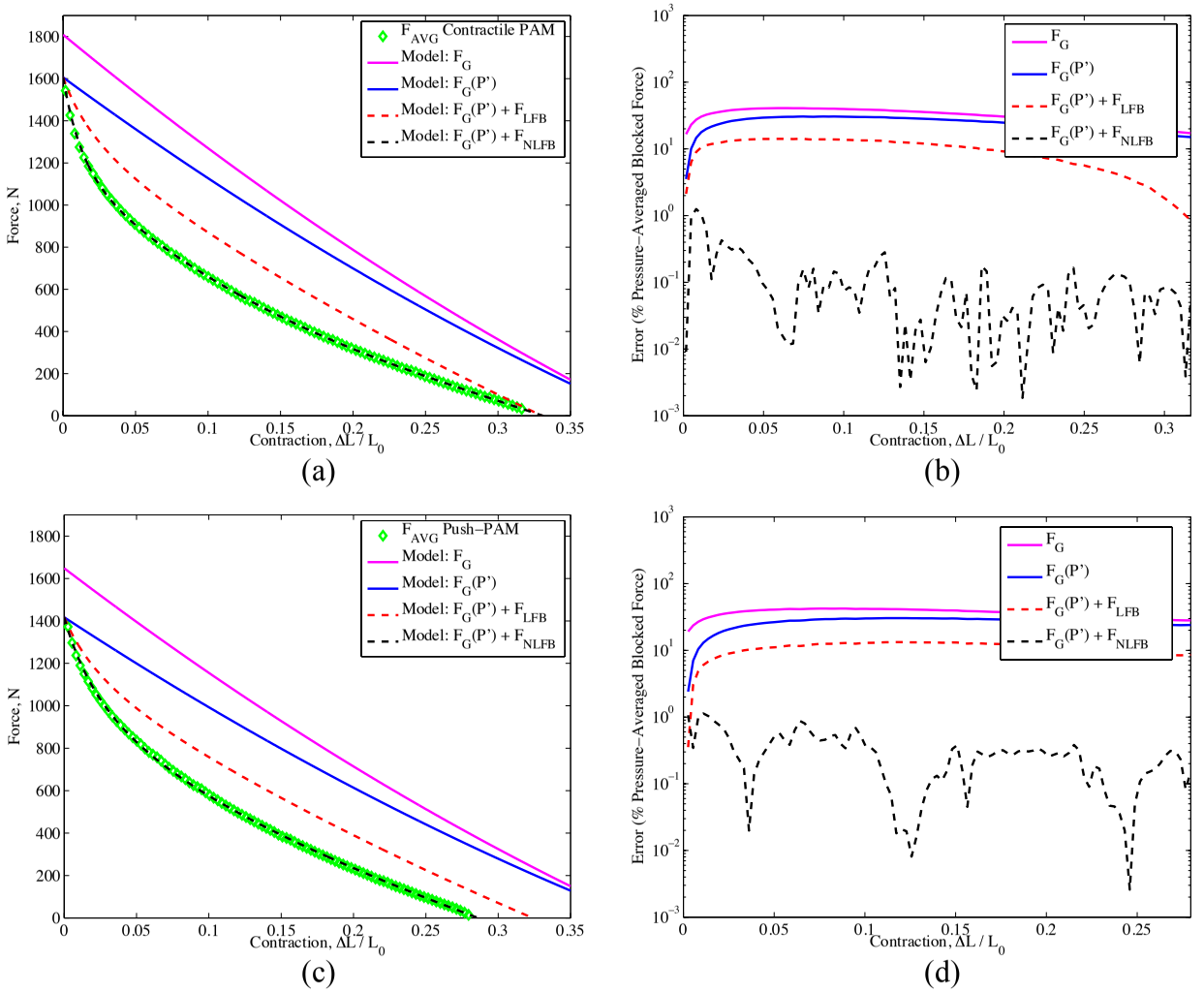

Figure 3.10 Progressive accuracy of modeling techniques for the contractile PAM (a – b) and the push-PAM (c – d) at 414 kPa. (a/c) Model output compared to experimental data. (b/d) Associated model error (% of pressure-averaged block force).

As is evident in Figure 3.10, the Gaylord force by itself (F_G) provides a poor estimate of each PAM's blocked force capabilities and uniformly over-predicts the PAM performance as the actuators contract. Upon including the pressure correction to account for the actuation deadband (see $F_G(P')$), the model yields a much more accurate prediction of blocked force, but still fails to capture the appropriate loss in PAM force with increasing contraction. Using the basic linear elastic force balance model used by Ferraresi *et al.* [21] and again by Kothera *et al.* [22], that is $F_G(P') + F_{LFB}$, the model is able to more closely forecast the PAM force, although it still tends to over-predict the PAM output throughout actuation for both the contractile PAM and the push-PAM. Finally, the nonlinear elastic force balance model proposed in this thesis, $F_G(P') + F_{NLFB}$, shown here using $M = 4$, is able to fully capture the PAM actuation behavior and predict the PAM force (neglecting hysteresis) with considerably less error, demonstrating that this model does indeed work well with full-scale PAMs, in addition to the small-scale PAMs for which it was developed. This comparison also corroborates the assertion that the same type of modeling efforts may be used on both the contractile PAM and the push-PAM with comparable accuracy. For the contractile PAM results shown in Figure 3.10(a) and Figure 3.10(b), the nonlinear elastic force balance model yielded an average error of only 0.12% and a maximum error of 1.26% with respect to the contractile PAM's blocked force at 414 kPa. Similarly, the push-PAM results from Figure 3.10(c) and Figure 3.10(d) reflect an average error of only 0.31% and a maximum error of 1.13% with respect to that PAM's blocked force using the same model. Across all of the actuation pressures tested (not shown graphically), the average error associated with the

nonlinear elastic force balance model was 0.22% for the contractile PAM and 0.34% for the push-PAM, confirming the similar accuracy of the model for both types of actuators.

Having verified the ability of the nonlinear elastic force balance model to predict the average force output of both the contractile PAM and the push-PAM, the next phase of the model validation process was to incorporate the friction force term as proposed in Equation (15) in order to fully capture the hysteretic nature of the PAM actuation. The output of the full PAM force model ($F_G + F_{NLFB} + F_F$) is shown with respect to the experimental data in Figure 3.11, with the results from the contractile PAM shown in Figure 3.11(a) and those of the push-PAM shown in Figure 3.11(b). Here it is evident that the proposed model accurately predicts the PAM force as a function of actuation pressure, PAM contraction, and PAM direction of motion, fully encompassing all aspects of the actuation behavior for both types of actuators.

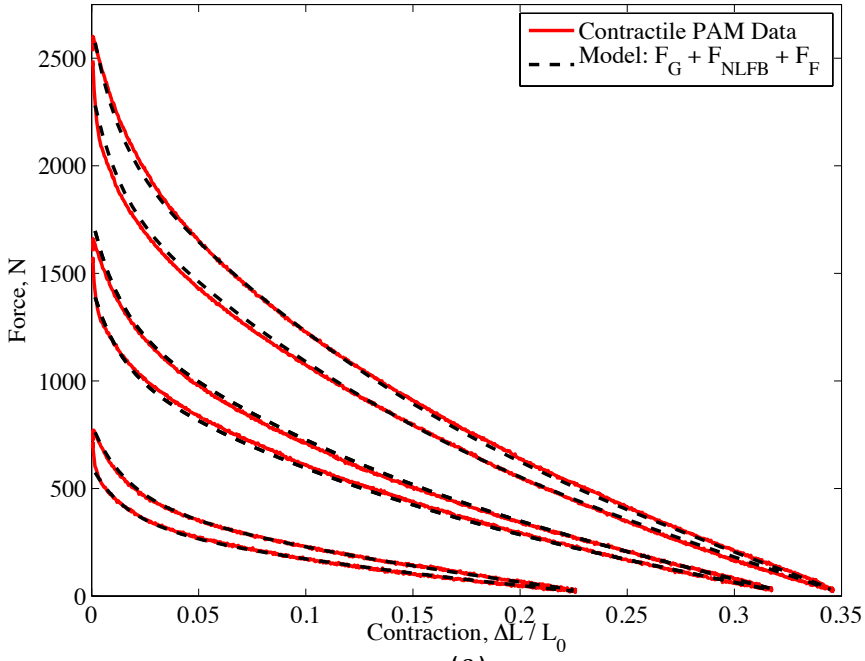

(a)

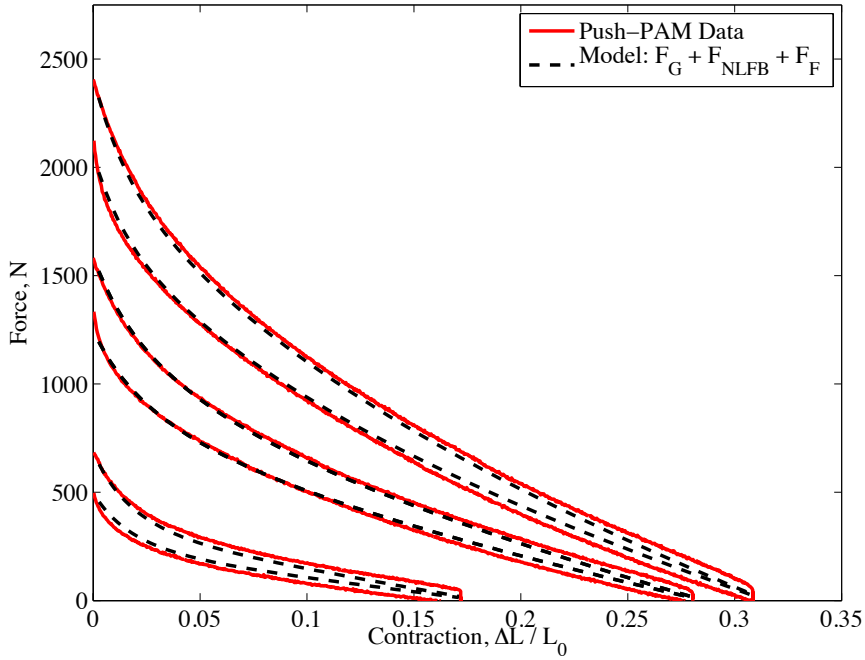

(b)

Figure 3.11 Full PAM force model ($F_G + F_{NLFB} + F_F$) compared to experimental data for (a) the contractile PAM and (b) the push-PAM.

3.4.6. Impact of Length Correction Term on Modeling Efforts

Although prior work on PAMs supports the inclusion of a length correction term to account for the non-cylindrical tip shape of the actuator when it is inflated [4,10,19-20,22], it was ultimately concluded that the inclusion of such a term generally weakened the results of the nonlinear elastic force balance model and diminished the physical significance of the proposed material model for the full-scale PAMs investigated here. Figure 3.12 shows the modeling results for both the contractile PAM (Figure 3.12(a)) and the push-PAM (Figure 3.12(b)) using the linear elastic force balance model (E_1 non-optimized) and the nonlinear elastic force balance model ($M = 4$), both with and without a corrected length term. While Tondu [28] offers a review of several methods used to account for the non-cylindrical tip shape, the correction offered by Woods *et al.* [4] was used to generate these results. For this correction, the tip shape was modeled as a 90° circular arc, which effectively reduced the length of the actuator at each end by

$$\Delta l = \left(\frac{\pi}{2} - 1\right)\left(R - R_0\right) \tag{20}$$

such that the corrected length was given by

$$L' = L - 2\Delta l \tag{21}$$

where L' was the corrected actuator length that was used in place of the true actuator length (L) in the PAM force models.

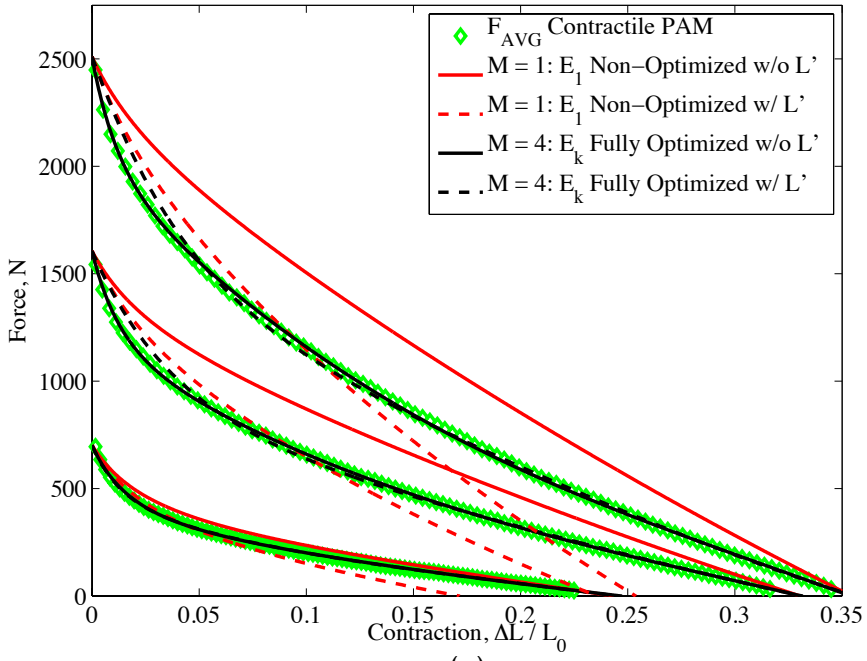

(a)

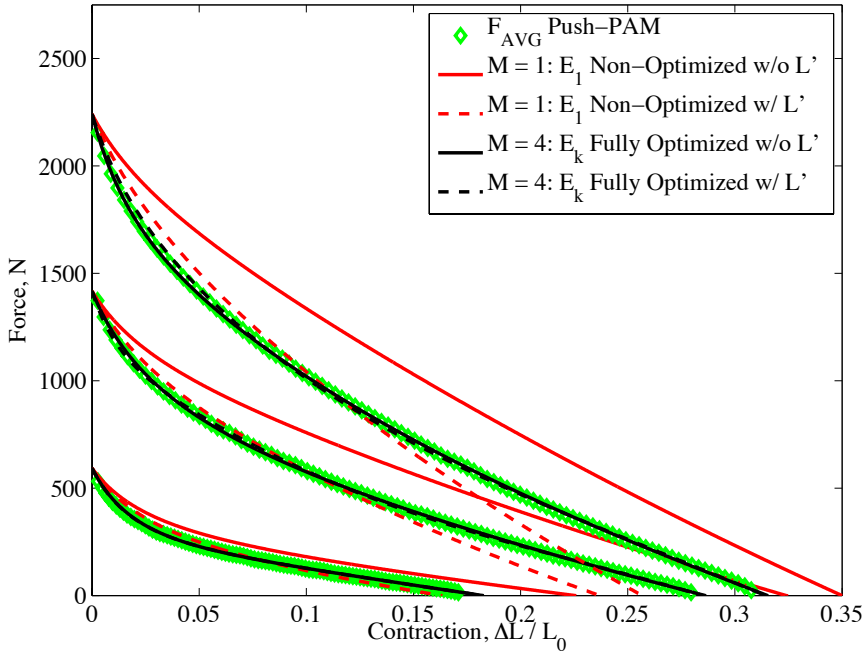

(b)

Figure 3.12 Force balance model results both with and without the corrected length term (*L'*) compared to experimental data for (a) the contractile PAM and (b) the push-PAM.

As shown in Figure 3.12, the inclusion of the length correction term reduces the predicted PAM force for the linear elastic force balance model ($M = 1$). This change allows the model to better capture the PAM actuation behavior at low contractions, but ultimately causes the model to vastly under-predict the PAM force at higher contractions. Including the length correction term with the nonlinear elastic force balance model ($M = 4$) produced a less substantial change with respect to the same model without the length correction term because the modulus values have been optimized for both types of models. In some cases (contractile PAM at 207 kPa, and push-PAM at 207 and 414 kPa), the two nonlinear models nearly overlay each other. However, it should be noted that at low contractions and high actuation pressures (especially for the contractile PAM), a higher order elastic model ($M > 4$) will be required when using L' in order to reproduce the same accuracy as was achieved without the use of L'.

Furthermore, the associated stress-strain curves that were generated for the optimized quartic elastic model with the inclusion of L' were investigated for comparison to those previously described in Figure 3.7 for the same order model without L'. A direct comparison between the two material models is shown in Figure 3.13 for the 414 kPa test of both the contractile PAM and the push-PAM, with the maximum strain plotted once again corresponding to the maximum radial strain encountered during testing. As shown in this figure, the stress-strain relationship associated with the nonlinear elastic model using L' is physically impossible, suggesting that the stress in the bladder is negative as a result of the strains encountered during testing. So although the use of the length correction term had a small effect on the accuracy of the nonlinear elastic force balance model in terms of predicting the PAM actuation diagram, the loss of physical significance

associated with including this correction make it inappropriate to use *L'* with the PAMs studied here.

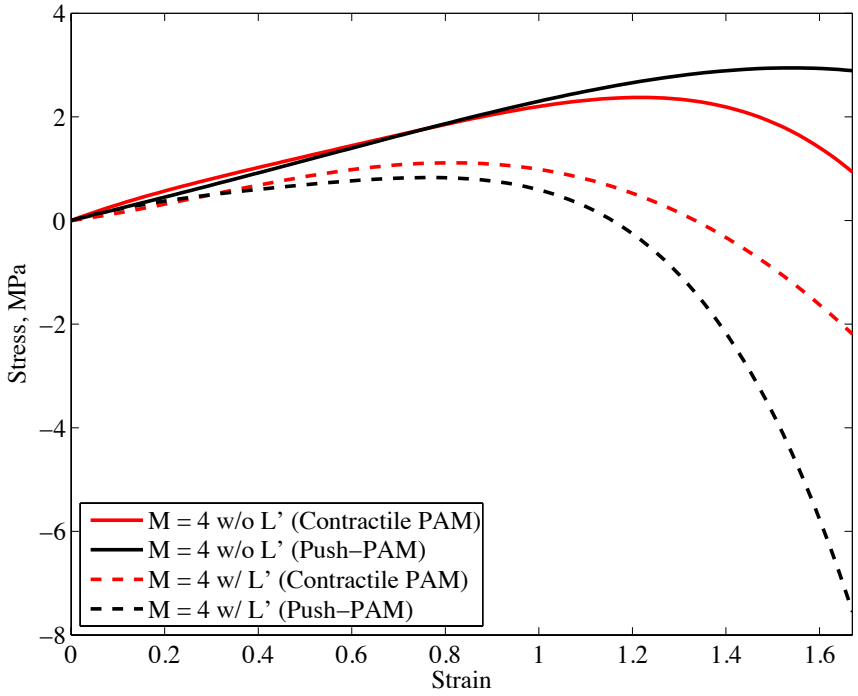

Figure 3.13 Stress-strain curves associated with an optimized nonlinear elastic model (*M* = 4), with and without *L'* , for the contractile PAM and the push-PAM.

3.5. Conclusions

This study proposed a novel pneumatic artificial muscle (PAM) actuator that utilized the advantageous performance characteristics of a traditional contractile PAM, but converted the normal direction of force and motion such that the resulting push-PAM achieved excellent compressive force generation and extensile motion with just a small increase in friction, weight, and cost. This motion conversion was accomplished by a pushrod that was attached to the inside of one of the contractile PAM's end fittings and extended through the actuator body and out of the other end fitting. Upon pressurization, the flexible body of the actuator inflated and expanded radially, causing relative

contractile motion between the two end fittings, which ultimately extended the pushrod such that the push-PAM actuator demonstrated extensile motion and compressive force generation. The key results of this study are the following:

1. The experimental characterization of the push-PAM highlighted the quasi-static behavior of the actuator and verified that the push-PAM was capable of producing forces and displacements comparable to a contractile PAM. For both types of actuators, three key nonlinear phenomena were observed during testing: nonlinear PAM stiffness, hysteresis of the force vs. displacement response, and a pressure deadband.
2. In terms of modeling the behavior of the push-PAM, it was shown that the same analysis methods may be applied to both the push-PAM and the contractile PAM with similar accuracy. In order to account for the nonlinear behavior of the actuators, both PAMs were ultimately modeled using a refined force balance model. This model included correction terms to accurately capture the nonlinear stress vs. strain relationship in the PAM bladder, friction effects that contributed to hysteresis, as well as the actuation deadband at low operating pressures, offering excellent agreement with experimental results for both the contractile PAM and the push-PAM. Additionally, the accuracy of these modeling efforts validated the applicability of the nonlinear elastic force balance model proposed in Chapter 2 for use with full-scale PAM actuators.

3. Further model analysis revealed that the inclusion of a length correction term to account for the non-cylindrical tip shape of the PAM generally weakened the results of the nonlinear elastic force balance model and diminished the physical significance of the proposed material model for the full-scale PAMs investigated here.

In conclusion, the push-PAM offers a simple, yet highly effective device for utilizing the outstanding actuation characteristics of a contractile PAM in a manner the yields extensile motion and compressive force generation. Having proven that this push-PAM is capable of achieving forces and displacements that are comparable to those of its contractile counterpart, while also adhering to the same modeling approaches, this apparatus stands to revolutionize the application of PAM actuators by opening the doors to a wide array of tasks that were previously unsuitable for the contractile motion and tensile forces of traditional contractile PAMs.

3.6. References

[1] Caldwell, D., Tsagarakis, N., and Medrano-Cerda, G. A., 2000, "Bio-mimetic Actuators: Polymeric Pseudo Muscular Actuators and Pneumatic Muscle Actuators for Biological Emulation," Mechatronics, **10**(4–5), pp. 499–530. DOI: 10.1016/S0957-4158(99)00071-9

[2] Chou, C., and Hannaford, B., 1994, "Static and Dynamic Characteristics of McKibben Pneumatic Artificial Muscles," *Proc. of ICRA*, **1**, pp. 281–286.

[3] Woods, B. K. S., 2012, "Pneumatic Artificial Muscle Driven Trailing Edge Flaps for Active Rotors," Ph.D. Thesis, University of Maryland, College Park.

[4] Woods, B. K. S., Kothera, C. S., and Wereley, N. M., 2011, "Wind Tunnel Testing of a Helicopter Rotor Trailing Edge Flap Actuated via Pneumatic Artificial Muscles," J. Intell. Mater. Syst. Struct., **22**(13), pp. 1513–1528. DOI: 10.1177/1045389X11424216

[5] Vocke III, R. D., Kothera, C. S., Chaudhuri, A., Woods, B. K. S., and Wereley, N. M., 2012, "Design and Testing of a High-specific Work Actuator Using Miniature Pneumatic Artificial Muscles," J. Intell. Mater. Syst. Struct., **23**(3), pp. 365–378. DOI: 10.1177/1045389X11431743

[6] Woods, B. K. S., Gentry, M. F., Kothera, C. S., and Wereley, N. M., 2011, "Fatigue Life Testing of Swaged Pneumatic Artificial Muscles as Actuators for Aerospace Applications," J. Intell. Mater. Syst. Struct., **23**(3), pp. 327–343. DOI: 10.1177/1045389X11433495

[7] Philen, M. K., 2009, "On the Applicability of Fluidic Flexible Matrix Composite Variable Impedance Materials for Prosthetic and Orthotic Devices," Smart Mater. Struct., **18,** 104023 (10pp). DOI: 10.1088/0964-1726/18/10/104023

[8] Bharadwaj, K., Hollander, K. W., Mathis, C. A., and Sugar, T. G., 2004, "Spring Over Muscle (SOM) Actuator for Rehabilitation Devices," *Proc. Of the 26th Annual Int. Conf. of the IEEE EMBS*, **1**, pp. 2726–2729.

[9] Birch, M. C., *et al.*, 2001, "A Miniature Hybrid Robot Propelled by Legs," *Proc. of the 2001 IELE/RSJ Int. Conf. on Intelligent Robots and Systems,* **2**, pp. 845–851.

[10] De Volder, M., Moers, A. J. M., and Reynaerts, D., 2011, "Fabrication and Control of Miniature McKibben Actuators," Sensors Actuat. A, **166**(1), pp. 111–116. DOI: 10.1016/j.sna.2011.01.002

[11] Chen, Y., Yin, W., Liu, Y., and Leng, J., 2011, "Structural Design and Analysis of Morphing Skin Embedded with Pneumatic Muscle Fibers," Smart Mater. Struct., **20,** 085033 (8pp). DOI: 10.1088/0964-1726/20/8/085033

[12] Bubert, E. A., 2009, "Highly Extensible Skin for a Variable Wing-Span Morphing Aircraft Utilizing Pneumatic Artificial Muscle Actuation," M.S. Thesis, University of Maryland, College Park.

[13] Zhang, Z., and Philen, M. K., 2011, "Review: Pressurized Artificial Muscles," J. Intell. Mater. Syst. Struct., **23**(3), pp. 255–268. DOI: 10.1177/1045389X11420592

[14] Pritts, M. B., and Rahn, C. D., 2004, "Design of an Artificial Muscle Continuum Robot," *Proc. IEEE Int. Conf. on Robotics and Automation*, **5**, pp. 4742–4746.

[15] Trivedi, D., and Rahn, C. D., 2012, "Soft Robotic Manipulators: Design, Analysis, and Control," *Plants and Mechanical Motion: A Synthetic Approach to Nastic Materials and Structures*, Wereley, N. M., and Sater, J. M., eds., DEStech Publications, Inc., Lancaster, PA, Chap. 7, pp. 141–165.

[16] Liu, W., and Rahn, C. D., 2003, "Fiber-Reinforced Membrane Models of McKibben Actuators," ASME J. Appl. Mech., **70**(6), pp. 853–859. DOI: 10.1115/1.1630812

[17] Gaylord, R., 1958, "Fluid Actuated Motor System and Stroking Device," U.S. Patent No. 2,844,126.

[18] Schulte, H. F., Adamski, D. F., and Pearson, J. R., 1961, "Characteristics of the Braided Fluid Actuator," Report at Department of Physical Medicine and Rehabilitation, the University of Michigan, Ann Arbor, MI, pp. 105–120.

[19] Tondu, B., and Lopez, P., 2000, "Modeling and Control of McKibben Artificial Muscle Robot Actuators," IEEE Control Systems Magazine, **20**(2), pp. 15–38. DOI: 10.1109/37.833638

[20] Tsagarakis, N., and Caldwell, D., 2000, "Improved Modeling and Assessment of Pneumatic Muscle Actuators," *Proc. of ICRA*, **4**, pp. 3641–3646.

[21] Ferraresi, C., Franco, W., and Bertetto, A. M., 2001, "Flexible Pneumatic Actuators: A Comparison Between the McKibben and the Straight Fibres Muscles," J. Robot. Mechatron., **13**(1), pp. 56–63.

[22] Kothera, C. S., Jangid, M., Sirohi, J., and Wereley, N. M., 2009, "Experimental Characterization and Static Modeling of McKibben Actuators," ASME J. Mech. Des., **131**, 091010 (10pp). DOI: 10.1115/1.3158982

[23] Davis, S., and Caldwell, D., 2006, "Braid Effects on Contractile Range and Friction Modeling in Pneumatic Muscle Actuators," Int. J. Robot. Res., **25**(4), pp. 359–369.

[24] Solano, B., and Rotinat-Libersa, C., 2011, "Compact and Lightweight Hydraulic Actuation System for High Performance Millimeter Scale Robotic Applications: Modeling and Experiments," J. Intell. Mater. Syst. Struct., **22**(13), pp. 1479–1487. DOI: 10.1177/1045389X11418860

[25] Zhu, B., Rahn, C. D., and Bakis, C. E., 2011, "Actuation of fluidic flexible matrix composites in structural media," J. Intell. Mater. Syst. Struct., **23**(3), pp. 269–278. DOI: 10.1177/1045389X11428676

[26] Philen, M. K., Shan, Y., Prakash, P., Wang, K. W., Rahn, C. D., Zydney, A. L., and Bakis, C. E., 2007, "Fibrillar Network Adaptive Structure with Ion-transport Actuation," J. Intell. Mater. Syst. Struct., **18**(4), pp. 323–334. DOI: 10.1177/1045389X06066097

[27] Woods, B. K. S., Wereley, N. M., Kothera, K. S., Boyer, S. M., 2011, "Extensile Fluidic Muscle Actuator," U.S Patent Appl. No. 12/955,242.

[28] Tondu, B., 2012, "Modelling of the McKibben Artificial Muscle: A Review," J. Intell. Mater. Syst. Struct., **23**(3), pp. 225–253. DOI: 10.1177/1045389X11435435

[29] Gelb, A., and Vander Velde, W. E., 1968, *Multiple-input Describing Functions and Nonlinear System Design*, McGraw-Hill, New York, pp. 4–5, Chap. 1.

4. Conclusions

In this thesis, the nonlinear quasi-static actuation behavior of two innovative pneumatic artificial muscles (PAMs) was carefully characterized and analyzed. The first of these actuators was a miniature PAM that possessed the same operating principle as a full-scale contractile PAM, but with a diameter an order of magnitude smaller. The second actuator, known as a push-PAM, harnessed the operational characteristics of a typical contractile PAM, but changed the direction of motion and force with a simple conversion package that required only a small increase in friction, weight, and cost.

For both the miniature PAM and the push-PAM, as well as a full-scale contractile PAM that was tested to serve as a baseline case, experimental characterization revealed three key nonlinear phenomena: nonlinear PAM stiffness, hysteresis in the force vs. displacement curve at a given pressure, and a pressure deadband. Despite the differences in size and construction of these PAMs, the nonlinear behavior of all three actuators was accurately modeled using a refined nonlinear force balance model that utilized correction terms to address each of the nonlinearities encountered during testing. The key results of the studies on each novel PAM are as follows.

4.1. Miniature PAM Development and Analysis

In this first study, miniature PAMs were constructed using low-cost commercially available materials in a manufacturing process that consistently yielded high-performance actuators that were suitable for use in small-scale mechanical systems. Experimental characterization revealed the highly nonlinear nature of the miniature PAM actuation, including nonlinear PAM stiffness, hysteresis in the actuation diagram, and a pressure

deadband. To reconstruct the PAM behavior, a series of nonlinear model refinements were proposed for use with a previously derived force balance analysis to address each nonlinearity in turn. To account for PAM stiffening, a nonlinear elastic model was used wherein stress was expressed as a quartic polynomial of strain. The empirically identified modulus coefficients trended well with pressure and could be expressed as spline fits for a lookup table of coefficient values. Hysteresis in the force vs. displacement curves was modeled using an empirical friction factor that was linearly dependent on pressure, and thus also suitable for a lookup table. To address the pressure deadband, a uniform pressure offset term was incorporated into the model. With the inclusion of these three refinements, the proposed PAM force model was shown to capture the full actuation behavior of the miniature PAM at each operating pressure and reconstruct the response of the small-scale actuator with much more accuracy than previously possible. Additional model analysis revealed that the inclusion of a length correction term to account for the non-cylindrical tip shape of the PAM did not significantly impact the accuracy of the nonlinear elastic force balance model at this small scale.

4.2. Push-PAM Development and Analysis

In this second study, an innovative full-scale push-PAM converted the normal direction of force and motion for a contractile PAM such that the resulting actuator achieved excellent compressive force generation and extensile motion with just a small increase in friction, weight, and cost. The experimental characterization of the push-PAM revealed the nonlinear quasi-static behavior of the actuator and verified that the push-PAM was capable of producing forces and strokes comparable to a similarly sized contractile PAM tested under the same conditions. For both the contractile PAM and the

push-PAM, the same three nonlinear phenomena that were observed in the characterization of the miniature PAMs (i.e. nonlinear PAM stiffness, hysteresis of the force vs. displacement response, and a pressure deadband) were observed during testing on these full-scale PAMs as well. Utilizing the refined force balance analysis that was originally developed for the small-scale PAMs was shown to reconstruct the actuator response with minimal error for both the contractile PAM and the push-PAM. These results not only confirmed that contractile PAMs and push-PAMs could be accurately modeled using the same analysis methods, but they also validated the use of this nonlinear model for full-scale PAMs. Further model analysis revealed that the inclusion of a length correction term reduced the accuracy of the nonlinear elastic force balance model and lessened the physical significance of the proposed material model for these full-scale PAMs.

4.3. Significant Contributions to PAM Technology

The primary contribution of this work is a robust analysis method that is capable of predicting highly nonlinear PAM actuation behavior for a wide range of PAM sizes and configurations. The use of a nonlinear stress vs. strain model with systematic parameter identification for the modulus coefficients is completely new to PAM research, and when this refinement is used in conjunction with a simple hysteresis model and pressure bias, the accuracy of the full model in predicting PAM behavior far surpasses that which has been demonstrated by previous researchers. Furthermore, although this nonlinear analysis relies on measured force vs. displacement data for parameter identification, preliminary results indicate that the system variables trend well with actuation pressure and could thus be used to generate a lookup table to enable more

precise control of the PAM over the full measured range of operating pressures. Additionally, for both the miniature PAM and the full-scale PAMs characterized in this study, it was shown that the nonlinear elastic force balance model eliminated the need for a length correction term, thus simplifying the model.

The two novel PAMs discussed in this work also represent significant contributions to PAM technology. While previous researchers have investigated miniature PAMs, this is the first study to carefully describe a simple, low-cost method for manufacturing these small-scale actuators using commercially available materials. Furthermore, the push-PAM is the first device to fully utilize the operational characteristics of a contractile PAM, but convert the contraction to extension without sacrificing actuator performance or simplicity in order to produce the desired change.

4.4. Future Work

Given that both new PAMs presented in this work fill a niche for types of actuation packages that were previously unsuitable for traditional contractile PAMs, the next important step in this research is to investigate and develop the applications of these novel actuators. The miniature PAMs, for example, would be ideal for actuating the desired movement of fingers on a robotic manipulator, as they are small enough to be contained within the palm of a robotic hand. For the push-PAM, an industrial stamping application would make excellent use of the actuator's remarkable compressive forces and extensile motion.

Building on the analysis work that has been presented in this thesis, the next step in the development of the nonlinear elastic force balance model is to further investigate the physical nature of the nonlinear elastic material model. In the current state of the

model development, the analysis method is primarily phenomenological and the elastic modulus values (E_k) for each PAM actuator must be systematically identified using experimental results. Although this post-dictive style of modeling does reconstruct PAM behavior with high accuracy, the final goal is to develop a predictive nonlinear elastic material model wherein the coefficient values can be determined without PAM experimental results based on basic material properties such as elastic modulus, Poisson's ratio, and shear modulus. In addition to refining the nonlinear force balance model, it will be necessary to utilize this analysis method to develop accurate quasi-static actuation strategies and dynamic models so that these PAMs may be carefully controlled in any actuation scheme.

Appendix

A.1 MATLAB Code Used for Optimization of Model Parameters

```
% This script was used to analyze the experimental results from the MTS
% machine, as well as model the performance of the PAM and compare
% these results to the experimental data. This code was initially
% developed for the miniature PAM, then modified for use with the Push
% PAM.



%% Part 1 - Experimental Results

% This section reads in data from the MTS machine and plots the force
% vs. displacement curves at each pressure. Also, it establishes global
% variables and pressure-averaged force data (spline fits) that will be
% necessary in later parts of the code for modeling.


clc
clear all
close all

global X_actual Y_actual Lrange B N tipfact R0 Vb L0 P Pa k m ...
    X_actual_lin Y_actual_lin Lrange_lin

c = ['r+bxg*kdc.mo'];%vector of colors and shapes for plotting
lb2N = 4.448222; %conversion factor from pounds to Newtons
lw = 'linewidth';
lwn = 2; %linewidth for plotting

% File names of tests to be plotted
aa = 'millipam_2p0_air_30psi_spec4_07.txt';
bb = 'millipam_2p0_air_40psi_spec4_07.txt';
cc = 'millipam_2p0_air_50psi_spec4_07.txt';
dd = 'millipam_2p0_air_60psi_spec4_07.txt';
ee = 'millipam_2p0_air_70psi_spec4_07.txt';
ff = 'millipam_2p0_air_80psi_spec4_07.txt';

% Compile file and create vector of pressures and active length
files = [{{aa} {bb} {cc} {dd} {ee} {ff}}]'; %cell array of file names
La = 39.16/25.4*ones(1,length(files)); %active length in inches
P = [29.7 40.1 49.6 60.3 70.5 79.2]; %actual pressures tested in psi

cal = 508.41; %100 lb load cell calibration factor for MTS
```

```
for i = 1:length(files)

    % Read in data
    data = dlmread(char(files{i}),'\t', 5, 0);



    % Manipulate Data
    f = data(:,4)*cal; %force (lbs)
    fc = -1*data(:, 2); %free contraction (inches)
    fc = fc-min(fc); %accounts for initial offset in displacement
    pc = (fc/La(i)); %percent contraction



    % Average data (for modeling)
    % Number of chunks the data is divided into for taking the average
    num_chunks = int64(max(pc)*500);

    % Free contraction segments over which data is averaged
    chunk = linspace(min(fc),max(fc),num_chunks);

    for yy = 1:length(chunk)-1
        loc = find(fc >= chunk(yy) & fc <= chunk(yy+1));
        f_avg(i,yy) = mean(f(loc));
        fc_avg(i,yy) = mean(fc(loc));
        pc_avg(i,yy) = mean(pc(loc));
    end

    % Spline fit the averaged data (for modeling)
    % Percent contraction spline fits (full and linear)
    pc_spline(i,:) = linspace(pc_avg(i,1), pc_avg(i,end), 100);
    pc_spline_lin(i,:) = linspace(pc_avg(i,1), .04, 100);

    % Force spline fits (full and linear)
    f_spline(i,:) = spline(pc_avg(i,:),f_avg(i,:), pc_spline(i,:));
    f_spline_lin(i,:) = spline(pc_avg(i,:),f_avg(i,:), ...
        pc_spline_lin(i,:));



    % Filter data for clearer point plotting
    filter = 8; %plots every 8 data points for filter = 8
    clear pcnew lamnew fnew
    for ee = 1:length(fc)/filter
        pcnew(ee) = pc(filter*ee);
        fnew(ee) = f(filter*ee);
    end
```

```
    % Plot Data
    figure(1) %% FORCE VS PERCENT CONTRACTION
    set(gcf,'name','F vs PC')
    set(gca, 'fontsize', 14)
    set(gca, 'fontname', 'Times New Roman')
    count = 2*i-1;
    plot(pcnew, fnew*lb2N, c(count:count+1))
    xlabel('Contraction, \DeltaL / L_0')
    ylabel('Force, N')
    hold on
    box on



    % Save performance specs
    force_exp(i) = max(f); %max blocked force
    force_avg(i) = max(f_spline(i,:)); %pressure-averaged blocked force
    fc_exp(i) = max(fc); %free contraction (inches)
    pc_exp(i) = max(pc); %free contraction (percent)
end


figure(1) %% FORCE VS PERCENT CONTRACTION
axis([0 .08 0 140])
legend('207 kPa', '276 kPa', '345 kPa', '414 kPa', '483 kPa','552 kPa')



%% Part 2 - Optimization/Model (fmincon)

% This section establishes the modeling parameters and runs the
% optimization routine for the nonlinear elastic force balance model.
% It also calculates modeling results based on other models (Gaylord,
% Linear Elastic Force Balance) to compare the results and plots the
% output.


% PAM Info
% Bladder Info
L0 = La(1); %active length in inches (index if using multiple PAMs)
OD0 = 3/25.4; %bladder outer diameter in inches
R0 = OD0/2; %bladder outer radius in inches
t0 = .5/25.4; %bladder thickness in inches
ID0 = OD0 - 2*t0; %bladder inner diameter in inches
Vb = (pi/4)*L0*(OD0^2 - ID0^2); %bladder volume (in^3)
Er = 1.75e6 * .000145; %bladder Youngs modulus (psi)

% Braid Info
theta0 = 77.4*pi/180; %initial braid angle measured from actual PAM
N = L0/tan(theta0)/(OD0*pi); %number of turns of the braid
B = L0/sin(theta0); %true length of a single filament
```

```
% Length range for modeling over full contraction and linear
% portion of contraction
for i = 1:length(P)
    Lrange(i,:) = linspace(L0,(1-max(pc_spline(i,:)))*L0,100);
    Lrange_lin(i,:) = linspace(L0,(1-max(pc_spline_lin(i,:)))*L0,100);
end

% Tip factor for length correction
tipfact = pi/2 - 1;

% Pressure offset from linear trend line of blocked force
Pa = 11.08;

% Empirically determined friction factor
kf = [.14 .12 .10 .08 .06 .04];



% Optimization Parameters
% Establish lower and upper bounds
Lb = -10000*ones(1,4); % lower bound on Er in psi
Ub = 10000*ones(1,4); %upper bound on Er in psi

% Linear Inequality Constraints (for fmincon) in the form of Ax <= b
b = []; %zeros(5,1); % These constraints force x to be non-negative
A = []; %-1*eye(5);

% Linear Equality Constraints (for fmincon) in the form of Ax = b;
Aeq = [];
beq = [];

% Initial conditions (for fmincon)
Er01 = 300*ones(1,1); %Initial guesses for Er in psi
Er02 = 300*ones(1,2);
Er03 = 300*ones(1,3);
Er04 = 300*ones(1,4);

% Optimization options for fmincon
options = optimset('TolFun',1e-15,'TolX',1e-10, ...
    'MaxFunEvals', 1000000,'MaxIter',1000000,...
    'Display','iter-detailed')



% Run optimizer, calculate model results, plot model output
for k = 1:length(P)

    % RUN OPTIMIZER TO FIND Ek FOR EACH PRESSURE
    % Full contraction data for optimizer to match
    X_actual = pc_spline(k,:);
    Y_actual = f_spline(k,:);

    % Linear portion of contraction for optimizer to match
    X_actual_lin = pc_spline_lin(k,:);
    Y_actual_lin = f_spline_lin(k,:);
```

```
    %Run fmincon for M = 1 (linear portion)
    [Erfm1(k,:),fval_fm1(k)] = ...
        fmincon(@PAMObjFunction1T, Er01,A,b,Aeq,beq,Lb,Ub,[],options);

    %Run fmincon for M = 2 (full) and M = 2 (linear portion)
    [Erfm2(k,:),fval_fm2(k)] = ...
        fmincon(@PAMObjFunction2T, Er02,A,b,Aeq,beq,Lb,Ub,[],options);
    [Erfm2_lin(k,:),fval_fm2_lin(k)] = ...
        fmincon(@PAMObjFunction2_linT, Er02,A,b,Aeq,beq,Lb,Ub,[],...
        options);

    %Run fmincon for M = 3 (full)
    [Erfm3(k,:),fval_fm3(k)] = ...
        fmincon(@PAMObjFunction3T, Er03,A,b,Aeq,beq,Lb,Ub,[],options);

    %Run fmincon for M = 4 (full) w/ and w/o L'
    [Erfm4(k,:),fval_fm4(k)] = ...
        fmincon(@PAMObjFunction4T, Er04,A,b,Aeq,beq,Lb,Ub,[],options);
    [Erfm4NT(k,:),fval_fm4NT(k)] = ...
        fmincon(@PAMObjFunction4NT, Er04,A,b,Aeq,beq,Lb,Ub,[],options);



    % CALCULATE MODEL RESULTS
    P(k) = P(k) - Pa; %Correction on P (pressure deadband)

    % Range of lengths (i.e. contraction) for plotting
    Lrange_plot =  linspace(L0, .9*L0, 1000);
%     Lrange_plot = Lrange (k,:);% USE WHEN CALCULATING ERROR

    % Percent contraction for plotting
    PC_plot = (L0-Lrange_plot)./L0;

    for j = 1:length(Lrange_plot)

        % Calculate instantaneous parameters
        L = Lrange_plot(j);
        R = sqrt(B^2 - L^2)/(2*pi*N);
        Lcor = L-2*tipfact*(R-R0);
        t = R - sqrt(R^2 - Vb/pi/L);

        % Gaylord Force w/o P' or L'
        FG(k,j) = (P(k)+Pa)*(3*L^2-B^2)/(4*N^2*pi);

        % Gaylord Force w/ P'and L'
        FG_prime(k,j) = P(k)*(3*Lcor^2-B^2)/(4*N^2*pi);

        % Linear Force Balance Model (non-optimized)
        Fbal(k,j) = P(k)*(3*Lcor^2-B^2)/(4*N^2*pi) + ...
            (Er*t*Lcor^2)*(1/R - 1/R0)/(2*N^2*pi) + ...
            Er*Vb*(1/L0 - 1/Lcor);
```

```
% Nonlinear Elastic Force Balance Model
% M = 1
Fbal_stiff1(k,j) = P(k)*(3*Lcor^2-B^2)/(4*N^2*pi) - ...
    (Erfm1(k,1)*t*Lcor^2)*(1/R0 - 1/R)/(2*N^2*pi) + ...
    Erfm1(k,1)*Vb*(1/L0 - 1/Lcor);

% M = 2 (over full and linear portion of contraction)
Fbal_stiff2(k,j) = P(k)*(3*Lcor^2-B^2)/(4*N^2*pi) - ...
    (Erfm2(k,1)*t*Lcor^2)*(1/R0 - 1/R)/(2*N^2*pi) + ...
    Erfm2(k,1)*Vb*(1/L0 - 1/Lcor) - ...
    (Erfm2(k,2)*t*Lcor^2)*(R/R0 - 1)^2/(2*N^2*pi*R)+ ...
    Erfm2(k,2)*(Vb/Lcor)*(Lcor/L0-1)^2;
Fbal_stiff2_lin(k,j) = P(k)*(3*Lcor^2-B^2)/(4*N^2*pi) - ...
    (Erfm2_lin(k,1)*t*Lcor^2)*(1/R0 - 1/R)/(2*N^2*pi) + ...
    Erfm2_lin(k,1)*Vb*(1/L0 - 1/Lcor) - ...
    (Erfm2_lin(k,2)*t*Lcor^2)*(R/R0 - 1)^2/(2*N^2*pi*R)+ ...
    Erfm2_lin(k,2)*(Vb/Lcor)*(Lcor/L0-1)^2;

% M = 3
Fbal_stiff3(k,j) = P(k)*(3*Lcor^2-B^2)/(4*N^2*pi) - ...
    (Erfm3(k,1)*t*Lcor^2)*(1/R0 - 1/R)/(2*N^2*pi) + ...
    Erfm3(k,1)*Vb*(1/L0 - 1/Lcor) - ...
    (Erfm3(k,2)*t*Lcor^2)*(R/R0 - 1)^2/(2*N^2*pi*R) + ...
    Erfm3(k,2)*(Vb/Lcor)*(Lcor/L0-1)^2 - ...
    (Erfm3(k,3)*t*Lcor^2)*(R/R0 - 1)^3/(2*N^2*pi*R) + ...
    Erfm3(k,3)*(Vb/Lcor)*(Lcor/L0-1)^3;

% M = 4 (with and without length correction)
Fbal_stiff4(k,j) = P(k)*(3*Lcor^2-B^2)/(4*N^2*pi) - ...
    (Erfm4(k,1)*t*Lcor^2)*(1/R0 - 1/R)/(2*N^2*pi) + ...
    Erfm4(k,1)*Vb*(1/L0 - 1/Lcor) - ...
    (Erfm4(k,2)*t*Lcor^2)*(R/R0 - 1)^2/(2*N^2*pi*R) + ...
    Erfm4(k,2)*(Vb/Lcor)*(Lcor/L0-1)^2 - ...
    (Erfm4(k,3)*t*Lcor^2)*(R/R0 - 1)^3/(2*N^2*pi*R) + ...
    Erfm4(k,3)*(Vb/Lcor)*(Lcor/L0-1)^3 - ...
    (Erfm4(k,4)*t*Lcor^2)*(R/R0 - 1)^4/(2*N^2*pi*R)+ ...
    Erfm4(k,4)*(Vb/Lcor)*(Lcor/L0-1)^4;
Fbal_stiff4NT(k,j) = P(k)*(3*L^2-B^2)/(4*N^2*pi) - ...
    (Erfm4NT(k,1)*t*L^2)*(1/R0 - 1/R)/(2*N^2*pi) + ...
    Erfm4NT(k,1)*Vb*(1/L0 - 1/L) - ...
    (Erfm4NT(k,2)*t*L^2)*(R/R0 - 1)^2/(2*N^2*pi*R) + ...
    Erfm4NT(k,2)*(Vb/L)*(L/L0-1)^2 - ...
    (Erfm4NT(k,3)*t*L^2)*(R/R0 - 1)^3/(2*N^2*pi*R) + ...
    Erfm4NT(k,3)*(Vb/L)*(L/L0-1)^3 - ...
    (Erfm4NT(k,4)*t*L^2)*(R/R0 - 1)^4/(2*N^2*pi*R)+ ...
    Erfm4NT(k,4)*(Vb/L)*(L/L0-1)^4;

% Friction Model
% Friction force
Ff(k,j) = Fbal_stiff4(k,j)*kf(k);

% Total force during extension - friction adds
Ftote(k,j) = Fbal_stiff4(k,j)+Ff(k,j);

% Total force during contraction - friction subtracts
Ftotc(k,j) = Fbal_stiff4(k,j)-Ff(k,j);
```

```
%         %Error Calculations (error as percent of blocked force)
%         error_FG(k,j) = abs((FG(k,j)-f_spline(k,j))/(force_avg(k)));
%         error_FG_prime(k,j) = abs((FG_prime(k,j)-f_spline(k,j))/...
%             (force_avg(k)));
%         error_Fbal(k,j) = abs((Fbal(k,j)-f_spline(k,j))/...
%             (force_avg(k)));
%         error_Fbal_stiff4(k,j) = abs((Fbal_stiff4(k,j)-...
%             f_spline(k,j))/(force_avg(k)));
%         error_Fbal_stiff4NT(k,j) = abs((Fbal_stiff4NT(k,j)-...
%             f_spline(k,j))/(force_avg(k)));
%
%         avg_error4(k) = mean(error_Fbal_stiff4(k,:));
%         avg_error4NT(k) = mean(error_Fbal_stiff4NT(k,:));

    end

    P(k) = P(k) + Pa; %Restore activation pressure to real value



    % PLOT MODEL RESULTS
    % Rename model output (easier for plotting)
    Yfm1 = Fbal_stiff1(k,:);
    Yfm2 = Fbal_stiff2(k,:);
    Yfm2_lin = Fbal_stiff2_lin(k,:);
    Yfm3 = Fbal_stiff3(k,:);
    Yfm4 = Fbal_stiff4(k,:);
    Yfm4NT = Fbal_stiff4NT(k,:);

    figure(1) % Plots vs full data (pick which results to plot)
%     plot(PC_plot, Fbal(k,:)*lb2N, 'b--', lw, lwn)
%     plot(PC_plot, Yfm1*lb2N, 'g--', lw, lwn)
%     plot(PC_plot, Yfm2*lb2N, 'm--', lw, lwn)
%     plot(PC_plot, Yfm3*lb2N, 'c--', lw, lwn)
%     plot(PC_plot, Yfm4*lb2N, 'k--', lw, lwn)
    plot(PC_plot, Ftote(k,:)*lb2N, 'k--', lw, lwn)
    plot(PC_plot, Ftotc(k,:)*lb2N, 'k--', lw, lwn)
%     legend('207 kPa', '276 kPa', '345 kPa', '414 kPa', '483 kPa', ...
%         '552 kPa', 'Model: F_G + F_N_L_F_B')
    legend('207 kPa', '276 kPa', '345 kPa', '414 kPa', '483 kPa', ...
        '552 kPa', 'Model: F_G + F_N_L_F_B + F_F')


    figure (2) % Plots vs Spline Curve (pick which results to plot)
    hold on
    box on
    set(gcf,'name','Spline vs Model')
    set(gca, 'fontsize', 14)
    set(gca, 'fontname', 'Times New Roman')
    plot(X_actual,Y_actual*lb2N,'gd', lw, lwn)
%     plot(PC_plot, FG(k,:)*lb2N, 'm-', lw, lwn)
%     plot(PC_plot, FG_prime(k,:)*lb2N, 'b-', lw, lwn)
%     plot(PC_plot, Fbal(k,:)*lb2N, 'r--', lw, lwn)
%     plot(PC_plot,Yfm1*lb2N,'r--',lw,lwn)
%     plot(PC_plot,Yfm2_lin*lb2N,'k-',lw,lwn)
```

```
%     plot(PC_plot,Yfm2*lb2N,'r--',lw,lwn)
%     plot(PC_plot,Yfm3*lb2N,'g--',lw,lwn)
    plot(PC_plot,Yfm4*lb2N,'k-',lw,lwn)
    plot(PC_plot,Yfm4NT*lb2N,'r--',lw,lwn)
    xlabel('Contraction, \DeltaL / L_0')
    ylabel('Force, N')
%     legend('F_A_V_G','M = 1: E_1 Non-Optimized',...
%         'M = 1: E_1 Optimized Over Linear Portion', ...
%         'Location', 'SouthWest')
%     legend('F_A_V_G','M = 2: E_k Optimized Over Linear Portion',...
%         'M = 2: E_k Optimized Over Full Contraction',...
%         'Location', 'SouthWest')
%     legend('F_A_V_G','M = 4: E_k Optimized Over Full Contraction',...
%         'Location', 'SouthWest')
%     legend('F_A_V_G','Model: F_G + F_N_L_F_B')
%     legend('F_A_V_G','Model: F_G', 'Model: F_G(P1, L1)',...
%         'Model: F_G(P1, L1) + F_L_F_B(L1)',...
%         'Model: F_G(P1, L1) + F_N_L_F_B(L1)')
    legend('F_A_V_G','Model: F_G + F_N_L_F_B with Corrected Length',...
        'Model: F_G + F_N_L_F_B without Corrected Length')
    axis([0 .08 0 140])
%     axis([0 .07 0 100])


%     figure(5) %Error plots (pick which results to plot)
%     box on
% %     semilogy(PC_plot, error_FG(k,:)*100, 'm-', lw, lwn)
% %     hold on
% %     semilogy(PC_plot, error_FG_prime(k,:)*100, 'b-', lw, lwn)
% %     semilogy(PC_plot, error_Fbal(k,:)*100, 'r--', lw, lwn)
%     semilogy(PC_plot, error_Fbal_stiff4(k,:)*100, 'k-', lw, lwn)
%     hold on
%     semilogy(PC_plot, error_Fbal_stiff4NT(k,:)*100, 'r--', lw, lwn)
%     set(gcf,'name','Error Curves')
%     set(gca, 'fontsize', 14)
%     set(gca, 'fontname', 'Times New Roman')
%     xlabel('Contraction, \DeltaL / L_0')
%     ylabel('Error (% Pressure-Averaged Blocked Force)')
% %     legend('F_G', 'F_G(P1, L1)', 'F_G(P1, L1) + F_L_F_B(L1)', ...
% %         'F_G(P1, L1) + F_N_L_F_B(L1)', 'Location', 'SouthWest')
%     legend('F_G + F_N_L_F_B with Corrected Length', ...
%         'F_G + F_N_L_F_B without Corrected Length', ...
%         'Location', 'SouthWest')
% %     axis([0 .07 .001 1000])
%     axis([0 .07 .001 1])

end
```

```
%% Part 3 - Additional Plots of Interest

% This section plots the stress-strain curves associated with the model
% output, as well as Ek vs pressure


%Plot Stress Strain Curves for 414kPa case
ep = linspace (0, 1.1915, 100);
sig1_real = Er*ep;
sig1_opt = Erfm1(4,1)*ep;
sig2_lin = Erfm2_lin(4,1)*ep + Erfm2_lin(4,2)*ep.^2;
sig2_full = Erfm2(4,1)*ep + Erfm2(4,2)*ep.^2;
sig4 = Erfm4(4,1)*ep + Erfm4(4,2)*ep.^2 + Erfm4(4,3)*ep.^3 +...
    Erfm4(4,4)*ep.^4;
figure (3)
hold on
box on
set(gcf,'name','Stress Strain Curves')
set(gca, 'fontsize', 14)
set(gca, 'fontname', 'Times New Roman')
plot(ep, sig1_real/145,'b-', lw, lwn)
plot(ep, sig1_opt/145, 'r--', lw, lwn)
% plot(ep, sig2_lin/145, 'g-', lw,lwn)
% plot(ep, sig2_full/145, 'm-', lw, lwn)
plot(ep, sig4/145, 'k--', lw, lwn)
xlabel('Strain')
ylabel('Stress, MPa')
legend('M = 1: E_1 Non-Optimized', ...
    'M = 1: E_1 Optimized Over Linear Portion', ...
    'M = 4: E_k Optimized Over Full Contraction', ...
    'Location', 'NorthWest' )
axis([0 1.2 0 9])


%Plot E_k vs Pressure
PMPa = [30 40 50 60 70 80]*6.9;
figure (4)
hold on
box on
set(gcf,'name','Ek vs P')
set(gca, 'fontsize', 14)
set(gca, 'fontname', 'Times New Roman')
plot(PMPa, Erfm4(:,1)/145, 'k.-', lw, 1.1)
plot(PMPa, Erfm4(:,2)/145, 'rd-', lw, 1.1)
plot(PMPa, Erfm4(:,3)/145, 'bo-', lw, 1.1)
plot(PMPa, Erfm4(:,4)/145, 'gs-', lw, 1.1)
xlabel('Pressure, kPa')
ylabel('E_k, MPa')
legend('M = 4: E_1', 'M = 4: E_2', 'M = 4: E_3', ...
    'M = 4: E_4', 'Location', 'SouthWest')
axis([200 600 -10 10])
```

A.2 MATLAB Objective Functions for *fmincon*

A.2.1 Objective Function for M = 1

```
function [error] = PAMObjFunction1T(Er)

% This is the objective function for M = 1 (optimized over the linear
% portion of the contraction) with length correction for tip effects

global ploton X_actual Y_actual Lrange B N tipfact R0 Vb L0 P Pa k ...
    X_actual_lin Y_actual_lin Lrange_lin;

Yreal = Y_actual_lin; %Splined curve fit of the experimental data

    P(k) = P(k) - Pa; %Correction on P (activation pressure)

    for j = 1:length(Lrange_lin)
        L = Lrange_lin(k,j);
        R = sqrt(B^2 - L^2)/(2*pi*N);
        Lcor = L-2*tipfact*(R-R0);
        t = R - sqrt(R^2 - Vb/pi/L);

        % Nonlinear Force Balance Terms
        Ynew(j) = P(k)*(3*Lcor^2-B^2)/(4*N^2*pi) - ...
            (Er(1)*t*Lcor^2)*(1/R0 - 1/R)/(2*N^2*pi) + ...
            Er(1)*Vb*(1/L0 - 1/Lcor);
    end

  P(k) = P(k) + Pa; %Restore activation pressure to real value

% Normalized error (trying to minimize this)
error = sum(((Ynew - Yreal)./Yreal).^2);
```

A.2.2 Objective Function for M = 2

```
function [error] = PAMObjFunction2T(Er)

% This is the objective function for M = 2 (optimized over the full
% contraction) with length correction for tip effects

global ploton X_actual Y_actual Lrange B N tipfact R0 Vb L0 P Pa k;

Yreal = Y_actual; %Splined curve fit of the experimental data

    P(k) = P(k) - Pa; %Correction on P (activation pressure)

    for j = 1:length(Lrange)
        L = Lrange(k,j);
        R = sqrt(B^2 - L^2)/(2*pi*N);
        Lcor = L-2*tipfact*(R-R0);
        t = R - sqrt(R^2 - Vb/pi/L);
```

```
        %Nonlinear Force Balance Terms
        Ynew(j) = P(k)*(3*Lcor^2-B^2)/(4*N^2*pi) - ...
            (Er(1)*t*Lcor^2)*(1/R0 - 1/R)/(2*N^2*pi) + ...
            Er(1)*Vb*(1/L0 - 1/Lcor) - ...
            (Er(2)*t*Lcor^2)*(R/R0 - 1)^2/(2*N^2*pi*R) + ...
            Er(2)*(Vb/Lcor)*(Lcor/L0-1)^2;
    end

  P(k) = P(k) + Pa; %Restore activation pressure to real value

% Normalized error (trying to minimize this)
error = sum(((Ynew - Yreal)./Yreal).^2);
```

A.2.3 Objective Function for M = 2 (linear portion)

```
function [error] = PAMObjFunction2_linT(Er)

% This is the objective function for M = 2 (optimized over the linear
% portion of the contraction) with length correction for tip effects

global ploton X_actual Y_actual Lrange B N tipfact R0 Vb L0 P Pa k...
    X_actual_lin Y_actual_lin Lrange_lin;

Yreal = Y_actual_lin; %Splined curve fit of the experimental data

    P(k) = P(k) - Pa; %Correction on P (activation pressure)

    for j = 1:length(Lrange_lin)
        L = Lrange_lin(k,j);
        R = sqrt(B^2 - L^2)/(2*pi*N);
        Lcor = L-2*tipfact*(R-R0);
        t = R - sqrt(R^2 - Vb/pi/L);

        % Nonlinear Force Balance Terms
        Ynew(j) = P(k)*(3*Lcor^2-B^2)/(4*N^2*pi) - ...
            (Er(1)*t*Lcor^2)*(1/R0 - 1/R)/(2*N^2*pi) +...
            Er(1)*Vb*(1/L0 - 1/Lcor) -...
            (Er(2)*t*Lcor^2)*(R/R0 - 1)^2/(2*N^2*pi*R) +...
            Er(2)*(Vb/Lcor)*(Lcor/L0-1)^2;
    end

  P(k) = P(k) + Pa; %Restore activation pressure to real value

% Normalized error (trying to minimize this)
error = sum(((Ynew - Yreal)./Yreal).^2);
```

A.2.4 Objective Function for M = 3

```
function [error] = PAMObjFunction3T(Er)

% This is the objective function for M = 3 (optimized over the full
% contraction) with length correction for tip effects

global ploton X_actual Y_actual Lrange B N tipfact R0 Vb L0 P Pa k;

Yreal = Y_actual; %Splined curve fit of the experimental data

    P(k) = P(k) - Pa; %Correction on P (activation pressure)

    for j = 1:length(Lrange)
        L = Lrange(k,j);
        R = sqrt(B^2 - L^2)/(2*pi*N);
        Lcor = L-2*tipfact*(R-R0);
        t = R - sqrt(R^2 - Vb/pi/L);

        %Nonlinear Force Balance Terms
        Ynew(j) = P(k)*(3*Lcor^2-B^2)/(4*N^2*pi) -...
            (Er(1)*t*Lcor^2)*(1/R0 - 1/R)/(2*N^2*pi) +...
            Er(1)*Vb*(1/L0 - 1/Lcor) - ...
            (Er(2)*t*Lcor^2)*(R/R0 - 1)^2/(2*N^2*pi*R) +...
            Er(2)*(Vb/Lcor)*(Lcor/L0-1)^2 -...
            (Er(3)*t*Lcor^2)*(R/R0 - 1)^3/(2*N^2*pi*R) +...
            Er(3)*(Vb/Lcor)*(Lcor/L0-1)^3;
    end

  P(k) = P(k) + Pa; %Restore activation pressure to real value

% Normalized error (trying to minimize this)
error = sum(((Ynew - Yreal)./Yreal).^2);
```

A.2.5 Objective Function for M = 4

```
function [error] = PAMObjFunction4T(Er)

% This is the objective function for M = 4 (optimized over the full
% contraction) with length correction for tip effects

global ploton X_actual Y_actual Lrange B N tipfact R0 Vb L0 P Pa k;

Yreal = Y_actual; %Splined curve fit of the experimental data

    P(k) = P(k) - Pa; %Correction on P (activation pressure)

    for j = 1:length(Lrange)
        L = Lrange(k,j);
        R = sqrt(B^2 - L^2)/(2*pi*N);
        Lcor = L-2*tipfact*(R-R0);
        t = R - sqrt(R^2 - Vb/pi/L);
```

```
        % Nonlinear Force Balance Terms
        Ynew(j) = P(k)*(3*Lcor^2-B^2)/(4*N^2*pi) - ...
            (Er(1)*t*Lcor^2)*(1/R0 - 1/R)/(2*N^2*pi) + ...
            Er(1)*Vb*(1/L0 - 1/Lcor) - ...
            (Er(2)*t*Lcor^2)*(R/R0 - 1)^2/(2*N^2*pi*R) + ...
            Er(2)*(Vb/Lcor)*(Lcor/L0-1)^2 - ...
            (Er(3)*t*Lcor^2)*(R/R0 - 1)^3/(2*N^2*pi*R) + ...
            Er(3)*(Vb/Lcor)*(Lcor/L0-1)^3 - ...
            (Er(4)*t*Lcor^2)*(R/R0 - 1)^4/(2*N^2*pi*R) + ...
            Er(4)*(Vb/Lcor)*(Lcor/L0-1)^4;
    end

  P(k) = P(k) + Pa; %Restore activation pressure to real value

% Normalized error (trying to minimize this)
error = sum(((Ynew - Yreal)./Yreal).^2);
```

A.2.6 Objective Function for M = 4 (without length correction)

```
function [error] = PAMObjFunction4NT(Er)

% This is the objective function for M = 4 (optimized over the full
% contraction) WITHOUT length correction for tip effects

global ploton X_actual Y_actual Lrange B N tipfact R0 Vb L0 P Pa k;

Yreal = Y_actual; %Splined curve fit of the experimental data

    P(k) = P(k) - Pa; %Correction on P (activation pressure)

    for j = 1:length(Lrange)
        L = Lrange(k,j);
        R = sqrt(B^2 - L^2)/(2*pi*N);
        Lcor = L; % LENGTH IS NOT CORRECTED
        t = R - sqrt(R^2 - Vb/pi/L);

        % Nonlinear Force Balance Terms
        Ynew(j) = P(k)*(3*Lcor^2-B^2)/(4*N^2*pi) -...
            (Er(1)*t*Lcor^2)*(1/R0 - 1/R)/(2*N^2*pi) +...
            Er(1)*Vb*(1/L0 - 1/Lcor) -...
            (Er(2)*t*Lcor^2)*(R/R0 - 1)^2/(2*N^2*pi*R) +...
            Er(2)*(Vb/Lcor)*(Lcor/L0-1)^2 -...
            (Er(3)*t*Lcor^2)*(R/R0 - 1)^3/(2*N^2*pi*R) +...
            Er(3)*(Vb/Lcor)*(Lcor/L0-1)^3 -...
            (Er(4)*t*Lcor^2)*(R/R0 - 1)^4/(2*N^2*pi*R) +...
            Er(4)*(Vb/Lcor)*(Lcor/L0-1)^4;
    end

  P(k) = P(k) + Pa; %Restore activation pressure to real value

% Normalized error (trying to minimize this)
error = sum(((Ynew - Yreal)./Yreal).^2);
```

References

Chapter 1 References

[1] Trivedi, D., and Rahn, C. D., 2012, "Soft Robotic Manipulators: Design, Analysis, and Control," *Plants and Mechanical Motion: A Synthetic Approach to Nastic Materials and Structures*, Wereley, N. M., and Sater, J. M., eds., DEStech Publications, Inc., Lancaster, PA, Chap. 7, pp. 141–165.

[2] Pritts, M. B., and Rahn, C. D., 2004, "Design of an Artificial Muscle Continuum Robot," *Proc. IEEE Int. Conf. on Robotics and Automation*, **5**, pp. 4742–4746.

[3] Zhu, B., Rahn, C. D., and Bakis, C. E., 2011, "Actuation of Fluidic Flexible Matrix Composites in Structural Media," J. Intell. Mater. Syst. Struct., **23**(3), pp. 269–278. DOI: 10.1177/1045389X11428676

[4] Philen, M. K., Shan, Y., Prakash, P., Wang, K. W., Rahn, C. D., Zydney, A. L., and Bakis, C. E., 2007, "Fibrillar Network Adaptive Structure with Ion-transport Actuation," J. Intell. Mater. Syst. Struct., **18**(4), pp. 323–334. DOI: 10.1177/1045389X06066097

[5] Woods, B. K. S., Gentry, M. F., Kothera, C. S., and Wereley, N. M., 2011, "Fatigue Life Testing of Swaged Pneumatic Artificial Muscles as Actuators for Aerospace Applications," J. Intell. Mater. Syst. Struct., **23**(3), pp. 327–343. DOI: 10.1177/1045389X11433495

[6] Woods, B. K. S., 2012, "Pneumatic Artificial Muscle Driven Trailing Edge Flaps for Active Rotors," Ph.D. Thesis, University of Maryland, College Park.

[7] Caldwell, D., Tsagarakis, N., and Medrano-Cerda, G. A., 2000, "Bio-mimetic Actuators: Polymeric Pseudo Muscular Actuators and Pneumatic Muscle Actuators for Biological Emulation," Mechatronics, **10**(4–5), pp. 499–530. DOI: 10.1016/S0957-4158(99)00071-9

[8] Daerden, F., 1999, "Conception and Realization of Pleated Pneumatic Artificial Muscles and their Use as Compliant Actuation Elements," Ph.D. Thesis, Vrije University Brussel, Brussels.

[9] Bharadwaj, K., Hollander, K. W., Mathis, C. A., and Sugar, T. G., 2004, "Spring Over Muscle (SOM) Actuator for Rehabilitation Devices," *Proc. Of the 26th Annual Int. Conf. of the IEEE EMBS*, **1**, pp. 2726–2729.

[10] Philen, M. K., 2009, "On the Applicability of Fluidic Flexible Matrix Composite Variable Impedance Materials for Prosthetic and Orthotic Devices," Smart Mater. Struct., **18,** 104023 (10pp). DOI: 10.1088/0964-1726/18/10/104023

[11] Ferris, D. P., Czerniecki, J. M., and Hannaford, B., 2005, "An Ankle-Foot Orthosis Powered by Artificial Pneumatic Muscles," J. Appl. Biomech., **21**(2), pp. 189–197.

[12] Sawicki, G. S., and Ferris, D. P., 2009, "A Pneumatically Powered Knee-Ankle-Foot Orthosis (KAFO) with Myoelectric Activation and Inhibition," J. Neuroeng. Rehabil., **6**(23), pp. 1–16.

[13] Robinson, R. M., Kothera, C. S., Woods, B. K. S., Vocke III, R. D., and Wereley, N. M., 2011, "High Specific Power Actuators for Robotic Manipulators," J. Intell. Mater. Syst. Struct., **22**(13), pp. 1501–1511. DOI: 10.1177/1045389X11417653

[14] Birch, M. C. *et al.*, 2001, "A Miniature Hybrid Robot Propelled by Legs," *Proc. of the 2001 IELE/RSJ Int. Conf. on Intelligent Robots and Systems,* **2**, pp. 845–851.

[15] De Volder, M., Moers, A. J. M., and Reynaerts, D., 2011, "Fabrication and Control of Miniature McKibben Actuators," Sensors Actuat. A, **166**(1), pp. 111–116. DOI: 10.1016/j.sna.2011.01.002

[16] Bubert, E. A., 2009, "Highly Extensible Skin for a Variable Wing-Span Morphing Aircraft Utilizing Pneumatic Artificial Muscle Actuation," M.S. Thesis, University of Maryland, College Park.

[17] Chen, Y., Yin, W., Liu, Y., and Leng, J., 2011, "Structural Design and Analysis of Morphing Skin Embedded with Pneumatic Muscle Fibers," Smart Mater. Struct., **20,** 085033 (8pp). DOI: 10.1088/0964-1726/20/8/085033

[18] Woods, B. K. S., Kothera, C. S., and Wereley, N. M., 2011, "Wind Tunnel Testing of a Helicopter Rotor Trailing Edge Flap Actuated via Pneumatic Artificial Muscles," J. Intell. Mater. Syst. Struct., **22**(13), pp. 1513–1528. DOI: 10.1177/1045389X11424216

[19] Zhang, Z., and Philen, M. K., 2011, "Review: Pressurized Artificial Muscles," J. Intell. Mater. Syst. Struct., **23**(3), pp. 255–268. DOI: 10.1177/1045389X11420592

[20] Gaylord, R., 1958, "Fluid Actuated Motor System and Stroking Device," U.S. Patent No. 2,844,126.

[21] Schulte, H. F., Adamski, D. F., and Pearson, J. R., 1961, "Characteristics of the Braided Fluid Actuator," Report at Department of Physical Medicine and Rehabilitation, the University of Michigan, Ann Arbor, MI, pp. 105–120.

[22] Chou, C., and Hannaford, B., 1994, "Static and Dynamic Characteristics of McKibben Pneumatic Artificial Muscles," *Proc. of ICRA*, **1**, pp. 281–286.

[23] Tondu, B., and Lopez, P., 2000, "Modeling and Control of McKibben Artificial Muscle Robot Actuators," IEEE Control Systems Magazine, **20**(2), pp. 15–38.

[24] Tsagarakis, N., and Caldwell, D., 2000, "Improved Modeling and Assessment of Pneumatic Muscle Actuators," *Proc. of ICRA*, **4**, pp. 3641–3646.

[25] Ferraresi, C., Franco, W., and Bertetto, A. M., 2001, "Flexible Pneumatic Actuators: A Comparison Between the McKibben and the Straight Fibres Muscles," J. Robot. Mechatron., **13**(1), pp. 56–63.

[26] Kothera, C. S., Jangid, M., Sirohi, J., and Wereley, N. M., 2009, "Experimental Characterization and Static Modeling of McKibben Actuators," ASME J. Mech. Des., **131**, 091010 (10pp). DOI: 10.1115/1.3158982

[27] Davis, S., and Caldwell, D., 2006, "Braid Effects on Contractile Range and Friction Modeling in Pneumatic Muscle Actuators," Int. J. Robot. Res., **25**(4), pp. 359–369.

[28] Tondu, B., 2012, "Modelling of the McKibben Artificial Muscle: A Review," J. Intell. Mater. Syst. Struct., **23**(3), pp. 225–253. DOI: 10.1177/1045389X11435435

[29] Woods, B. K. S., Wereley, N. M., Kothera, K. S., Boyer, S. M., "Extensile Fluidic Muscle Actuator," U.S Patent Appl. No. 12/955,242.

Chapter 2 References

[1] Vocke III, R. D., Kothera, C. S., Chaudhuri, A., Woods, B. K. S., and Wereley, N. M., 2012, "Design and Testing of a High-specific Work Actuator Using Miniature Pneumatic Artificial Muscles," J. Intell. Mater. Syst. Struct., **23**(3), pp. 365–378. DOI: 10.1177/1045389X11431743

[2] Woods, B. K. S., Kothera, C. S., and Wereley, N. M., 2011, "Wind Tunnel Testing of a Helicopter Rotor Trailing Edge Flap Actuated via Pneumatic Artificial Muscles," J. Intell. Mater. Syst. Struct., **22**(13), pp. 1513–1528. DOI: 10.1177/1045389X11424216

[3] Woods, B. K. S., 2012, "Pneumatic Artificial Muscle Driven Trailing Edge Flaps for Active Rotors," Ph.D. Thesis, University of Maryland, College Park.

[4] Caldwell, D., Tsagarakis, N., and Medrano-Cerda, G. A., 2000, "Bio-mimetic Actuators: Polymeric Pseudo Muscular Actuators and Pneumatic Muscle Actuators for Biological Emulation," Mechatronics, **10**(4–5), pp. 499–530. DOI: 10.1016/S0957-4158(99)00071-9

[5] Chou, C., and Hannaford, B., 1994, "Static and Dynamic Characteristics of McKibben Pneumatic Artificial Muscles," *Proc. of ICRA*, **1**, pp. 281–286.

[6] Woods, B. K. S., Gentry, M. F., Kothera, C. S., and Wereley, N. M., 2011, "Fatigue Life Testing of Swaged Pneumatic Artificial Muscles as Actuators for Aerospace Applications," J. Intell. Mater. Syst. Struct., **23**(3), pp. 327–343. DOI: 10.1177/1045389X11433495

[7] Chen, Y., Yin, W., Liu, Y., and Leng, J., 2011, "Structural Design and Analysis of Morphing Skin Embedded with Pneumatic Muscle Fibers," Smart Mater. Struct., **20,** 085033 (8pp). DOI: 10.1088/0964-1726/20/8/085033

[8] De Volder, M., Moers, A. J. M., and Reynaerts, D., 2011, "Fabrication and Control of Miniature McKibben Actuators," Sensors Actuat. A, **166**(1), pp. 111–116. DOI: 10.1016/j.sna.2011.01.002

[9] Birch, M. C., *et al.*, 2001, "A Miniature Hybrid Robot Propelled by Legs," *Proc. of the 2001 IELE/RSJ Int. Conf. on Intelligent Robots and Systems,* **2**, pp. 845–851.

[10] Solano, B., and Rotinat-Libersa, C., 2011, "Compact and Lightweight Hydraulic Actuation System for High Performance Millimeter Scale Robotic Applications: Modeling and Experiments," J. Intell. Mater. Syst. Struct., **22**(13), pp. 1479–1487. DOI: 10.1177/1045389X11418860

[11] Tiwari, R., Meller, M. A., Wajcs, K. B., Moses, C., Reveles, I., and Garcia, E., 2012, "Hydraulic Artificial Muscles," J. Intell. Mater. Syst. Struct., **23**(3), pp. 301–312. DOI: 10.1177/1045389X12438627

[12] Gaylord, R., 1958, "Fluid Actuated Motor System and Stroking Device," U.S. Patent No. 2,844,126.

[13] Schulte, H. F., Adamski, D. F., and Pearson, J. R., 1961, "Characteristics of the Braided Fluid Actuator," Report at Department of Physical Medicine and Rehabilitation, the University of Michigan, Ann Arbor, MI, pp. 105–120.

[14] Tondu, B., and Lopez, P., 2000, "Modeling and Control of McKibben Artificial Muscle Robot Actuators," IEEE Control Systems Magazine, **20**(2), pp. 15–38. DOI: 10.1109/37.833638

[15] Tsagarakis, N., and Caldwell, D., 2000, "Improved Modeling and Assessment of Pneumatic Muscle Actuators," *Proc. of ICRA*, **4**, pp. 3641–3646.

[16] Ferraresi, C., Franco, W., and Bertetto, A. M., 2001, "Flexible Pneumatic Actuators: A Comparison Between the McKibben and the Straight Fibres Muscles," J. Robot. Mechatron., **13**(1), pp. 56–63.

[17] Kothera, C. S., Jangid, M., Sirohi, J., and Wereley, N. M., 2009, "Experimental Characterization and Static Modeling of McKibben Actuators," ASME J. Mech. Des., **131**, 091010 (10pp). DOI: 10.1115/1.3158982

[18] Davis, S., and Caldwell, D., 2006, "Braid Effects on Contractile Range and Friction Modeling in Pneumatic Muscle Actuators," Int. J. Robot. Res., **25**(4), pp. 359–369.

[19] Tondu, B., 2012, "Modelling of the McKibben Artificial Muscle: A Review," J. Intell. Mater. Syst. Struct., **23**(3), pp. 225–253. DOI: 10.1177/1045389X11435435

[20] Diani, J., Fayolle, B., and Gilormini, P., 2009, "A Review on the Mullins Effect," Eur. Polym. J., **45**(3)**,** pp. 601–612. DOI: 10.1016/j.eurpolymj.2008.11.017

[21] Gelb, A., and Vander Velde, W. E., 1968, *Multiple-input Describing Functions and Nonlinear System Design*, McGraw-Hill, New York, pp. 4–5, Chap. 1.

Chapter 3 References

[1] Caldwell, D., Tsagarakis, N., and Medrano-Cerda, G. A., 2000, "Bio-mimetic Actuators: Polymeric Pseudo Muscular Actuators and Pneumatic Muscle Actuators for Biological Emulation," Mechatronics, **10**(4–5), pp. 499–530. DOI: 10.1016/S0957-4158(99)00071-9

[2] Chou, C., and Hannaford, B., 1994, "Static and Dynamic Characteristics of Mckibben Pneumatic Artificial Muscles," *Proc. of ICRA*, **1**, pp. 281–286.

[3] Woods, B. K. S., 2012, "Pneumatic Artificial Muscle Driven Trailing Edge Flaps for Active Rotors," Ph.D. Thesis, University of Maryland, College Park.

[4] Woods, B. K. S., Kothera, C. S., and Wereley, N. M., 2011, "Wind Tunnel Testing of a Helicopter Rotor Trailing Edge Flap Actuated via Pneumatic Artificial Muscles," J. Intell. Mater. Syst. Struct., **22**(13), pp. 1513–1528. DOI: 10.1177/1045389X11424216

[5] Vocke III, R. D., Kothera, C. S., Chaudhuri, A., Woods, B. K. S., and Wereley, N. M., 2012, "Design and Testing of a High-specific Work Actuator Using Miniature Pneumatic Artificial Muscles," J. Intell. Mater. Syst. Struct., **23**(3), pp. 365–378. DOI: 10.1177/1045389X11431743

[6] Woods, B. K. S., Gentry, M. F., Kothera, C. S., and Wereley, N. M., 2011, "Fatigue Life Testing of Swaged Pneumatic Artificial Muscles as Actuators for Aerospace Applications," J. Intell. Mater. Syst. Struct., **23**(3), pp. 327–343. DOI: 10.1177/1045389X11433495

[7] Philen, M. K., 2009, "On the Applicability of Fluidic Flexible Matrix Composite Variable Impedance Materials for Prosthetic and Orthotic Devices," Smart Mater. Struct., **18,** 104023 (10pp). DOI: 10.1088/0964-1726/18/10/104023

[8] Bharadwaj, K., Hollander, K. W., Mathis, C. A., and Sugar, T. G., 2004, "Spring Over Muscle (SOM) Actuator for Rehabilitation Devices," *Proc. Of the 26th Annual Int. Conf. of the IEEE EMBS*, **1**, pp. 2726–2729.

[9] Birch, M. C., *et al.*, 2001, "A Miniature Hybrid Robot Propelled by Legs," *Proc. of the 2001 IELE/RSJ Int. Conf. on Intelligent Robots and Systems,* **2**, pp. 845–851.

[10] De Volder, M., Moers, A. J. M., and Reynaerts, D., 2011, "Fabrication and Control of Miniature McKibben Actuators," Sensors Actuat. A, **166**(1), pp. 111–116. DOI: 10.1016/j.sna.2011.01.002

[11] Chen, Y., Yin, W., Liu, Y., and Leng, J., 2011, "Structural Design and Analysis of Morphing Skin Embedded with Pneumatic Muscle Fibers," Smart Mater. Struct., **20,** 085033 (8pp). DOI: 10.1088/0964-1726/20/8/085033

[12] Bubert, E. A., 2009, "Highly Extensible Skin for a Variable Wing-Span Morphing Aircraft Utilizing Pneumatic Artificial Muscle Actuation," M.S. Thesis, University of Maryland, College Park.

[13] Zhang, Z., and Philen, M. K., 2011, "Review: Pressurized Artificial Muscles," J. Intell. Mater. Syst. Struct., **23**(3), pp. 255–268. DOI: 10.1177/1045389X11420592

[14] Pritts, M. B., and Rahn, C. D., 2004, "Design of an Artificial Muscle Continuum Robot," *Proc. IEEE Int. Conf. on Robotics and Automation*, **5**, pp. 4742–4746.

[15] Trivedi, D., and Rahn, C. D., 2012, "Soft Robotic Manipulators: Design, Analysis, and Control," *Plants and Mechanical Motion: A Synthetic Approach to Nastic Materials and Structures*, Wereley, N. M., and Sater, J. M., eds., DEStech Publications, Inc., Lancaster, PA, Chap. 7, pp. 141–165.

[16] Liu, W., and Rahn, C. D., 2003, "Fiber-Reinforced Membrane Models of McKibben Actuators," ASME J. Appl. Mech., **70**(6), pp. 853–859. DOI: 10.1115/1.1630812

[17] Gaylord, R., 1958, "Fluid Actuated Motor System and Stroking Device," U.S. Patent No. 2,844,126.

[18] Schulte, H. F., Adamski, D. F., and Pearson, J. R., 1961, "Characteristics of the Braided Fluid Actuator," Report at Department of Physical Medicine and Rehabilitation, the University of Michigan, Ann Arbor, MI, pp. 105–120.

[19] Tondu, B., and Lopez, P., 2000, "Modeling and Control of McKibben Artificial Muscle Robot Actuators," IEEE Control Systems Magazine, **20**(2), pp. 15–38. DOI: 10.1109/37.833638

[20] Tsagarakis, N., and Caldwell, D., 2000, "Improved Modeling and Assessment of Pneumatic Muscle Actuators," *Proc. of ICRA*, **4**, pp. 3641–3646.

[21] Ferraresi, C., Franco, W., and Bertetto, A. M., 2001, "Flexible Pneumatic Actuators: A Comparison Between the McKibben and the Straight Fibres Muscles," J. Robot. Mechatron., **13**(1), pp. 56–63.

[22] Kothera, C. S., Jangid, M., Sirohi, J., and Wereley, N. M., 2009, "Experimental Characterization and Static Modeling of McKibben Actuators," ASME J. Mech. Des., **131**, 091010 (10pp). DOI: 10.1115/1.3158982

[23] Davis, S., and Caldwell, D., 2006, "Braid Effects on Contractile Range and Friction Modeling in Pneumatic Muscle Actuators," Int. J. Robot. Res., **25**(4), pp. 359–369.

[24] Solano, B., and Rotinat-Libersa, C., 2011, "Compact and Lightweight Hydraulic Actuation System for High Performance Millimeter Scale Robotic Applications: Modeling and Experiments," J. Intell. Mater. Syst. Struct., **22**(13), pp. 1479–1487. DOI: 10.1177/1045389X11418860

[25] Zhu, B., Rahn, C. D., and Bakis, C. E., 2011, "Actuation of fluidic flexible matrix composites in structural media," J. Intell. Mater. Syst. Struct., **23**(3), pp. 269–278. DOI: 10.1177/1045389X11428676

[26] Philen, M. K., Shan, Y., Prakash, P., Wang, K. W., Rahn, C. D., Zydney, A. L., and Bakis, C. E., 2007, "Fibrillar Network Adaptive Structure with Ion-transport Actuation," J. Intell. Mater. Syst. Struct., **18**(4), pp. 323–334. DOI: 10.1177/1045389X06066097

[27] Woods, B. K. S., Wereley, N. M., Kothera, K. S., Boyer, S. M., 2011, "Extensile Fluidic Muscle Actuator," U.S Patent Appl. No. 12/955,242.

[28] Tondu, B., 2012, "Modelling of the McKibben Artificial Muscle: A Review," J. Intell. Mater. Syst. Struct., **23**(3), pp. 225–253. DOI: 10.1177/1045389X11435435

[29] Gelb, A., and Vander Velde, W. E., 1968, *Multiple-input Describing Functions and Nonlinear System Design*, McGraw-Hill, New York, pp. 4–5, Chap. 1.